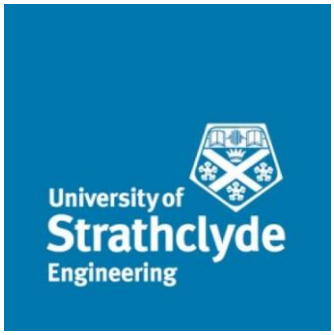


# Integration of Large Wind Farms to Weak Power Grids

Kamyab Givaki

A thesis presented in fulfilment of the requirements for the degree of
Doctor of Philosophy

Wind Energy CDT
Department of Electronic and Electrical Engineering
University of Strathclyde
Glasgow, UK

2017

This thesis is the result of the author's original research. It has been composed by the author and has not been previously submitted for examination which has led to the award of a degree.



Signed:

Date:

# Abstract

Power grids are changing significantly with the introduction of large amounts of renewable energy (especially wind) into the system. Integration of wind energy into the grid is challenging as, firstly it increases penetration stresses when compared to conventional generation as the wind is intermittent and fluctuates in power output. Secondly, most of the wind farms are located in offshore or rural areas which have good wind conditions. The grid in these regions is not normally strong. Most of the modern variable speed wind turbines use voltage source converters (VSCs) for grid integration. However, integrating VSCs to weak power grids will cause instability when a large amount of active power is transferred to the grid.

In this thesis, the integration of wind farms to very weak power grids is investigated. A multiple input, multiple output (MIMO) model of the grid side VSC of a wind turbine is developed in the frequency domain in which the d-axis of the synchronous reference frame (SRF) is aligned with the grid voltage. Then, this model has been used as the basis for modelling the multiple parallel converters in the frequency domain.

In this thesis, to improve the stability of the very weak grid connected of VSCs, a control method based on the d- and q- axis current error is introduced. This controller compensates the output angle of the phase locked loop (PLL) and the voltage amplitude of the converter. Using this controller, full rated active power transfer and fault ride-through are achieved under very weak grid connection.

Furthermore, a stabiliser controller based on virtual impedance is proposed in this thesis to achieve stable operation of a very weak grid connected VSC. This stabilising control method enables the VSC to operate at full power and to ride-through faults under very weak grid conditions. Based on this principle, an external device is proposed that can be utilised and connected to a weak point of the grid to allow a large amount of VSC interfaced power generation (e.g. wind power) to be connected to the grid without introducing stability issues.

# Acknowledgements

I would like to express my sincere gratitude to my supervisor Professor Lie Xu for his guidance over my period of research. He does not only share with me selflessly research ideas but also teaches me research attitudes, inspirations and methods that are more beneficial for me throughout a lifetime. It is my honour to have worked with you. I also would like to thank my second supervisor, Dr. Olimpo Anaya-Lara for his advice through my course of research.

Besides my supervisors, I would like to thank Dr. Dong Chen and Dr. Grain P. Adam for their comments and advice not only in academic but also in my daily life.

I also appreciate members of the PEDEC and Wind Energy CDT for the privilege to work with them during my time at the University of Strathclyde.

I am most grateful to my parents for the support they gave through my life. My Brother, Kamyar and my partner, Sabah have given me great support through my academic life when I needed the most, thank you both.

# List of Abbreviations and Symbols

## Abbreviations

| | |
|---|---|
| AC | Alternating Current |
| DC | Direct Current |
| DPC | Direct Power Control |
| DTC | Direct Torque Control |
| DFIG | Doubly Fed Induction Generator |
| FRC | Fully Rated Converter |
| HVAC | High Voltage Alternating Current |
| HVDC | High Voltage Direct Current |
| IC | Impedance-Conditioning |
| LCC | Line-Commutated Converter |
| MIMO | Multiple-Input-Multiple-Output |
| PLL | Phase Locked Loop |
| PCC | Point of Common Coupling |
| PSC | Power Synchronisation Control |
| PSL | Power Synchronisation Loop |
| p.u. | Per Unit |
| PWM | Pulse Width Modulation |

| | |
|---|---|
| SCC | Short Circuit Capacity |
| SCR | Short Circuit Ratio |
| SRF | Synchronous Reference Frame |
| VSG | Virtual Synchronous Generator |
| VISMA | Virtual Synchronous Machine |
| VDCL | Voltage Dependent Current Limit |
| VSC | Voltage Source Converter |

## Symbols

| | |
|---|---|
| $\lvert V_s \rvert$ | Grid voltage amplitude |
| $\mathbf{I_2}$ | Grid transformer current |
| $\mathbf{I_C}$ | Converter reactor current |
| $\mathbf{I_s}$ | Grid current |
| $k_i$ | Integral gain of controllers |
| $k_p$ | Proportional gain of controllers |
| $L_1$ | Inductance of Converter reactor |
| $L_{net}$ | Equivalent inductance of grid |
| $L_{tx}$ | Leakage inductance of transformer (p.u.) |
| $R_1$ | Resistance of Converter reactor |
| $R_{net}$ | Equivalent resistance of grid |
| $\mathbf{V_C}$ | Filter bus voltage |

| | |
|---|---|
| $\mathbf{V_s}$ | Grid voltage |
| $\omega_n$ | Natural frequency of controller |
| $\omega_s$ | Synchronous frequency of the grid |
| $\|V_C\|$ | Filter bus voltage amplitude |
| C | Filter capacitance (p.u.) |
| $I_{dc}$ | Converter DC side Current |
| M | Modulation index |
| P | Active power |
| $P_{ac}$ | Converter AC side power |
| $P_{dc}$ | Converter DC side power |
| Q | Reactive Power |
| Subscript “0” | Refers to operating point parameters |
| Subscript “b” | Refers to base values for p.u. calculations |
| Subscript “d” | d-axis parameter |
| Subscript “q” | q-axis parameter |
| Superscript “*” | Reference value for a parameter |
| $T_h$ | High-pass filter time constant |
| $\mathbf{V_{conv}}$ | Converter output voltage |
| XRr | X/r ratio |
| ω | Per unit synchronous frequency |
| $V_{DC}$ | DC voltage |

# Contents

Abstract ..... II
Acknowledgements ..... III
List of Abbreviation and Symbols ..... IV
Contents ..... VII
List of Figures ..... X
List of Tables ..... XIV
1. Introduction ..... 1
1.1. Wind Generation Technology Background ..... 1
1.2. Wind Turbine Configurations ..... 3
1.3. Transmission of Wind Power to the Grid ..... 4
1.4. Grid Integration of Wind Farms ..... 5
1.5. Research Scope and Contributions ..... 7
1.5.1. Research Scope ..... 7
1.5.2. Thesis Contributions ..... 8
1.6. Organisation of the Thesis ..... 9
2. Background and Literature Review ..... 10
2.1 General Aspect of Wind Farm Integration to the Grid ..... 10
2.2. Grid Strength ..... 11
2.2.1. High AC System Impedance ..... 12
2.2.2. Low Inertia ..... 13
2.3. Grid Connected VSC Control ..... 14
2.3.1. Direct Power Control ..... 15
2.3.2. Vector Current Control ..... 16
2.3.3. Grid Synchronisation ..... 16
2.4. Control of VSC Connected to Weak Grid ..... 17
2.4.1. Vector Current Control Based Control Methods ..... 18
2.4.2. Synchronous Generator Based Controller Schemes ..... 21
2.5. Summary ..... 28
3. Modelling of Grid Connected Voltage Source Converter ..... 30
3.1. Introduction ..... 30
3.2. Vector Current Control ..... 31

3.2.1. Outer Control Loop ..... 35
3.2.2. Phase Locked Loop ..... 38
3.3. Modelling of a Grid Connected Single Converter System ..... 38
3.3.1. AC Grid Connection ..... 38
3.3.2. PWM Modulation Modelling ..... 44
3.3.3. Converter Controller Modelling ..... 44
3.3.4. Overall System Modelling ..... 45
3.4. Phase locked Loop Modelling ..... 46
3.5. Model Validation and Case Studies for Developed MIMO Models ..... 48
3.5.1. Simplified Grid Connection ..... 49
3.5.2. System Model with Inter-Array Cables (T model) ..... 52
3.5.3. System Model with Inter-Array Cables (Pi model) ..... 54
3.6. Modelling of Parallel Converters ..... 55
3.7. Outer Loop Modelling ..... 60
3.8. Summary ..... 63
4. Improved Current Control of VSC with Current Error Based Compensation 64
4.1. Principles of VSC Control and the Proposed Current Error Based Voltage Angle and Magnitude Compensation ..... 64
4.2. Analytical Model and System Analysis ..... 70
4.3. Time Domain Case Studies ..... 75
4.3.1. Power Ramp Case Study ..... 75
4.3.2. Multiple Parallel VSC Test ..... 77
4.3.3. AC Fault Test (Fault-Ride-Through Test) ..... 79
4.4. Summary ..... 84
5. Virtual Impedance Based Stabiliser for Wind Farm Integration into Very Weak Grids ..... 85
5.1. Principles of operation of Virtual Impedance Voltage Stabiliser ..... 86
5.1.1. Dynamic Operating Point Based on System Power Flow ..... 86
5.1.2. Principles of the Proposed Virtual Impedance Control for Voltage Stabilisation ..... 91
5.2. Analytical Model of the Overall System for Dynamic Analysis ..... 96
5.3. Case Studies and Validation of the Proposed Control Method ..... 102
5.3.1. Power Ramp Test for the Proposed Controller ..... 102
5.3.2. Transient Test for Proposed Controller ..... 103

5.3.3. Test for Different Grid Strengths ..... 103
5.4. Grid Stabiliser for Weak Grid Integration of VSC ..... 104
5.5. Summary ..... 111
6. Conclusion and Future Work ..... 113
6.1. Conclusions ..... 113
6.2. Author's Contributions ..... 115
6.3. Suggestions for Future Research ..... 116
References ..... 117
Appendices ..... 125
Appendix 1. Simulation Models ..... 125
Appendix 2. List of Publications ..... 128

# List of Figures

Fig. 1.1. Generic wind turbine ..... 2
Fig. 1.2. Simplified power curve of a variable speed wind turbine ..... 3
Fig. 1.3. Schematic diagram of a fixed speed wind turbine ..... 3
Fig. 1.4. Schematic diagram of variable speed wind turbines ..... 4
Fig. 1.5. Different power electronic converters ..... 6
Fig. 2.1. Wind farm AC collection grid topologies [23] ..... 12
Fig. 2.2. Pulse width modulation with sinusoidal reference [40] ..... 15
Fig. 2.3. Schematic diagram of IC-PLL [83]. ..... 20
Fig. 2.4. Schematic diagram of the artificial bus method for grid synchronisation, (b) dq-reference frame representation of the artificial bus method [87] ..... 20
Fig. 2.5. Advanced outer loop control [74]. ..... 21
Fig. 2.6. Different models of the synchronous machine for VISMA implementation [100]. 24
Fig. 2.7. Components of VISMA [100]. ..... 25
Fig. 2.8. Schematic Diagram of VSG [88] ..... 25
Fig. 2.9. the schematic control block diagram of synchronverter [91]. ..... 26
Fig. 2.10. Schematic diagram of a Power Synchronisation loop [75] ..... 27
Fig. 2.11. Control diagram of VSC based on PSL [75]. ..... 28
Fig. 3.1. Schematic diagrams of a grid connected VSC ..... 32
Fig. 3.2. (a) Schematics of a grid connected VSC. (b) AC equivalent circuit of the VSC in the synchronous reference frame (c) DC equivalent circuit of the VSC [119]. ..... 32
Fig. 3.3. Schematic diagram of VSC current control ..... 35
Fig. 3.4. Schematic diagram of AC voltage controller (a) PI controller (b) Droop controller 37
Fig. 3.5. Simplified schematic diagram of an SRF PLL [77] ..... 38
Fig. 3.6. Single line schematic of a VSC connected to the power grid ..... 39
Fig. 3.7. Equivalent circuit of a grid connected VSC in the dq reference frame. ..... 39
Fig. 3.8. Single line schematic of a VSC connected to the power grid with T equivalent cable representation ..... 41
Fig. 3.9. Single line schematic of a VSC connected to the power grid with Pi equivalent representation of cables ..... 43
Fig. 3.10. Block diagram of the frequency domain model of the converter ..... 45
Fig. 3.11. Schematic block diagram of the MIMO model of the grid connected VSC ..... 46
Fig. 3.12. Positions of the actual and PLL measured filter bus (PCC) voltage ..... 47

Fig. 3.13. Simplified schematic of rotation due to the PLL. ..... 47
Fig. 3.14. Schematic block diagram of the MIMO model of the grid connected VSC with integrated PLL. ..... 50
Fig. 3.15. Step responses of the d- and q- axis currents for a small current step, operating condition 1: a step of 0.1 p.u. is applied to zero current; operating condition 2: a step of 0.05 is applied when converter is operating with 0.7 p.u. current. ..... 51
Fig. 3.16. Root loci of the d-axis current for different SCR levels ..... 52
Fig. 3.17. Step responses of the d-axis current for T equivalent of the medium voltage cables ..... 53
Fig. 3.18. Open loop Bode diagram of the simplified state-space model and T equivalent of cables ..... 53
Fig. 3.19. Step response of the system for various AC grid connections ..... 54
Fig. 3.20. Open loop Bode diagram of the system for various AC connections and cable length =20 km, SCR=5. ..... 55
Fig. 3.21. Single line circuit diagram of two parallel converters with T line model. ..... 56
Fig. 3.22. Block diagram of a dynamic model of parallel converters. ..... 58
Fig. 3.23. Step response for d-axis current of a multiple converter system, SCR=5. ..... 59
Fig. 3.24 . Root loci for d-axis current of one of the converters in a 2-converter system ..... 59
Fig. 3.25. Step response for d-axis current with input from the second converter and output of the first converter ..... 60
Fig. 3.26. Root locus for d-axis current with input from the second converter and output of the first converter ..... 61
Fig. 3.27. Block diagram of the frequency domain model of the outer control loop ..... 62
Fig. 3.28. The d-axis current step response for the MIMO model of system including an outer control loop ..... 62
Fig. 3.29. d-axis current root loci for the MIMO model of a system including an outer control loop (direction of arrows: SCR=100 to SCR=1). ..... 63
Fig. 4.1. Schematic of VSC connected to power grid. ..... 65
Fig. 4.2. Classical current vector control for VSC ..... 65
Fig. 4.3. Power ramp test with conventional vector control (from top to bottom: active power, actual voltage angle of Vc, PLL detected voltage angle of Vc, error between the actual and measured angle of Vc) ..... 67
Fig. 4.4. VSC with current vector control and proposed current error based compensation . 70
Fig. 4.5. Block diagram of the VSC analytical model in the frequency domain ..... 72
Fig. 4.6. Root locus (rated current, SCR = 100 to 1) ..... 74

Fig. 4.7. Power ramp test (full power, SCR=1) ..... 76
Fig. 4.8. Power transferring capability ..... 77
Fig. 4.9. Parallel VSC power ramp test (full power, SCR=1) ..... 78
Fig. 4.10. Voltage dependent active current limit ..... 79
Fig. 4.11. Fault ride through ..... 83
Fig. 5.1. Schematic of VSC connected to power grid with power flow direction ..... 86
Fig. 5.2. Schematic circuit diagram for power flow analysis ..... 87
Fig. 5.3. The block diagram of the reactive power/AC voltage Droop control ..... 89
Fig. 5.4. Power ramp of the converter ..... 90
Fig. 5.5. P-V curve of converter connected to grid with different SCRs ..... 91
Fig. 5.6. Schematic of circuit with physical damping resistance ..... 92
Fig. 5.7. Power ramp test and capacitor voltage with physical damping resistance ..... 92
Fig. 5.8. Equivalent circuit of the system in the SRF with physical resistance $R_D$ ..... 93
Fig. 5.9. Equivalent circuit of the system in dq frame with virtual impedance ..... 93
Fig. 5.10. Block diagrams of virtual impedance control ..... 94
Fig. 5.11. Block diagram of the proposed virtual impedance control ..... 95
Fig. 5.12. Schematic block diagram of the proposed virtual impedance controller in the overall system ..... 95
Fig. 5.13 .Block diagram of the MIMO model of the system including the proposed control method ..... 98
Fig. 5.14. Root locus of the d-axis current without proposed virtual impedance based voltage stabiliser control ..... 99
Fig. 5.15. Root locus of the d-axis current with proposed virtual impedance based voltage stabiliser control ..... 99
Fig. 5.16. Root locus of the q-axis current with proposed virtual impedance based voltage stabiliser control ..... 100
Fig. 5.17. Root locus of the d-axis current for d- and q- axis gains of the virtual impedance ..... 101
Fig. 5.18. Power ramp test with the virtual impedance voltage stabiliser control embedded into the VSC control ..... 105
Fig. 5.19. The system configuration with fault location ..... 105
Fig. 5.20. Transient performance with virtual impedance stabiliser control ..... 106
Fig. 5.21. Power ramp test and transient performance with the proposed virtual impedance stabiliser control for relatively weak and strong grids ..... 107

Fig. 5.22. Root locus of the d-axis current with proposed virtual impedance based voltage stabiliser control ..... 108
Fig. 5.23. System Schematic including external stabiliser..... 110
Fig. 5.24. External stabiliser for weak grid stabilisation..... 110
Fig. 5.25. The external stabiliser for weak grid with impedance between the converter and stabiliser..... 111

Fig. A1. 1. Converter schematic model in Simulink..... 125
Fig. A1. 2. The Simulink implementation of the proposed d-axis current error controller added to the PLL output angle ..... 125
Fig. A1. 3. The vector current control model implementation in Simulink..... 126
Fig. A1. 4. The Simulink implementation of the proposed q-axis current error into the system ..... 127
Fig. A1. 5. The Simulink implementation of the proposed d-axis virtual impedance controller ..... 127

# List of Tables

Table 3.1. Parameters for the VSC connected to the grid ..... 49
Table 4.1. Parameters for the simulated VSC system ..... 66
Table 4.2. System initial parameters ..... 72
Table 5.1. System parameters for illustration ..... 90
Table 5.2. Model parameters for small-signal analysis ..... 97
Table 5.3. Proposed virtual impedance control parameters ..... 97
Table 5.4. Cable parameters ..... 109
Table 5.5. External stabiliser parameters for different impedances ..... 109
Table 5.6. Required energy from the storage unit for different impedances ..... 109

# 1. Introduction

Wind energy is one of the fastest growing electricity sources in the world [1]. For example in Europe, the wind counts for 51% of the newly installed power capacity in 2016. Also, wind energy is the second largest technology for power generation and the largest renewable generation with a total installed capacity of 153.7 GW by the end of 2016, accounting for 17% of the total installed power generation capacity [2]. For all the installed wind capacity in Europe, around 12.5 GW is offshore wind [3], and the total installed offshore capacity is likely to increase to around 25GW by the end of 2020 [3]. However, the grid infrastructures are not ready for this significant amount of offshore power as highlighted by a case in Germany where delays in grid connection have hindered the development of new offshore wind generation [2].

Therefore, it is vital to address the problems posed by the integration of a large amount of wind energy to the grid. In this chapter, a brief overview of wind energy generation and power electronics used for wind energy applications is presented. The scopes and contributions of this thesis are presented, and the overall organisation of the thesis is outlined.

## 1.1. Wind Generation Technology Background

Wind energy has been used for thousands of years for sailing ships, grinding grains, and pumping water [4]. Wind energy is used to generate electrical energy by using wind turbines [5]. A generic wind turbine and its components are shown in Fig. 1.1. Most of the commercially available wind turbines have three blades, and the power output of a wind turbine is calculated by (1.1) [4]

$$P = \frac{1}{2} C_p \rho V_w^3 A \tag{1.1}$$

where $C_p$, $\rho$, A, and $V_w$ are the power coefficient, the air density, the rotor swept area and the wind speed, respectively. As seen in (1.1), the power output of a wind turbine

can be increased by improving $C_p$, increasing the rotor size (i.e. increasing the swept area) and having a higher wind speed. The power output of the wind turbine increases with the cube of wind speed as seen in (1.1). Therefore, as the wind speed is higher in the offshore environment, construction of offshore wind farms is favourable for investors [6].

A generic power curve of a wind turbine is shown in Fig. 1.2, which shows that the wind turbine starts generating power when the wind speed becomes higher than the cut-in speed. Then, the wind turbine output is in accordance to (1.1) until the wind speed reaches the rated wind speed (i.e. within the below-rated region). At the rated wind speed, the wind turbine generates the full rated power of the turbine. As seen in Fig. 1.2, in the wind speeds higher than the rated speed (i.e. above rated region), the pitch angle of the wind turbine blades are increased to curtail the wind turbine output to the rated power of the turbine. Finally, if the wind speed increases above the cut-out speed (extreme winds), the wind turbine stops generating power to protect the turbine from structural failure.

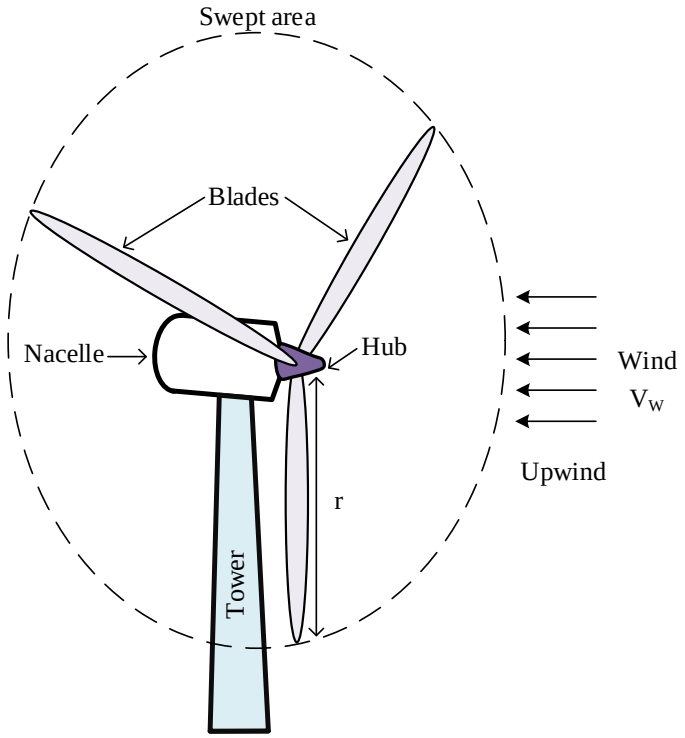


Fig. 1.1. Generic wind turbine

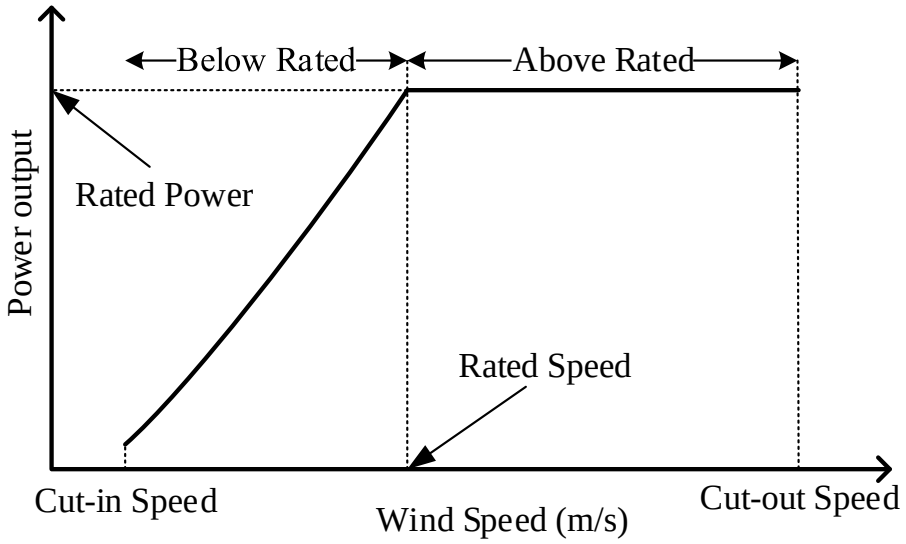


Fig. 1.2. Simplified power curve of a variable speed wind turbine

## 1.2. Wind Turbine Configurations

Different types of wind turbines have been utilised in last few decades and can generally be categorised into fixed speed and variable speed turbines [7].

Fixed speed wind turbines use induction generators with a squirrel cage rotor, and the simplified schematic diagram is shown in Fig. 1.3. A capacitor bank is connected to the turbine to provide reactive power to compensate the magnetising current of the machine [8]. To limit the inrush current to the induction generator at start-up, a soft starter is usually used [7].

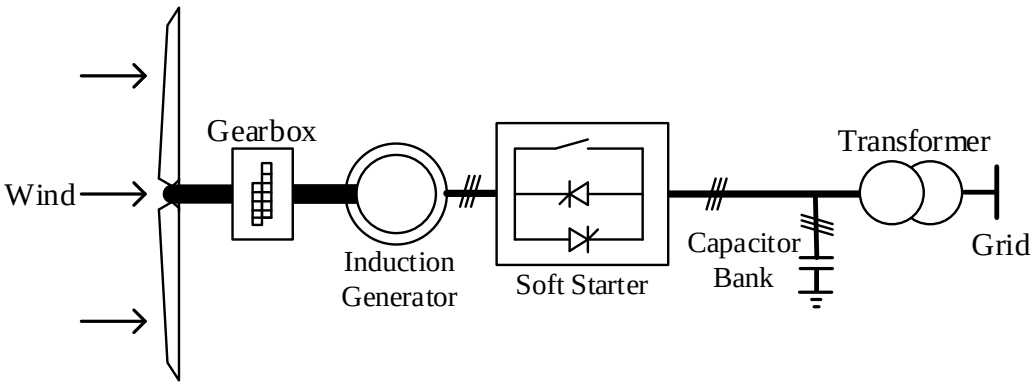


Fig. 1.3. Schematic diagram of a fixed speed wind turbine

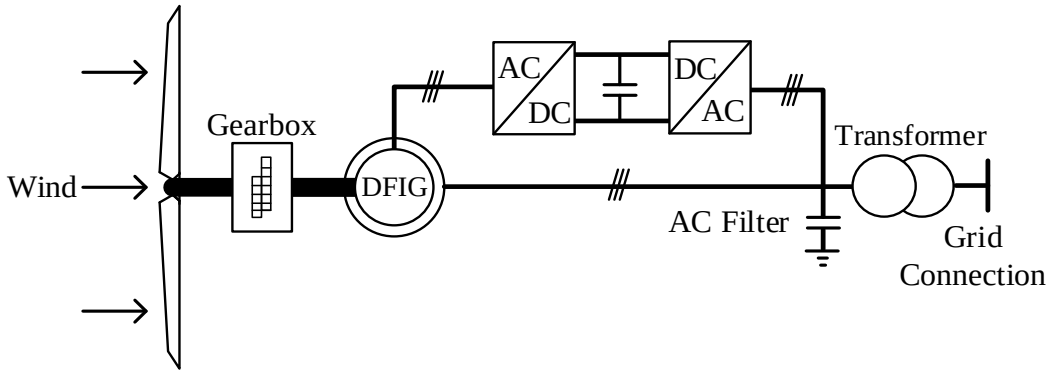


(a). Doubly fed induction generator (DFIG) wind turbine

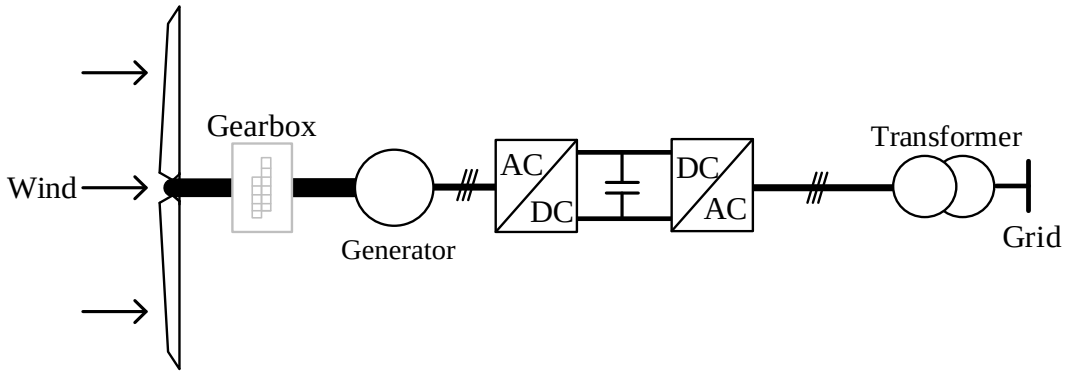


(b). Fully rated converter (FRC) wind turbine

Fig. 1.4. Schematic diagram of variable speed wind turbines

Variable speed wind turbines, in general, use power electronic converters between the turbine and grid which allow the turbine to operate over a wide range of rotational speeds [7]. Commercial variable speed wind turbines are mainly partial rated converters using doubly-fed induction generator (DFIG), and fully rated wind turbine as shown in Fig. 1.4 (a) and (b), respectively. These turbines provide greater efficiency compared to fixed speed turbines [7]. As seen in Fig. 1.4(b), in FRC wind turbines back-to-back voltage source converters (VSCs) are used for grid connection.

## 1.3. Transmission of Wind Power to the Grid

The power generated by a wind farm can be transmitted to the grid using either high voltage AC (HVAC) or high voltage DC (HVDC) transmission. HVAC transmission is the most straightforward option for connecting wind farms [9]. However, for offshore wind farms over a long distance, the cable capacitive charge current can cause large losses in the AC cables which will reduce the cable transmission capability, and

thus, reactive power compensation might be required. On the other hand, to decrease losses and increase transmission capacity the voltage level of the transmission lines should be increased but this increases the cost of equipment [10].

High voltage DC (HVDC) transmission is an alternative to conventional HVAC transmission, and the two HVDC technologies that are widely used are [7]

1. Line-commutated converter (LCC)
2. Voltage source converters (VSC)

The line-commutated converter has been used for more than half a century and is a mature technology [7]. LCC technology relies on the AC grid for commutation, and thus problems can arise during a fault in a weak AC grid [11]. The schematic block diagram of an LCC-HVDC transmission system is shown in Fig. 1.5 (a).

Voltage source converter technology is relatively modern compared to conventional LCC-HVDC. Self-commutated semiconductor devices, e.g. IGBTs, are employed in this type of converter. Using VSCs can provide some advantages over LCCs including independent control of reactive and active power, reduced filter size, faster dynamic responses, black start capability, no commutation failure, the possibility of weak grid integration, etc. [12-16]. The schematic block diagram of a VSC based HVDC system is shown in Fig. 1.5 (b).

## 1.4. Grid Integration of Wind Farms

The study of grid integration of wind energy becomes necessary as the share ofwind in the energy market has increased and the wind farms became large. Integration of wind power to the grid will impact the grid operation in different ways that will be briefly discussed in this section.

Wind energy is an intermittent energy source which means the output power of the wind farm can vary according to the weather conditions. As the power generation and demand at any time instant need to be balanced, this intermittency will impose limitations on power system operation. Hence, when a large wind farm is connected

to the grid, the requirement for the reserve generation to ensure reliable operation of the power grid is increased. This means that the associated cost of reserve generation in the power system will increase. Furthermore, as the share of wind energy in the total energy mix increases, the requirement for continuous frequency regulation will increase [17].

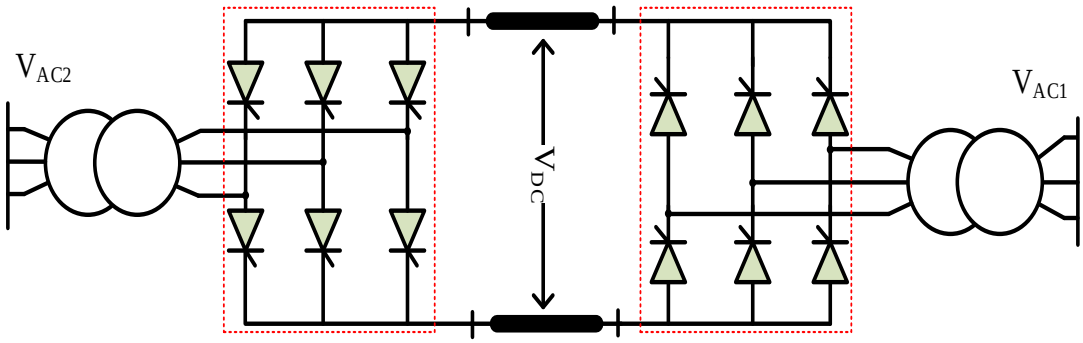


(a). Line commutated converter (LCC)

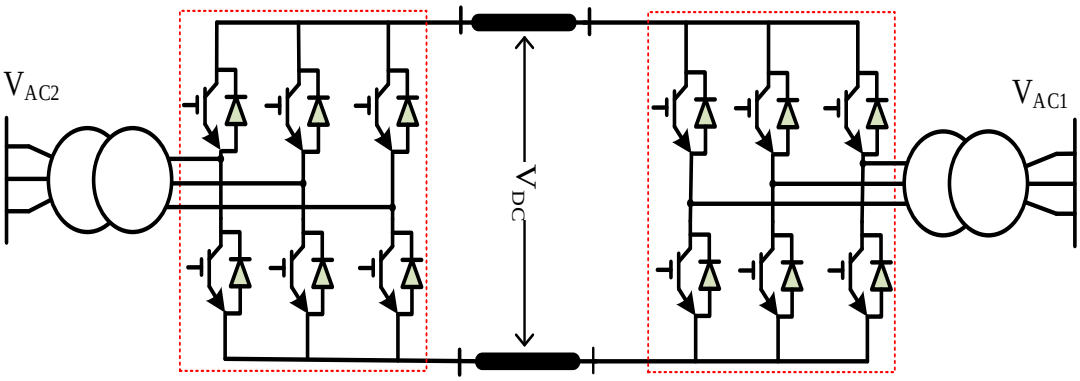


(b). Voltage source converter (VSC)

Fig. 1.5. Different power electronic converters

In addition, as in variable speed wind turbines, the electrical and mechanical parts are decoupled by the power electronic converters, and the wind turbine cannot contribute to the total inertia of the power system. Therefore, increasing the penetration of wind energy will have adverse effects on power system frequency response [18].

Large-scale wind farms are integrated into the system at very high voltage levels. As the main locations of wind farms become further away from the load centres, the grid connections in these areas are typically weak which can cause various problems to the system. These problems include excessive voltage drop or rise at the point of connection [19, 20], voltage flicker due to the variation of the output power of the wind

farm caused by wind speed variation, connection and disconnection of the generation, tower shadow, etc. [20]. Furthermore, grid integration of a large wind farm and injection of a large amount of active power into grid can cause instability if the connection is not strong.

## 1.5. Research Scope and Contributions

### 1.5.1. Research Scope

The main purpose of this thesis is to investigate the stable operation of wind farms connected to a very weak grid. In large wind farms, fully rated wind turbines are commonly used in which VSCs are used for grid integration. Therefore, in this study, such wind turbines are considered, and their grid side converter control is investigated for the stability study and enhancement of grid integration.

The main objectives and scopes of this research are as follow:

- To provide a comprehensive literature review on the stability of VSCs connected to a weak grid, including stability assessment, causes for instability, methods for stability improvement, etc.
- To develop a frequency domain model of the grid side converter of the wind farm for conducting stability studies of the grid connected VSC. The frequency domain model needs to include all the dynamics of the system, e.g. grid connection circuit, current controllers, power/voltage controller, phase locked loop, etc.
- To develop the frequency domain model of multiple converters for representing large wind farms so that the stability of multiple converters in the wind farm can be studied.
- Develop methods to improve the stability of the grid connected VSC and allow stable operation under very weak grid conditions. These methods are required to improve the transient performance of the VSC during different operating conditions.

### 1.5.2. Thesis Contributions

In this thesis the main contributions are:

- A frequency domain model of parallel VSCs is developed where the d-axis of the synchronous reference frame is aligned with the grid voltage instead of the filter capacitor voltage of each VSC. Thus, all the VSCs have the same reference frame, and any number of parallel VSCs can be added to the MIMO frequency domain model, making stability study simple and easy.
- A novel control method based on the classic VSC vector control of the VSC, which uses the current errors to calculate compensation terms for the PLL angle and the voltage amplitude, is proposed. The method enables the VSC to operate and transfer the rated power during normal and transient conditions without the requirement of any control mode switch. Compared to other methods in the relevant literature, this approach is very simple to implement, and as the current control loop is always in place, the VSC is able to control the current during transients. This control method can maintain the stability of the system without the need for changing the controller gains, even if the strength of the connected AC system changes during the operation. The proposed control method can also be used to control any type of VSC interfaced renewable energy system.
- A control method based on active damping of the voltage oscillations using virtual impedance is developed. This controller works as an extra outer control loop for the vector current control. Based on this principle, an external stabiliser device is proposed that can be utilised and connected to a weak point of the grid and allows a large amount of VSC interfaced power generation (e.g. wind power) to be connected to the grid. This proposed control method can also be used to control any type of VSC interfaced renewable energy system such as solar energy.

## 1.6. Organisation of the Thesis

This thesis is organised as follows:

- In chapter 2, the literature review on wind farm integration to the weak grid is presented. This review includes some general issues for wind integration, control methods for grid connected VSC, causes of the instability when connecting VSCs to the weak grid, and different methods for stability improvement.
- In Chapter 3, a comprehensive frequency domain model of a grid connected VSC is developed that includes the dynamics of every component, e.g. current controller, phase locked loop, switching delays, etc. Furthermore, a frequency domain model of parallel VSCs connected to the grid is also developed.
- In Chapter 4, a control method for the VSCs connected to the weak grid is proposed based on the d-q axis current errors to compensate the output angle of the PLL and the voltage amplitude. In this method, the main structure of the classic vector control is maintained. Detailed analysis of the proposed control method is presented using the root locus method, time domain simulations, etc. In this chapter, the proposed controller is tested under different operational scenarios including power ramps, AC faults, multiple converters, and different grid strengths.
- In Chapter 5, an active damping method based voltage stabilisation control is proposed as the complementary outer control in the vector current control. This method also provides stability to the VSC during normal and transient conditions when the VSC is connected to a weak point of the grid. In this chapter, analysis of the proposed method is conducted using the root locus method. Extensive simulations are conducted including power ramps, AC faults, multiple converters, and different grid strength. Finally, in this chapter, an external stabiliser based on active damping is proposed that can be used to enhance the stability of the grid.
- Chapter 6 draws the conclusion of this thesis, and potential future works for the continuation of this research is presented.

# 2. Background and Literature Review

In this chapter, a comprehensive review of the integration of wind farms to weak grids is presented. A general overview of issues related to wind farm integration is presented first, which is then followed by a discussion on grid strength. The control methods for grid connected VSC are reviewed, and finally, control methods for mitigating the issues of VSC weak grid integration are discussed.

## 2.1 General Aspect of Wind Farm Integration to the Grid

Integration of a wind farm to the grid consists of inter-array transmission to the wind farm substation and then transmitting the wind farm power to the grid. Different inter-array layouts can be used, and the wind farm power can be transferred to the grid by AC or DC lines. The medium voltage level (33-36kV) is typically used for the inter-array connection, and then higher voltage levels are used for transmission to the grid [10].

The sizes of the recently developed or consented wind farms are becoming large. For example in Europe, the average size of wind farms has been doubled in the period of 2010-2015 from 155.3 MW in 2010 to 337.9 MW in 2015 [21]. The increase of wind farm size has caused many issues for the collection of wind power and integration to the main grid [22]. One of the issues is that the amount of the inter-array cables in the wind farm is tremendously increased, potentially introducing stability problems to wind farm integration [23]. Therefore, the wind farm energy collection system and integration need to be designed in a way that minimises the potential problems.

Various issue including power losses, economic considerations, reliability issues, dynamic performance, and the transient and small-signal stability of different collection systems for wind farms have been studied in the literature [22-30]. The desired collection grid can be selected based on different considerations, e.g. size of the wind farm, desired reliability and stability level, and power losses in the wind farm [22]. Since the repair downtime for offshore wind farms is higher than that for the

onshore ones, adding redundancy to the power flow paths is essential for offshore wind farms to provide a high level of reliability [23, 30]. The collection grid of the wind farms can be designed with the same architecture as distribution systems. The collection system can be designed either in AC or DC configurations [30] though currently only AC is used. The main AC collection grid configurations are shown in Fig. 2.1 [4]. Each of the collection grid configurations has its advantages and disadvantages.

In a star configuration, as shown in Fig. 2.1.(a), the rated power of cables is low since the cables are required to transfer the power of only a single turbine. This configuration offers a great reliability as in the event of a wind turbine failureas the other wind turbines will not be affected.

The simplest topology for a collection grid is the radial or string configuration, as illustrated in Fig. 2.1.(b). This configuration does not offer any additional power path, and therefore, when a fault occurs, downstream turbines will lose the connection to the grid [23, 31].

Fig. 2.1.(c) and (d) depict the schematic diagram of a single sided ring collector and a double sided ring collector, respectively. The ringed configurations offer a high level of reliability by adding an additional power flow path. The single sided topology provides the additional path at the expense of using a greater amount of cables. The double sided ring topology provides the additional power flow path by connecting the last turbine in a string to the last turbine of the neighbouring string [22]. However, the cables need to be rated high enough to be able to transfer the power from two adjacent strings. Therefore, the cable cost will be increased.

## 2.2. Grid Strength

A power system is defined as being weak if the equivalent impedance of the AC grid is high or the mechanical inertia of the AC system is low [32]. In this section, these two types of weak power systems are reviewed.

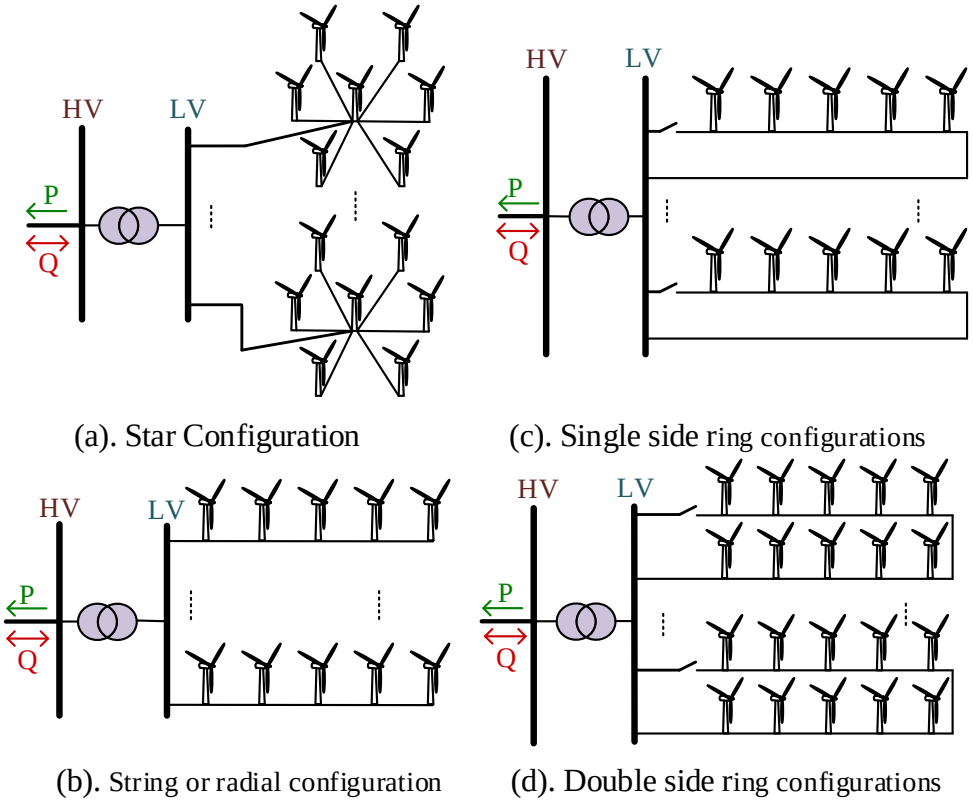


Fig. 2.1. Wind farm AC collection grid topologies [23]

### 2.2.1. High AC System Impedance

The power system strength can be measured by the short circuit ratio which is the ratio of the short circuit capacity at a specific point of the grid to the nominal power of the generation/equipment/system (e.g. converters) connected to the grid at that point [33]. This index is often used in the planning and design stages to understand the potential issues that might occur by installing equipment to the grid [33].The SCR at the connection point is then calculated as [32]

$$SCR = \frac{S}{P_d} \tag{2.1}$$

where S is the short circuit capacity (SCC) of the AC grid and $P_d$ is the rated power of the connected equipment/device/generation. Assuming the rated power of the wind farm as the base power for the per unit calculation, the SCR can also be calculated as

$$SCR = \frac{1}{Z_{Net}} \tag{2.2}$$

where $Z_{Net}$ represents the per unit impedance of the grid seen at the connection point [33]. A power system with SCR greater than 3.0 is considered as a strong system, and systems with 2<SCR<3 and SCR<2 are categorised as weak and very weak systems, respectively [32]. The sensitivity of the power system to the active/reactive power change increases by the reduction of the SCR [33].

Other than the short circuit ratio, the other often-used metric for measuring the strength of the grid is the ratio of the inductive and resistive parts of the grid impedance (X/R ratio). The value of the resistive and inductive parts of the grid impedance can be calculated by [32]:

$$\begin{cases} X_{Net} = \frac{Z_{Net}}{\sqrt{1+\left(\frac{1}{XRr}\right)^2}} \\ R_{Net} = \frac{Z_{Net}}{\sqrt{1+(XRr)^2}} \end{cases} \tag{2.3}$$

where XRr is the X/R ratio of the grid. The ohmic part of the grid impedance in weak grids is relatively high, so the X/R ratio is small.

### 2.2.2. Low Inertia

As mentioned earlier, the other type of weak grid has low AC grid mechanical inertia compared to the installed equipment (e.g. converter or wind farm, etc.) at the point of connection. For a system with generation mainly from synchronous generators, inertia is defined as the total amount of kinetic energy stored in all spinning components (e.g. turbines and rotors) in the system [34].

During power disturbances, the inertia constant of the power system determines the transient frequency behaviour of the system [35]. The inertia constant is defined as the time in seconds taken by the generator to replace the stored kinetic energy during operation at the rated speed and apparent power output [36].

The inertia constant of a system can be obtained by using the swing equation in which the frequency and power balance are measured in the event of active power imbalance [36]. The swing equation can be written as [37]

$$\begin{cases} \frac{2H}{\omega_0}\frac{d\omega}{dt} = P_G - P_l \\ \frac{d\delta}{dt} = \omega - \omega_0 \end{cases} \tag{2.4}$$

where H represents the inertia constant, and $P_G$ and $P_l$ are the power generation and load within the system, respectively. $\omega_0$ is the angular frequency of the system and $\delta$ is the rotor angle for a single machine system.

As previously mentioned, variable speed wind turbines are widely connected to the electrical grid using power electronic converters, meaning variable speed wind turbines (e.g. DFIG and FRC) cannot provide inertia to the power system as their mechanical and electrical systems are de-coupled by the converter interface. Thus, the kinetic energy that is stored in the blade of the wind turbines will not appear in the grid [18]. Therefore, if a power system contains a significant amount of converter interfaced wind farms, the equivalent inertia of the power system will be significantly decreased.

## 2.3. Grid Connected VSC Control

For FRC based wind farms, the controller of the grid side VSC is responsible for ensuring reliable and satisfactory system operation during different operating and grid conditions with adequate power quality, and for ensuring grid code compliance for the connection.

The main objective of the controller is to modulate the converter output voltage with controlled magnitude and phase angle to control active and reactive power at the grid connection point [38]. VSCs use self-commutated semiconductor devices which are turned on and off by gate signals. By changing the gate signals (i.e. duration of the on/off time) the output of a VSC can be controlled. Gate signals are generated using pulse width modulation (PWM), which may be defined as the control of the average

level of a quantity by applying or driving that quantity in discrete intervals or pulses [39]. There are different PWM techniques, e.g. sinusoidal, space vector, and hysteresis PWM, etc. [40, 41]. However, the most popular PWM technique uses a sinusoidal reference signal as shown in Fig. 2.2, where the converter reference voltage waveform is compared to a high-frequency triangular waveform to generate gate signals. Different methods have been proposed in the literature to control grid connected VSCs. In this section, two main control methods that are used for grid connected VSCs, i.e. direct power control and vector current control, are reviewed.

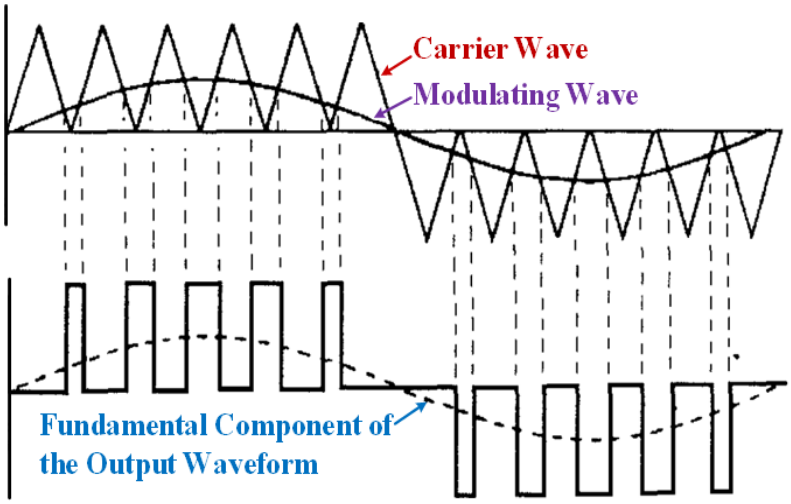


Fig. 2.2. Pulse width modulation with sinusoidal reference [40].

### 2.3.1. Direct Power Control

In this control method, the active and reactive power of the converter is controlled using the principles of the direct torque control (DTC) of electrical machines [42-53] and the control scheme is accordingly named direct power control (DPC). These methods can be based on virtual flux calculated from the integration of the voltage [42-47], or the active/reactive power errors in combination with the converter voltage angle [48-50]. This method has different variations in which the switching frequency either varies due to the variation in the grid conditions [47-50], etc. or is kept constant [42-44, 51-53]. In the control method with varying switching frequency, the AC harmonic filter needs to be designed for a wide bandwidth, leading to reduced efficiency of the filter and larger filter size [44].

Furthermore, some of the proposed methods in the literature [42, 46, 54] use estimation or prediction based approaches to calculate the required parameters (e.g. virtual flux [42], active and reactive power [46, 54], stator flux angular position [55], etc.) to be used in the control process. The performance and accuracy of this method are significantly dependent on the model that is used for parameter estimation.

### 2.3.2. Vector Current Control

Vector current control is used in most practical VSC industrial applications [44, 56]. The control strategy for a grid connected VSC having the requirement of controlling its DC link voltage and AC voltage usually consists of two levels of cascade control loops. The first control loop is a fast inner loop controlling the current. This control loop also deals with protection and power quality and dynamic issues. The slow outer control loop controls the DC link/AC voltage by regulating active/reactive power flow between the grid and the converter [57]. By using rotating synchronous d-q frame transformation, AC current and voltage effectively become DC quantities for ease of control. However, it is possible to control the current in $\alpha\beta$ or abc stationary frames [56]. By controlling the current in the stationary frame, the controlling signals are sinusoidal for which PI controllers have difficulty in to eliminating steady state error. Therefore, proportional resonant (PR) controllers have been proposed which have very large gains in the vicinity of the resonance frequencies (line frequency in this case) to eliminate the steady state error [57-59]. The modelling and operational concept of vector current control are discussed further in Chapter 3.

### 2.3.3. Grid Synchronisation

Grid connected VSCs need to be synchronised to the main grid. In VSC applications, the synchronisation should be updated continuously (in contrast with thyristor valves, where synchronisation just needs to be updated at zero crossing points) [60]. Poor synchronisation results in significant performance reduction. For example, a phase shift in the synchronisation scheme can lead to steady state current and power errors. For the grid synchronisation of a VSC, different open loop and closed loop methods have been used [60-73]. A commonly used method for grid synchronisation is via a

phase locked loop (PLL) that extracts the phase and frequency information of the grid voltage. This information is later used inside the controller to convert three-phase current and voltage into synchronous reference frame (SRF) variables, and vice versa [61-63].

## 2.4. Control of VSC Connected to Weak Grid

As most of the newly constructed or planned wind farms are located in rural areas or offshore which are far from main conventional power plants, the electrical distance of the connection point to large synchronous generators is increased, and thus the grid strength at the connection point becomes weak. On the other hand, the rated power of newly constructed wind farms is becoming larger, and thus a large amount of active power needs to be injected to a weak point of a grid which becomes problematic or even impossible. From an economic point of view, tackling this issue from the VSC control aspect will be very advantageous to the power grid owner as it will ease the requirement for reinforcing the grid.

A VSC (e.g. wind turbines) with vector current controller connected to a weak power grid can potentially become unstable, and the active power transfer capability of the converter to the grid might have to be limited, e.g. to 60-70% of the converter rated power [74, 75]. For a weak grid, the voltage is very sensitive to both active and reactive power changes. Thus, voltage magnitude and phase angle stabilisation after a power change in a weak grid are necessary [33].

The aforementioned instability problem of VSC connected to a weak grid can be induced by the performance of the PLL in interaction with other components of the power system [16, 76-81], which might lead to positive feedback and cause causing instability [77]. Furthermore, The PLL gains significantly impact the operation of VSC connected to a very weak grid. For a VSC connected to a very weak grid, the theoretical operation limits cannot even be met even if PLL gains are very small [78]. Therefore, the PLL impacts the stability of the system. In addition, the lack of ability of the system to provide enough reactive power to the connection point in order to stabilise the PCC voltage can also lead to system instability [82-84].

To resolve the instability issue of VSC connected to the weak grid, a number of strategies from a grid point of view can be considered, e.g. reinforcing the grid, using extra compensations, etc., though they all require additional investment [82, 85]. The other option to tackle the stability issue of weak grid connection is to improve the VSC controller. In this section, different control methods are reviewed, and the control methods to enable stable operation when connected to a weak grid can generally be categorised into the following two groups:

a. Vector current control based control methods
b. Synchronous generator based control methods

### 2.4.1. Vector Current Control Based Control Methods

In these methods, the main structure of the vector control is maintained, and various control elements are added/modified to improve system stability. The adopted approaches can generally be categorised into three areas as follows.

A. PLL Tuning

As previously mentioned, the unstable behaviour of the converter when it is connected to a very weak point on the grid can arise from the performance of the PLL due to its inability to satisfactorily track the grid voltage angle. Consequently, the angle measured by the PLL differs from the real angle of the grid terminal voltage, potentially causing system instability. Therefore, the PLL phase error needs to be addressed [80, 81, 86]. The parameters for the PLL, therefore, need to be tuned in a way that the angle tracking has satisfactory accuracy, robustness, and speed [81]. There are two options for re-tuning the PLL, i.e. slowing down or speeding up the response.

It is possible to re-tune the control system to slow down PLL response and at the same time speed up the voltage regulator to improve the power transfer capability of VSC connected to a weak grid [87]. However, If the PLL gain is decreased to reduce the PLL bandwidth (i.e. slowing down the PLL), it can cause a poor and slow dynamic

response [78, 86]. Therefore, this re-tuning method is not capable of maintaining the stability of the system when SCR (i.e. grid impedance) is significantly changed [87].

Alternatively, the PLL bandwidth can be increased. Hence, the PLL tracking capability is quickened. However, this will reduce the tracking performance during unbalanced operation [81].

B. Virtual PCC point based methods

In this method, an artificial point in the grid which is stronger than the filter bus (PCC) is introduced to synchronise the converter to the grid [83, 87] which means that the reference frame for synchronisation is changed.

In [83], the VSC is virtually synchronised with a strong virtual point of grid voltage through including an impedance-conditioning (IC) term to the PLL as shown in Fig. 2.3. As shown in Fig. 2.3, to synchronise the PLL to the voltage of a remote point, the voltage drop across the virtual impedance in the d-q reference frame is deducted from the measured voltage of the PCC. In this method, the current at the PCC is also used as an input for the IC_PLL. To avoid over-modulation, the virtual impedance needs to be selected relatively low. This method improves the steady state behaviour, but transient stability (i.e. faults) is not considered in [83].

In [87], instead of using PCC voltage to feed into PLL for grid synchronisation, an arbitrary virtual bus between the PCC and grid is considered for grid synchronisation as shown in Fig. 2.4. The new system configuration has two new artificial values for filter and grid impedances so that the current control is adjusted to the new system configuration by recalculating the proportional gain of the current regulator based on the new filter impedance [87]. In this method, the artificial bus is selected to be purely inductive, so that the active power flow at the artificial bus is similar to that at the PCC. This method improves the steady state stability of the system, but the performance of the controller in the transient conditions (e.g. faults) is not considered in [87].

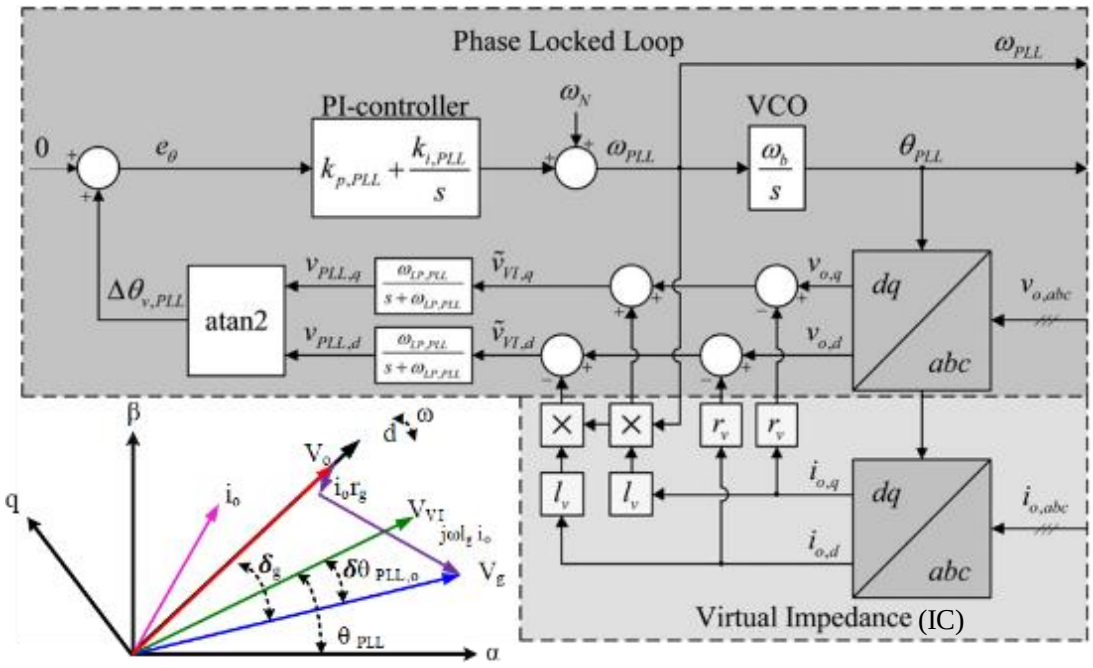


Fig. 2.3. Schematic diagram of IC-PLL [83].

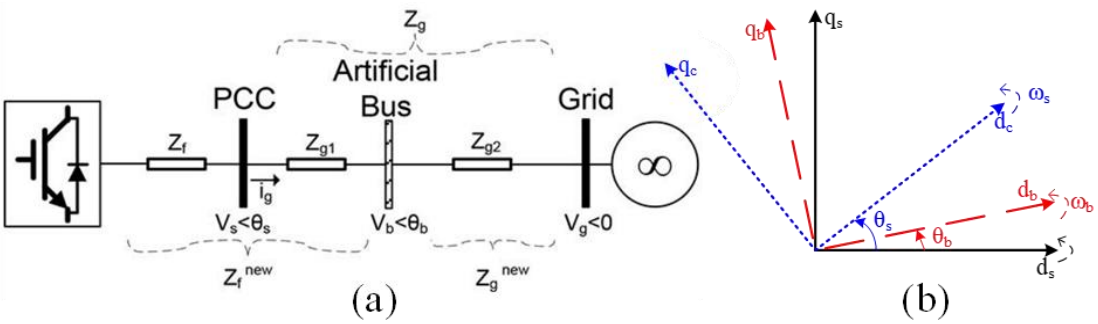


Fig. 2.4. Schematic diagram of the artificial bus method for grid synchronisation, (b) dq-reference frame representation of the artificial bus method [87].

C. Re-design of the outer control loops

An advanced vector control for VSCs connected to weak grids is presented in [74], where the inner current regulation loop is maintained. Therefore, this method benefits from the advantages of closed loop current control, i.e. current regulation during faults or transients. As the voltage/power interaction has been identified as one of the main

causes for the instability of VSC weak grid connection, a new decoupled upper-level control loop (power/voltage) based on gain scheduling to overcome the problems of the interactions between active power and voltage controllers is introduced as shown in Fig. 2.5. In this control, the nonlinearities of the system have been considered, and the outer control loop is a multi-variable controller with four decoupling constants ($k_1$-$k_4$) between voltage and power error, as seen in Fig. 2.5.

The PI controller and the decoupling gains ($k_1$-$k_4$) are tuned based on the gain-scheduling technique, where 35 different operating points are considered to tune the eight different parameters (decoupled gains and PI controllers). This control method provides a promising approach for weak grid VSC integration. However, it requires very complex tuning for each operating point. Furthermore, if the grid strength changes during the operation of the VSC, this method is not able to properly control the VSC.

### 2.4.2. Synchronous Generator Based Controller Schemes

Integration of synchronous generators to the electrical grid has been studied extensively over decades, and synchronous generators impose no limitation for connection to the weak grid as they provide inertia and damping to enhance stability. Various VSC control methods have been proposed for VSCs to imitate synchronous machine behaviour [75, 88-94], e.g. virtual synchronous machine (VISMA) [89], virtual synchronous generator (VSG) [88, 94], “synchronverter” [91, 95], power synchronisation control (PSC) [75, 92], etc. [90, 96].

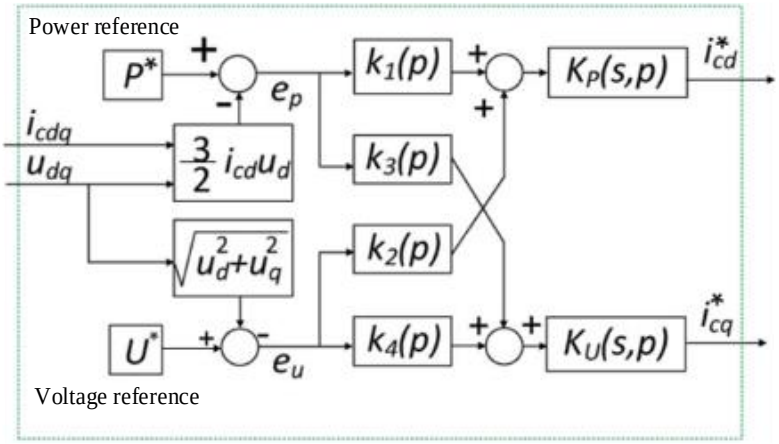


Fig. 2.5. Advanced outer loop control [74].

A. Virtual Synchronous Machine (VISMA) and Virtual Synchronous Generator (VSG)

The virtual synchronous machine based methods for controlling the power electronics converters are mainly developed to provide virtual inertia to the system, to ensure stable operation of the converter in islanded and grid-connected conditions without changing the structure and parameters of the converter controller [97]. Such methods try to emulate the behaviour of the synchronous machine, and different implementations have been proposed in the literature [88, 89, 94, 96-108]. These methods can be categorised based on the different reference signal that the mathematical model of the synchronous machine provides for the converter controller. Mathematical models that are used to implement virtual synchronous machines can have either current or voltage as the output of the virtual synchronous machine [97], as is shown in Fig. 2.6.

The first group of this family of controllers, in which the synchronous machine is mathematically modelled by a 'voltage to current' model of the synchronous machine, is shown in Fig. 2.6(a) [89, 98, 100, 109, 110], where, the input and output of the virtual synchronous machine model are voltage and current, respectively.

The other option for the mathematical model of synchronous machine is based on its internal electrical dynamics that gives voltage as the output. An example of this is shown in Fig. 2.6(b) in which a 'current to voltage' model of the synchronous generator is used [100]. By using the current to voltage model of the synchronous machine, the output of the synchronous machine model is a voltage that is calculated from the measured current of the converter which is then used in the implementation of the virtual synchronous machine as a reference signal [90, 100, 107, 111].

One of the implementations of the virtual synchronous machine is VISMA which usually consists of a generator (source), energy storage on the DC side, and a hysteresis-based control, as demonstrated in Fig. 2.7 [89]. In VISMA the phase currents are calculated from the measured PCC voltage. The calculated current is then used as the reference in the inverter [89, 100]. In VISMA, the active and reactive power

exchange to and from the grid can be regulated by adjusting the voltage and frequency at the connection point to the grid, which is similar to the synchronous machine. Such a control strategy can limit current, though it is difficult to tune the hysteresis controller to accommodate both steady state and transient conditions.

The virtual synchronous generator (VSG) method also emulates synchronous generator behaviour by providing virtual inertia and damping to the system. The VSG provides virtual inertia to the system by using a short-term energy storage [88, 94]. In this method, the power flow to/from the storage is regulated by the grid frequency deviation [88, 94]. Fig. 2.8 shows a schematic diagram of VSG. This method helps to improve the short-term stability of the system frequency [91].

In contrast to the discussed methods for emulation of the synchronous machines in which the control equation includes electrical dynamics of the synchronous machine, the controller can be implemented based on the quasi-stationary representation of the stator windings of the virtual synchronous machine [101, 108]. As the electrical dynamics equations of the virtual synchronous machine are neglected, this group of controllers offers simplicity for implementation.

All the control methods discussed in this section offer similar steady state behaviour [97]. The virtual synchronous machine based control methods can provide good inertial support to the grid providing sufficient energy storage is available. However, as a current control loop is not available in most of them except VISMA, the operation of the system under transient conditions could become problematic. In VISMA, the current can be limited, however the tuning of the hysteresis controller for operation during both steady state and transient operation is very difficult.

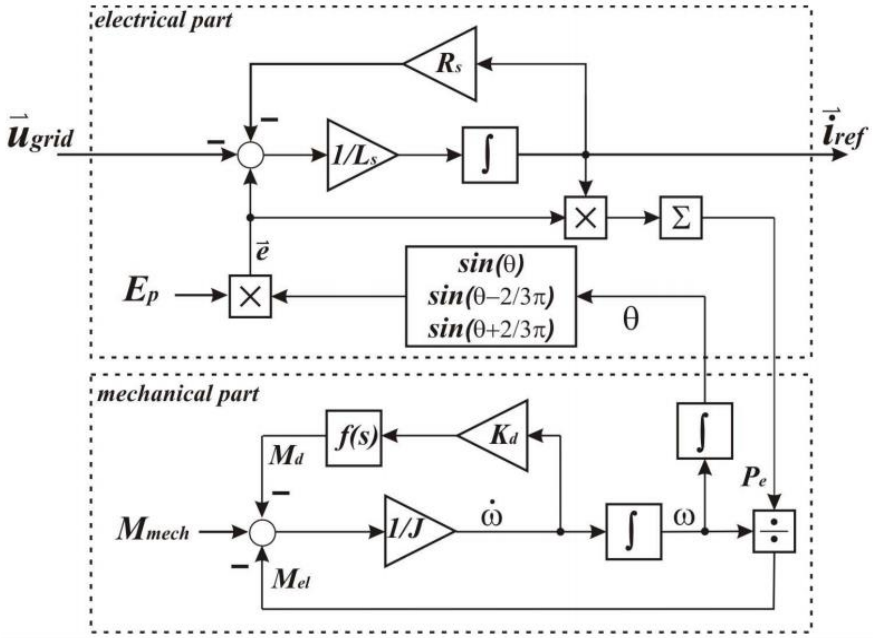


(a). Voltage to current model

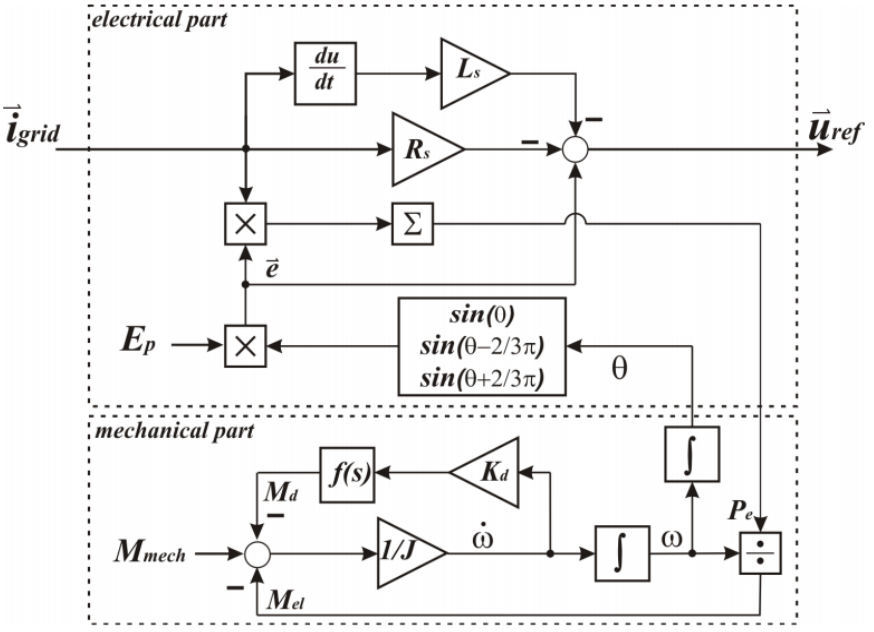


(b). Current to voltage model

Fig. 2.6. Different models of the synchronous machine for VISMA implementation [100].

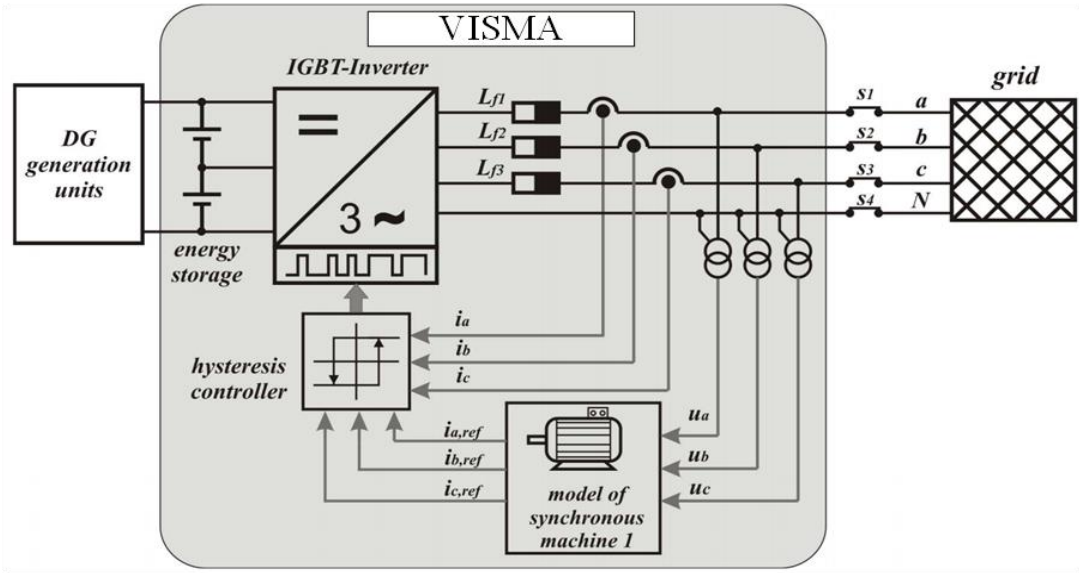


Fig. 2.7. Components of VISMA [100].

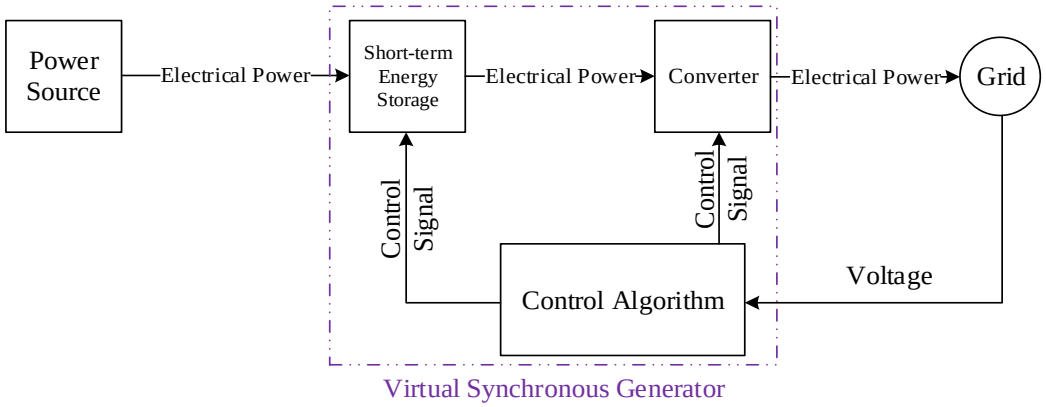


Fig. 2.8. Schematic Diagram of VSG [88].

B. Synchronverer

The other method that has been proposed in the literature to emulate synchronous generator behaviour is called the synchronverter which is designed based on an embedded mathematical model of a synchronous machine providing a voltage supply [91]. The control block diagram of the synchronverter is shown in Fig. 2.9. The synchronverter, in reality, behaves like a synchronous generator with a small capacitor connected in parallel to the stator of the generator [91]. The synchronverter controller is fundamentally a power controller with the additional capability to regulate voltage and frequency. In this method, to regulate the DC voltage, a DC voltage controller

with an energy storage device is required. As a synchronverter mimics the synchronous generator, some of the undesirable behaviour of synchronous machines can occur, e.g. loss of stability because of under-excitation, and 'hunting' [91].

In [93], a modification to the synchronverter was proposed which adds self-synchronising capability to the original synchronverter by eliminating the PLL from the control system, and hence, it is called a 'self-synchronised synchronverter'. The converter behaves similarly to a synchronverter, but different switches are used to achieve the self-synchronisation characteristic. This might add some complexity to the system.

Furthermore, an improved synchronverter is introduced in [95] to compensate the terminal voltage, as this voltage drops in the original synchronverter due to the different resistances of the simulated synchronous generator stator and the converter circuit. An advantage of this method is that the controller enables the converter to be synchronised with the grid under different operational conditions, e.g. synchronising before connecting to the grid. Similarly to VISMA based methods, one of the main problems with of the synchronverter [91, 93, 95] is the absence of the current control loop which means that there will be current regulation issues during over-current conditions (i.e. faults, transients, etc.).

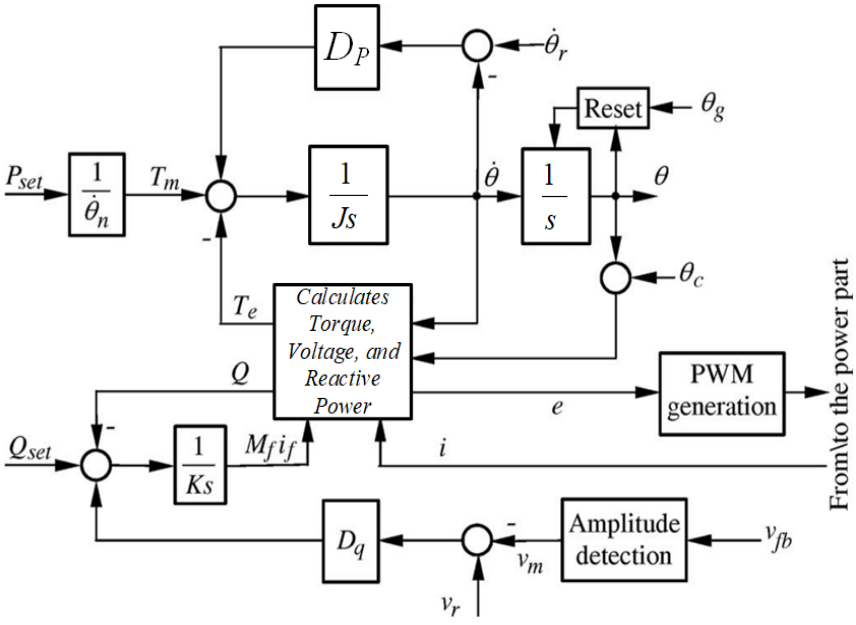


Fig. 2.9. the schematic control block diagram of synchronverter [91].

C. Power Synchronisation Control (PSC)

References [75, 92] introduced a control strategy called ‘power synchronisation control (PSC)’ that improves the power transfer capability of converters connected to weak grids. This control method emulates the swing equation of the power system and similar to synchronous generator control, closed-loop power control is performed by directly controlling the modulation voltage angle and magnitude of the converter voltage. In this case, the PLL is by-passed during steady state operation. The schematic control block diagram of the power synchronisation loop (PSL) and the overall control structure of a VSC based on PSL are shown in Fig. 2.10 and Fig. 2.11, respectively.

As the power synchronisation control process involves an unknown current that is defined by the interconnected grid, the vector current control loop which needs a current reference cannot be used. However, the absence of current loop can potentially give rise to extra current variations during perturbations. Thus, during a fault, the control system needs to switch to a current-loop based control mode with a backup PLL [75]. Such a non-linear mode switching scheme increases the complexity of VSC control. One consequent problem is that it is difficult to determine how the switching point should be set in order to avoid undesirable mode switches, especially during unpredictable perturbations, such as voltage fluctuations or faults, when the VSCs are operating near their rated power/current.

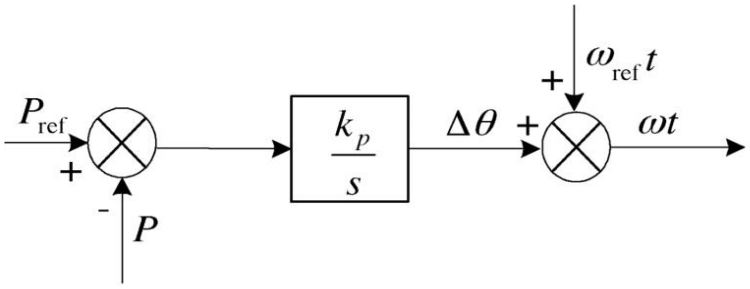


Fig. 2.10. Schematic diagram of a Power Synchronisation loop [75].

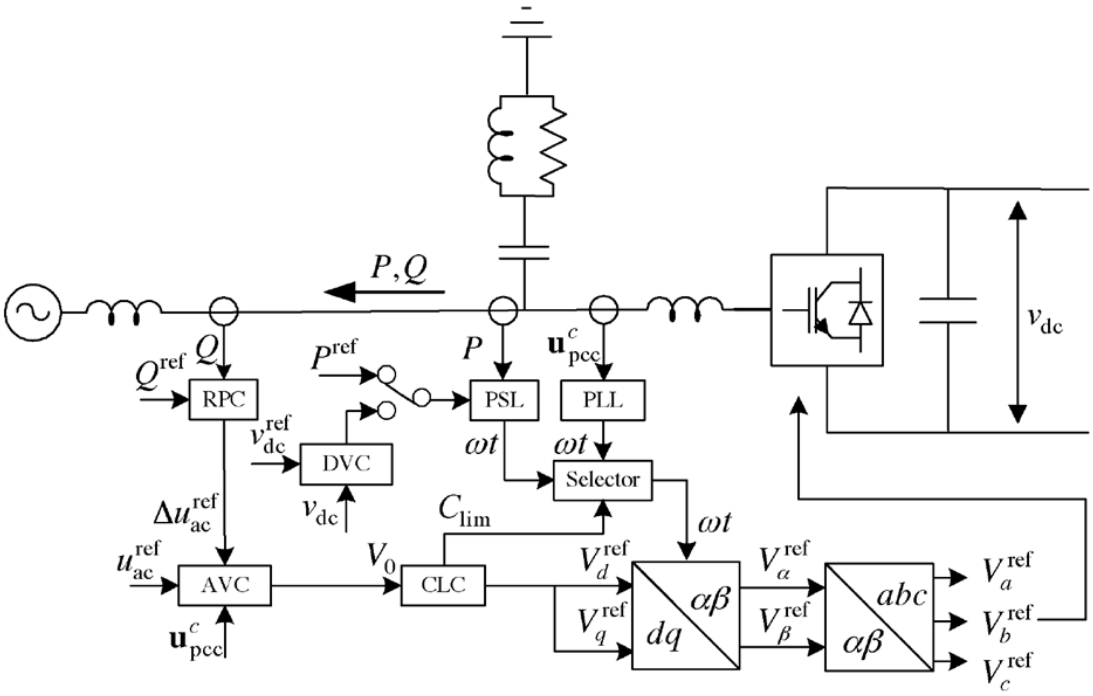


Fig. 2.11. Control diagram of VSC based on PSL [75].

## 2.5. Summary

In this chapter, grid integration of VSC interfaced wind farms has been reviewed with particular emphasis on weak grid connection. The general aspects of wind turbine integration to the grid are reviewed, followed by definition of a weak power grid. Then, the control strategies for the integration of the VSCs to the grid are introduced, including direct power control and the well-known vector current control. Problems arising from the integration of VSC to a weak grid are discussed, and two main factors are identified as the causes of the constraints on the VSC active power transfer capability. These two factors are the small signal stability problem largely due to the interaction of the PLL with other components of the system, and the active power/ voltage interaction. Finally, the control schemes that are proposed in the literature to overcome the issues of the integration of the VSCs to the weak grid are reviewed.

The control methods proposed for VSC weak grid operation are generally categorised into two groups. The first group of controllers is based on the well-known vector current control. These controllers maintain the main structure of the current control method with some parts of the controller being redesigned or re-tuned. One option to

maintain the control structure is to introduce a virtual integration point to synchronise the converter to a stronger point of the grid. A gain-scheduling based decoupled outer control loop is introduced which improves the performance of the VSC when connected to a very weak grid. However, this method increases the complexity of the controller re-tuning for each operating condition, therefore if the strength of the grid changes, the controller might face VSC control problem.

The second group of control methods tries to mimic the behaviour and control schemes of synchronous generators when they are integrated into the grid. This type of VSC control method is based on the fact that a properly-controlled synchronous machine can easily transfer bulk power from weak grid point, which has been studied for decades. These control methods also provide inertia response and frequency support to the connected grid. However, controlling the VSC as a voltage source as in a synchronous machine, does not directly control the converter output current which can become problematic during transient conditions, e.g. external and/or internal faults.

# 3. Modelling of Grid Connected Voltage Source Converter

In this chapter, vector current control is discussed, and the process of analytical modelling of grid connected voltage source converters in the frequency domain is presented. The model is established within the synchronous d-q reference frame where the d-axis is aligned to the grid voltage. To model the current control loop of the converter in the frequency domain, initially, a single converter connected to a grid through a converter reactor, step up transformer and cables is considered. A state-space model of multiple parallel converters is then developed to study the stability of parallel converters in a large wind farm. Finally, outer control loops of the VSC, such as those for active/reactive power and AC voltage, are modelled and added to the system. In this chapter, the phase locked loop (PLL) is integrated into the frequency domain of the converter to improve the accuracy of the analytical model.

## 3.1. Introduction

As mentioned in Chapter 1, variable speed wind turbines use voltage source converters (VSC) for grid connection. The most commonly used method for controlling grid connected VSCs is vector current control. However, problems can arise when the connected power grid is weak, and the systems can potentially become unstable [74, 75]. Many wind farms are being constructed in remote areas where the wind speed is high but the connection to the grid is weak. Furthermore, it is possible that the line impedance could increase further due to faults, variation in the load, and line trips [112].

Many studies have been conducted to evaluate system stability of grid connected VSCs [113, 114]. However, in [113, 114] the dynamics of the PLL, which can significantly affect system stability especially for weak grids [75], were not considered. In [115, 116] the analytical model of an HVDC system is developed to study the stability of an LCC-HVDC transmission link. In [115] the PLL is modelled by a state-space

representation, which is used in [16] to develop the analytical model of VSC-HVDC transmission. Also, in [117] an analytical model of VSC-HVDC is developed which includes PLL dynamics expressed by a state-space model. However, the d-axis voltage of the converter filter bus is selected as the reference for the d-q frame, and thus it becomes complicated when studying the dynamics of parallel converters since each converter model is developed based on its own d-q reference. In [118], PLL dynamics were added to the converter dynamic model by using synchronous machines theory, though the PLL dynamics were added to the feed-forward grid voltage rather than to the converter output voltage leading to inaccurate representation of the system. In [65], the dynamics of a PLL have been studied, but not as a part of the dynamic model of the VSC. The concept of a Jacobean matrix of the AC grid is introduced in [92] which can be used to study VSC converters with power synchronisation control, but it does not include PLL dynamics.

In this chapter, to investigate the stability of multiple grid connected VSCs, a state-space model is developed, and the actual dynamics of the PLL are integrated into the model. In the developed model, the d-axis of the synchronous frame is aligned to the source voltage, and the filter bus voltage at the VSC terminal is used to derive PLL dynamics for each converter. This ensures systems which contain a number of parallel connected VSCs can be modelled accurately by considering each PLL separately.

## 3.2. Vector Current Control

Fig. 3.1 shows a simplified schematic single-line diagram of a grid-connected VSC. The converter is connected to the grid through a converter reactor and transformer. An AC side filter is used to smooth out the harmonics generated by converter switching.
For integration of a VSC to the power grid, it is necessary to maintain a constant DC voltage (i.e. to be able to control the power flow) and also make AC voltage to comply with grid codes. However, power flow control and AC voltage control are both accomplished through controlling VSC current. The primary current control method for VSC is vector current control which was briefly discussed in Chapter 2 [44].

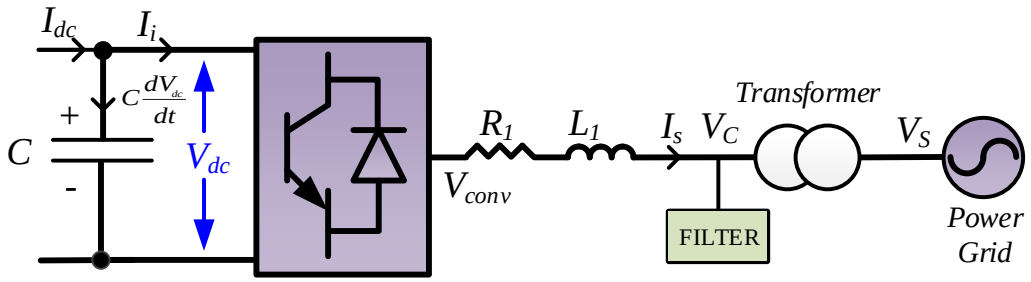


Fig. 3.1. Schematic diagrams of a grid connected VSC

A VSC connected to a simplified grid as seen in Fig. 3.2 (a) is used to derive the vector current control method. Fig. 3.2 (b) and (c) show the equivalent AC circuit in the synchronous reference frame rotating at an angular speed of $\omega_s$ and the DC equivalent circuit, respectively.

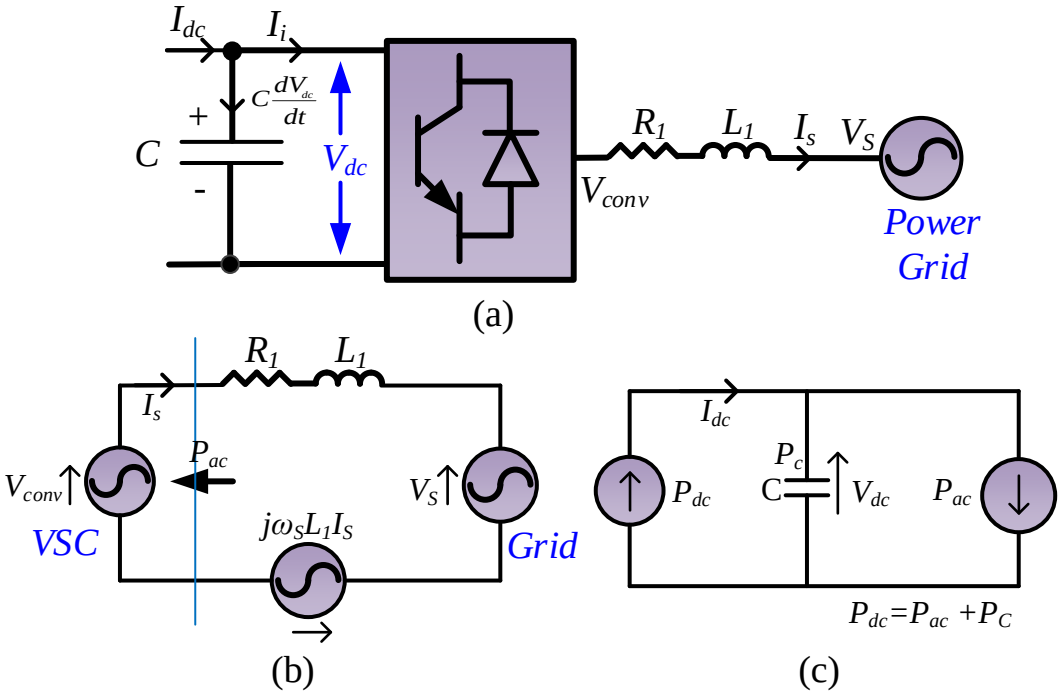


Fig. 3.2. (a) Schematics of a grid connected VSC. (b) AC equivalent circuit of the VSC in the synchronous reference frame (c) DC equivalent circuit of the VSC [119].

According to Fig. 3.2 (b), the system on the AC side can be expressed in the synchronous dq reference frame, where the d-axis is fixed to the source voltage $V_s$, as

$$\frac{d}{dt}\begin{bmatrix} I_{sd} \\ I_{sq} \end{bmatrix} = \begin{bmatrix} -R_1/L_1 & \omega_s \\ -\omega_s & -R_1/L_1 \end{bmatrix}\begin{bmatrix} I_{sd} \\ I_{sq} \end{bmatrix} + \frac{1}{L_1}\begin{bmatrix} -V_{sd} + V_{conv_d} \\ -V_{sq} + V_{conv_q} \end{bmatrix} \tag{3.1}$$

Neglecting the converter power loss, the DC system in Fig. 3.2 (c) can be expressed by considering power at the DC and AC sides being equal as

$$P_{dc} = P_{ac} + P_C \tag{3.2}$$

$$P_{ac} = \frac{3}{2}\left(V_{sd} \cdot I_{sd} + V_{sq} \cdot I_{sq}\right),\ P_{dc} = I_{dc} \cdot V_{dc} \tag{3.3}$$

By combining (3.2) and (3.3), the system can be expressed as:

$$I_{dc} \cdot V_{dc} = \frac{3}{2}\left(V_{sd} \cdot I_{sd} + V_{sq} \cdot I_{sq}\right) + C\frac{dV_{dc}}{dt} \cdot V_{dc} \tag{3.4}$$

where $C\frac{dV_{dc}}{dt}$ is the current flowing through the capacitor and $C\frac{dV_{dc}}{dt} \cdot V_{dc}$ is the input power to the capacitor.

From (3.1) and (3.4), the AC and DC side system of a lossless converter can be expressed as

$$\frac{d}{dt}\begin{bmatrix} I_{sd} \\ I_{sq} \end{bmatrix} = \begin{bmatrix} -R_1/L_1 & \omega_s \\ -\omega_s & -R_1/L_1 \end{bmatrix}\begin{bmatrix} I_{sd} \\ I_{sq} \end{bmatrix} - \frac{1}{L_1}\begin{bmatrix} V_{sd} \\ V_{sq} \end{bmatrix} + \frac{V_{dc}}{2L_1}\begin{bmatrix} M_d \\ M_q \end{bmatrix} \tag{3.5}$$

$$\frac{dV_{dc}}{dt} = \frac{1}{C} \cdot I_{dc} - \frac{3}{4C} \cdot \left(M_d \cdot\ I_{sd} + M_q \cdot I_{sq}\right) \tag{3.6}$$

where $M_d$ and $M_q$ are the converter modulation indices in the d-q reference frame [16, 119] and are given as

$$M_d = 2 \cdot \frac{V_{sd}}{V_{dc}} \tag{3.7}$$

$$M_q = 2 \cdot \frac{V_{sq}}{V_{dc}} \tag{3.8}$$

In the grid connected VSC, $I_{sd}$ and $I_{sq}$ should follow varying reference points, whilst the DC link voltage ($V_{dc}$) should maintain at a constant set value. Taking into account the model represented in (3.5) and (3.6), two separate loops, an inner fast current loop and an outer slow DC voltage loop, are designed to provide the required current and DC voltage control. Interaction between the two loops is avoided by adequately separating their own dynamics [119].

The bandwidth of the inner control loop should be a few times higher than that in the outer control loop, to ensure that the outer control loop appears to be in steady state to the inner control loop and the inner control loop approximates a pure gain for the outer control loop. Thus, the two control loops can be tuned independently. The bandwidth of the inner control loop is limited by the switching frequency of the converter and latency associated with signal sampling and conversion [120].

For designing the current control loop, two auxiliary inputs are defined [119]

$$\begin{bmatrix} u_d \\ u_q \end{bmatrix} = \begin{bmatrix} \frac{dI_{sd}}{dt} \\ \frac{dI_{sq}}{dt} \end{bmatrix} \tag{3.9}$$

Currents $I_{sd}$and $I_{sq}$ can be controlled independently by using the inputs $u_d$ and $u_q$ , respectively. The controller is designed using PI controllers as [119]

$$u_d = \frac{dI_{sd}}{dt} = k_p(I_{sd}^* - I_{sd}) + k_i \int (I_{sd}^* - I_{sd})dt \tag{3.10}$$

$$u_q = \frac{dI_{sq}}{dt} = k_p\left(I_{sq}^* - I_{sq}\right) + k_i \int \left(I_{sq}^* - I_{sq}\right)dt \tag{3.11}$$

where $k_p$ and $k_i$ are the proportional and integral coefficients of the current controller, and the superscript * refers to reference values.

By substituting (3.9) into (3.5), the modulation indices ($M_d$, and $M_q$) are calculated as [119]

$$\begin{cases} M_d = \frac{2L_1}{V_{dc}}\left(u_d + \frac{R_1}{L_1} I_{sd} - \omega_s \cdot I_{sq} + \frac{1}{L_1} u_d\right) \\ M_q = \frac{2L_1}{V_{dc}}\left(u_q + \frac{R_1}{L_1} I_{sq} + \omega_s \cdot I_{sd} + \frac{1}{L_1} u_q\right) \end{cases} \tag{3.12}$$

Fig. 3.3 shows the schematic of the inner current control loop of the grid connected VSC.

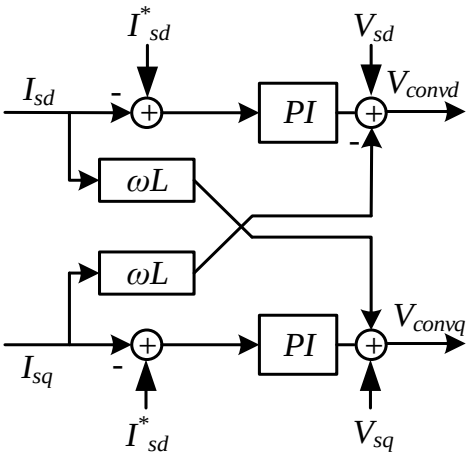


Fig. 3.3. Schematic diagram of VSC current control

### 3.2.1. Outer Control Loop

To provide the reference currents for the inner control loop, different approaches can be used. A simple method is to define power reference $P_{ac}$ and then use (3.3) to calculate reference values for $I_{Sd}$.

It should be noted that it is assumed the grid voltage ($V_s$) is fixed to the d-axis, so the q-axis voltage is zero. Thus (3.3) can be modified as

$$P = \frac{3}{2} V_{sd} \cdot I_{sd} \tag{3.13}$$

where $V_{sd}$ is the d-axis PCC voltage. Reference current for the d-axis can be found by rearranging (3.13) as

$$I^*_{sd} = \frac{\frac{2}{3} P_{ref}}{V_{sd}} \tag{3.14}$$

Also, the reference signal for the q-axis current can be found using the same procedure. The reactive power of the converter can be calculated by [121]

$$Q = \frac{3}{2}(-V_{sd} \cdot I_{sq} + V_{sq} \cdot I_{sd}) \tag{3.15}$$

As $V_{sq} = 0$, (3.15) is simplified to

$$Q = \frac{3}{2}(-V_{sd} \cdot I_{sq}) \tag{3.16}$$

Thus, the q-axis current reference is given as

$$I_{sq}^{*} = -\frac{\frac{2}{3} \cdot Q_{ref}}{V_{sd}} \tag{3.17}$$

This approach is appropriate for the power controller mode of operation for which it is required to control power flow [122].

If a VSC is required to control the DC/AC voltages, separate DC voltage and AC voltage controllers have to be implemented.

A. DC Voltage Controller

From (3.2)-(3.4), there is:

$$\frac{I_{dc}}{C} - \frac{\frac{3}{2} \cdot (V_{sd} \cdot I_{sd} + V_{sq} \cdot I_{sq})}{C V_{dc}} = \frac{dV_{dc}}{dt} \tag{3.18}$$

The DC voltage controller is designed in a similar way to the current controller, and a PI controller can be used as:

$$i_e = \frac{dV_{dc}}{dt} = k_{p_{DC}}(V_{dc}^{*} - V_{dc}) + k_{i_{DC}} \int (V_{dc}^{*} - V_{dc}) dt \tag{3.19}$$

where $k_{p_{DC}}$ and $k_{i_{DC}}$ are the proportional and integral gains of the DC voltage controller, respectively. Then the d-axis current reference, $i_{sd}^{*}$ can be calculated by:

$$I_{sd}^{*} = \frac{4C}{3M_d}\left(-i_e + \frac{1}{C}I_{dc} - \frac{3}{4C}M_q.I_{sq}\right) \tag{3.20}$$

B. AC Voltage Controller

Controlling the AC voltage at the grid connection point is one of the responsibilities of a grid connected VSC, especially when the grid is weak. This is achieved via the provision of reactive power through the control of the q–axis current. Thus, the AC voltage control loop can provide the reference q-axis current for the inner control loop. The reference q-axis current is given as [123]

$$I_{sq}^{*} = k_{p_{AC}}(|V_s^{*}| - |V_s|) + k_{i_{AC}}\int(|V_s^{*}| - |V_s|)dt \tag{3.21}$$

where $k_{p_{AC}}$ and $k_{i_{AC}}$ are proportional and integral gains of the control loop PI regulator, respectively. Proportional and integral gains can be found using the 'trial and error' method, in which the simulation will be run for different values of the gains and the gains will be chosen according to the best time domain performance [122]. Fig. 3.4 (a) shows the control diagram. If the PCC voltage is used as the reference, the d-axis component of the PCC voltage can be used as the control parameter [82]. The other option to control the AC voltage is to use a droop characteristic as shown in Fig. 3.4 (b). The droop controller is essentially a proportional controller.

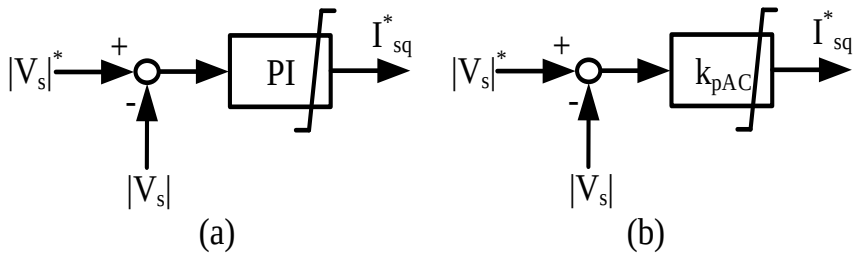


Fig. 3.4. Schematic diagram of AC voltage controller (a) PI controller (b) Droop controller

By using the control structures shown in Fig. 3.4, the reactive power of the VSC will be controlled. The VSC output terminal will act as a PV (power-voltage) bus with the AC voltage being regulated by controlling the reactive power at the VSC terminal [90].

### 3.2.2. Phase Locked Loop

A phase Locked Loop (PLL) detects the position of the grid voltage vector such that the converter output voltage can be synchronised to the grid. The PLL algorithm should cope with voltage sags, harmonics, etc. During power system transient events (e.g. faults), the PLL should also be able to lock to the voltage angle and accurately obtain the phase information. The simplified block diagram of a generic synchronous reference frame PLL (SRF-PLL) is shown in Fig. 3.5.

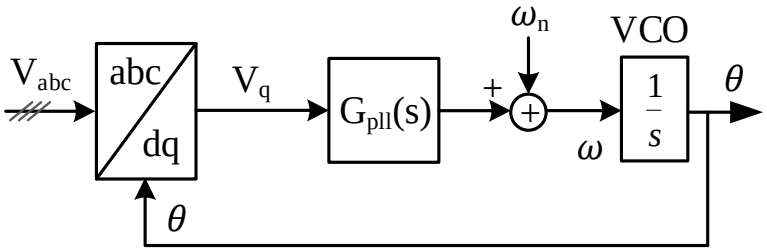


Fig. 3.5. Simplified schematic diagram of an SRF PLL [77]

In the simplified PLL block diagram, $G_{PLL}(s)$ represents a PI regulator, and voltage controlled oscillator (VCO) is simply an integrator.

## 3.3. Modelling of a Grid Connected Single Converter System

### 3.3.1. AC Grid Connection

In this section, the grid connected converter system is modelled by a state-space representation. A simplified system configuration is considered first in which the medium voltage connection cables are ignored. As in wind farms, the amount of inter-array cables that connect turbines together is significant. A state-space model is later developed that includes the inter-array medium voltage cables. The dynamics of the DC side are neglected as the focus is on AC grid stability, and thus, the DC side of the converter is modelled by a stiff DC source.

A. Simplified System Model

The schematic diagram of a grid connected VSC shown in Fig. 3.1 where the VSC is connected to the grid through an AC filter and a transformer, can be further simplified by transferring the voltage to the converter side of the transformer as shown in Fig. 3.6. The VSC is considered as a controllable voltage source, and the power grid is modelled as a voltage source behind an impedance. Furthermore, it is assumed that the three-phase system is balanced and has no neutral line, so there are no negative and zero sequence components.

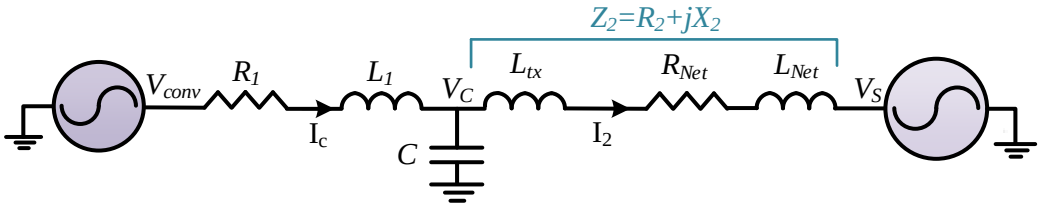


Fig. 3.6. Single line schematic of a VSC connected to the power grid

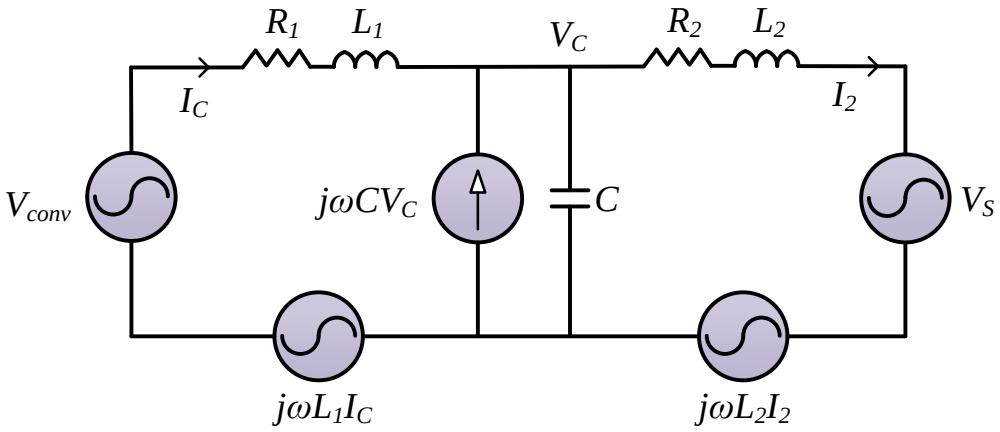


Fig. 3.7. Equivalent circuit of a grid connected VSC in the dq reference frame.

Fig. 3.7 shows the synchronous reference frame equivalent of the grid connected converter shown in Fig. 3.6. Using circuit theory, the circuit equations are obtained as

$$\begin{cases} \frac{L_1 d\boldsymbol{I_C}}{dt} + \boldsymbol{V_C} + j\omega L_1 \boldsymbol{I_C} - \boldsymbol{V_{conv}} + R_1 \boldsymbol{I_C} = 0 \\ L_2 \frac{d\boldsymbol{I_2}}{dt} + R_2 \boldsymbol{I_2} + \boldsymbol{V_s} + j\omega L_2 \boldsymbol{I_2} - \boldsymbol{V_C} = 0 \\ \boldsymbol{I_C} + j\omega C \boldsymbol{V_C} - \boldsymbol{I_2} - C \frac{d\boldsymbol{V_c}}{dt} = 0 \end{cases} \tag{3.22}$$

Transferring all the parameters and variables to per unit values using VSC rated power and terminal voltage as the based power and voltage values, respectively, the per unit state-space representative of system in the synchronous reference frame can be obtained by rearranging (3.22) as

$$\begin{cases} \dot{x}(t) = \boldsymbol{A}x(t) + \boldsymbol{B}u(t) \\ Y = \boldsymbol{C}x(t) + \boldsymbol{D}u(t) \end{cases} \tag{3.23}$$

where

$$\dot{x} = \frac{d}{dt}\left[I_{\mathrm{C}d}\, I_{\mathrm{C}q} V_{Cd}\, V_{Cq}\, I_{2d}\, I_{2q}\right]^T;\ x = \left[I_{\mathrm{C}d}\, I_{\mathrm{C}q} V_{Cd}\, V_{Cq}\, I_{2d}\, I_{2q}\right]^T;$$

$$u = \left[V_{sd}\, V_{sq}\, V_{convd}\, V_{convq}\right]^T$$

$$\boldsymbol{A} = \omega_b \begin{bmatrix} -\frac{R_1}{L_1} & \omega & -\frac{1}{L_1} & 0 & 0 & 0 \\ -\omega & -\frac{R_1}{L_1} & 0 & -\frac{1}{L_1} & 0 & 0 \\ \frac{1}{C} & 0 & 0 & -\omega & -\frac{1}{C} & 0 \\ 0 & \frac{1}{C} & \omega & 0 & 0 & -\frac{1}{C} \\ 0 & 0 & \frac{1}{L_2} & 0 & -\frac{R_2}{L_2} & \omega \\ 0 & 0 & 0 & \frac{1}{L_2} & -\omega & -\frac{R_2}{L_2} \end{bmatrix}$$

$$\boldsymbol{B} = \omega_b \begin{bmatrix} 0 & 0 & 0 & 0 & -\frac{1}{L_2} & 0 \\ 0 & 0 & 0 & 0 & 0 & -\frac{1}{L_2} \\ \frac{1}{L_1} & 0 & 0 & 0 & 0 & 0 \\ 0 & \frac{1}{L_1} & 0 & 0 & 0 & 0 \end{bmatrix}^T$$

where $\omega$ and $\omega_b$ are the per unit and base angular frequency of the system, respectively.

In the aforementioned model, $L_2$ and $R_2$ represent the respective combined equivalent inductance and resistance of the AC grid and the transformer, i.e. $L_2 = L_{Net} + L_{tx}$, $R_2 = R_{Net} + R_{tx}$. The per unit grid impedance for a specific SCR is obtained using (2.2) and (2.3).

The cables can also be modelled by 'T' and 'Pi' equivalent representations. In the next section, the intra-array cables will be modelled by using T and Pi models to assess whether or not the simplified model is comparable with them.

B. System Model with Inter-Array Cables (T model)

In wind farms, wind turbines are usually connected through subsea/underground medium voltage cables. As the size of the wind farm increases, the amount of inter-array cables also increases. Therefore, medium voltage cables need to be considered in the system model.

Fig. 3.8 shows the schematic diagram of a wind turbine converter connected to the grid and where the medium voltage cables are considered by one T section equivalent of the cables.

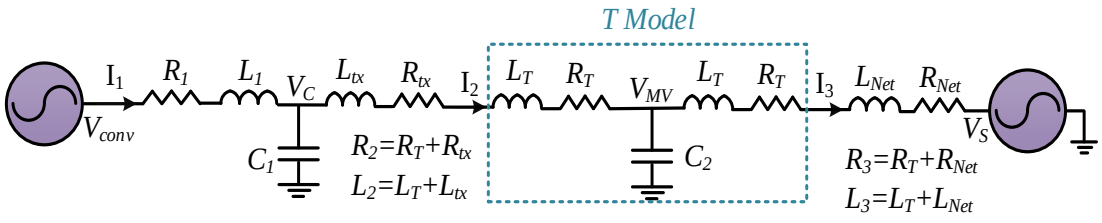


Fig. 3.8. Single line schematic of a VSC connected to the power grid with T equivalent cable representation

Using the same procedure as in section 3.3.1.A, the state-space model of the AC connection of a wind turbine to grid shown in Fig. 3.8, in the synchronous reference frame, is represented by

$$\begin{cases} \dot{x}(t) = \boldsymbol{A_1} x(t) + \boldsymbol{B_1} u(t) \\ Y = \boldsymbol{C_1} x(t) + \boldsymbol{D_1} u(t) \end{cases} \tag{3.24}$$

where

$$\dot{x} = \frac{d}{dt}\left[I_{1_d}\, I_{1_q} V_{C_d}\, V_{C_q}\, I_{2_d}\, I_{2_q}\, V_{MV_d}\, V_{MV_q}\, I_{3_d}\, I_{3_q}\right]^T$$

$$x = \left[I_{1_d}\, I_{1_q} V_{C_d}\, V_{C_q}\, I_{2_d}\, I_{2_q}\, V_{MV_d}\, V_{MV_q}\, I_{3_d}\, I_{3_q}\right]^T;\ u = \left[V_{s_d}\, V_{s_q}\, V_{conv_d}\, V_{conv_q}\right]^T$$

$$\boldsymbol{A_1} = \omega_b \begin{bmatrix} -\frac{R_1}{L_1} & \omega & -\frac{1}{L_1} & 0 & 0 & 0 & 0 & 0 & 0 & 0 \\ -\omega & -\frac{R_1}{L_1} & 0 & -\frac{1}{L_1} & 0 & 0 & 0 & 0 & 0 & 0 \\ \frac{1}{C_1} & 0 & 0 & -\omega & -\frac{1}{C_1} & 0 & 0 & 0 & 0 & 0 \\ 0 & \frac{1}{C_1} & \omega & 0 & 0 & -\frac{1}{C_1} & 0 & 0 & 0 & 0 \\ 0 & 0 & \frac{1}{L_2} & 0 & -\frac{R_2}{L_2} & \omega & -\frac{1}{L_2} & 0 & 0 & 0 \\ 0 & 0 & 0 & \frac{1}{L_2} & -\omega & -\frac{R_2}{L_2} & 0 & -\frac{1}{L_2} & 0 & 0 \\ 0 & 0 & 0 & 0 & \frac{1}{C_2} & 0 & 0 & -\omega & -\frac{1}{C_2} & 0 \\ 0 & 0 & 0 & 0 & 0 & \frac{1}{C_2} & \omega & 0 & 0 & -\frac{1}{C_2} \\ 0 & 0 & 0 & 0 & 0 & 0 & \frac{1}{L_2} & 0 & -\frac{R_3}{L_3} & \omega \\ 0 & 0 & 0 & 0 & 0 & 0 & 0 & \frac{1}{L_2} & -\omega & -\frac{R_3}{L_3} \end{bmatrix}$$

$$\boldsymbol{B_1} = \omega_b \begin{bmatrix} 0 & 0 & 0 & 0 & 0 & 0 & 0 & 0 & -\frac{1}{L_3} & 0 \\ 0 & 0 & 0 & 0 & 0 & 0 & 0 & 0 & 0 & -\frac{1}{L_3} \\ \frac{1}{L_1} & 0 & 0 & 0 & 0 & 0 & 0 & 0 & 0 & 0 \\ 0 & \frac{1}{L_1} & 0 & 0 & 0 & 0 & 0 & 0 & 0 & 0 \end{bmatrix}^T$$

C. System Model With Pi Equivalent Representation of Inter-Array Cables

The other possible option of modelling the system AC connection is to consider the Pi equivalent of the inter-array cables as shown in Fig. 3.9, where $C_2$, $C_3$, $R_3$, and $L_3$ are the parameters for the Pi section equivalent of the inter-array cables. $L_2$, $R_2$, $L_4$, and $R_4$ are the inductances and resistances of the transformer and grid, respectively.

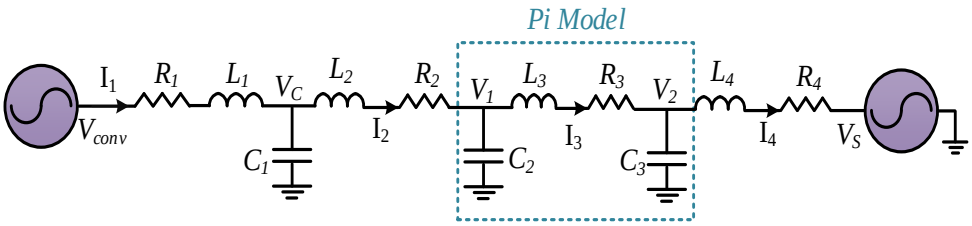


Fig. 3.9. Single line schematic of a VSC connected to the power grid with Pi equivalent representation of cables

The per unit state-space representation of the system in the synchronous reference frame shown in Fig. 3.9 is

$$\begin{cases} \dot{x}(t) = \boldsymbol{A_2}x(t) + \boldsymbol{B_2}u(t) \\ Y = \boldsymbol{C_2}x(t) + \boldsymbol{D_2}u(t) \end{cases} \tag{3.25}$$

where

$$\dot{x} = \frac{d}{dt}\left[I_{1_d}\, I_{1_q} V_{C_d}\, V_{C_q}\, I_{2_d}\, I_{2_q}\, V_{MV_d}\, V_{MV_q}\, I_{3_d}\, I_{3_q}\right]^T$$

$$x = \left[I_{1_d}\, I_{1_q} V_{C_d}\, V_{C_q}\, I_{2_d}\, I_{2_q}\, V_{MV_d}\, V_{MV_q}\, I_{3_d}\, I_{3_q}\right]^T ; u = \left[V_{s_d}\, V_{s_q}\, V_{conv_d}\, V_{conv_q}\right]^T$$

$$\boldsymbol{A_2} = \omega_b \begin{bmatrix}
-\frac{R_1}{L_1} & \omega & -\frac{1}{L_1} & 0 & 0 & 0 & 0 & 0 & 0 & 0 & 0 & 0 & 0 & 0 \\
-\omega & -\frac{R_1}{L_1} & 0 & -\frac{1}{L_1} & 0 & 0 & 0 & 0 & 0 & 0 & 0 & 0 & 0 & 0 \\
\frac{1}{C_1} & 0 & 0 & -\omega & -\frac{1}{C_1} & 0 & 0 & 0 & 0 & 0 & 0 & 0 & 0 & 0 \\
0 & \frac{1}{C_1} & \omega & 0 & 0 & -\frac{1}{C_1} & 0 & 0 & 0 & 0 & 0 & 0 & 0 & 0 \\
0 & 0 & \frac{1}{L_2} & 0 & -\frac{R_2}{L_2} & \omega & -\frac{1}{L_2} & 0 & 0 & 0 & 0 & 0 & 0 & 0 \\
0 & 0 & 0 & \frac{1}{L_2} & -\omega & -\frac{R_2}{L_2} & 0 & -\frac{1}{L_2} & 0 & 0 & 0 & 0 & 0 & 0 \\
0 & 0 & 0 & 0 & \frac{1}{C_2} & 0 & 0 & -\omega & -\frac{1}{C_2} & 0 & 0 & 0 & 0 & 0 \\
0 & 0 & 0 & 0 & 0 & \frac{1}{C_2} & \omega & 0 & 0 & -\frac{1}{C_2} & 0 & 0 & 0 & 0 \\
0 & 0 & 0 & 0 & 0 & 0 & \frac{1}{L_3} & 0 & -\frac{R_3}{L_3} & \omega & -\frac{1}{L_3} & 0 & 0 & 0 \\
0 & 0 & 0 & 0 & 0 & 0 & 0 & \frac{1}{L_3} & -\omega & -\frac{R_3}{L_3} & 0 & -\frac{1}{L_3} & 0 & 0 \\
0 & 0 & 0 & 0 & 0 & 0 & 0 & 0 & \frac{1}{C_3} & 0 & 0 & -\omega & -\frac{1}{C_3} & 0 \\
0 & 0 & 0 & 0 & 0 & 0 & 0 & 0 & 0 & \frac{1}{C_3} & \omega & 0 & 0 & -\frac{1}{C_3} \\
0 & 0 & 0 & 0 & 0 & 0 & 0 & 0 & 0 & 0 & \frac{1}{L_4} & 0 & -\frac{R_4}{L_4} & \omega \\
0 & 0 & 0 & 0 & 0 & 0 & 0 & 0 & 0 & 0 & 0 & \frac{1}{L_4} & -\omega & -\frac{R_4}{L_4}
\end{bmatrix}$$

$$\boldsymbol{B_2} = \omega_b \begin{bmatrix} 0 & 0 & 0 & 0 & 0 & 0 & 0 & 0 & 0 & 0 & 0 & 0 & -\frac{1}{L_4} & 0 \\ 0 & 0 & 0 & 0 & 0 & 0 & 0 & 0 & 0 & 0 & 0 & 0 & 0 & -\frac{1}{L_4} \\ \frac{1}{L_1} & 0 & 0 & 0 & 0 & 0 & 0 & 0 & 0 & 0 & 0 & 0 & 0 & 0 \\ 0 & \frac{1}{L_1} & 0 & 0 & 0 & 0 & 0 & 0 & 0 & 0 & 0 & 0 & 0 & 0 \end{bmatrix}^T$$

### 3.3.2. PWM Modulator Modelling

The PWM modulator dynamics are much faster than those of the current controller, but the modulator still imposes a delay to the system that is dependent on the sampling technique and switching frequency. In this analysis, the PWM modulator is considered as a unit delay ($e^{-TS}$) where the delay time constant T is half a PWM cycle. Using the Taylor's expansion of the unit delay around the operating point and considering the first order term, the final transfer function of the switching delay is approximated as

$$PWM_{TF} = \frac{1}{\tau_a s+1} \tag{3.26}$$

where $\tau_a$ is the modulation delay (i.e. $\tau_a = \frac{T_{switching}}{2}$).

Therefore, the relationship between the desirable converter voltage $\boldsymbol{V'_{conv}}$ from the current controller and the actual output voltage of the converter $\boldsymbol{V_{conv}}$ is represented as

$$\boldsymbol{V_{conv}} = \frac{1}{\tau_a s+1} \boldsymbol{V'_{conv}} \tag{3.27}$$

### 3.3.3. Converter Controller Modelling

The VSC control law in synchronous reference frame is presented as

$$\boldsymbol{V_{conv}} = L_1 \boldsymbol{U_C} + \boldsymbol{V_c} - j\omega L_1 \boldsymbol{I_C} \tag{3.28}$$

where

$$\boldsymbol{U_C} = k_p(\boldsymbol{I_C^*} - \boldsymbol{I_C}) + k_i \int (\boldsymbol{I_C^*} - \boldsymbol{I_C}) dt \tag{3.29}$$

The proportional-integral regulator used in current control is represented as

$$G_{PI} = k_p + \frac{k_i}{s} \tag{3.30}$$

where $k_p$ and $k_i$ are the proportional and integral gains, respectively. The proportional and integral gains of the regulator are found by second order approximation of a system as

$$k_p = 2\omega_n\zeta \tag{3.31}$$

$$k_i = \omega_n^2 \tag{3.32}$$

where $\omega_n$ is the current loop natural frequency and $\zeta$ represents the damping coefficient of the system [120].

### 3.3.4. Overall System Modelling

By combining different parts of the system, Fig. 3.10 shows the simplified schematic block diagram of the frequency domain model of the complete converter system. The overall multiple-input-multiple-output frequency domain model of the grid connected converter in the dq reference frame is developed as shown in Fig. 3.11.

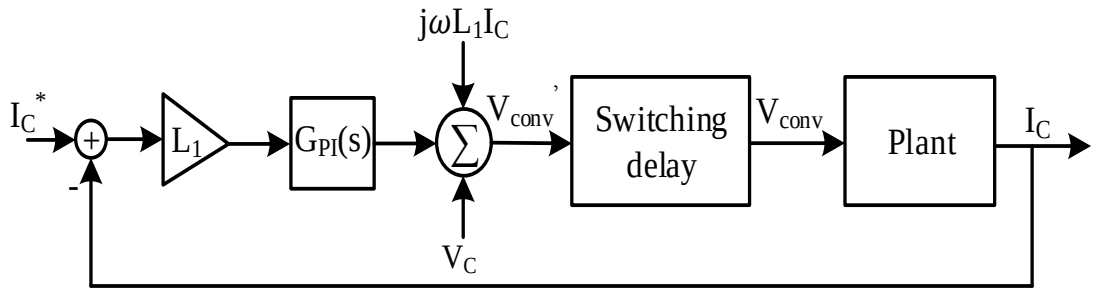


Fig. 3.10. Block diagram of the frequency domain model of the converter

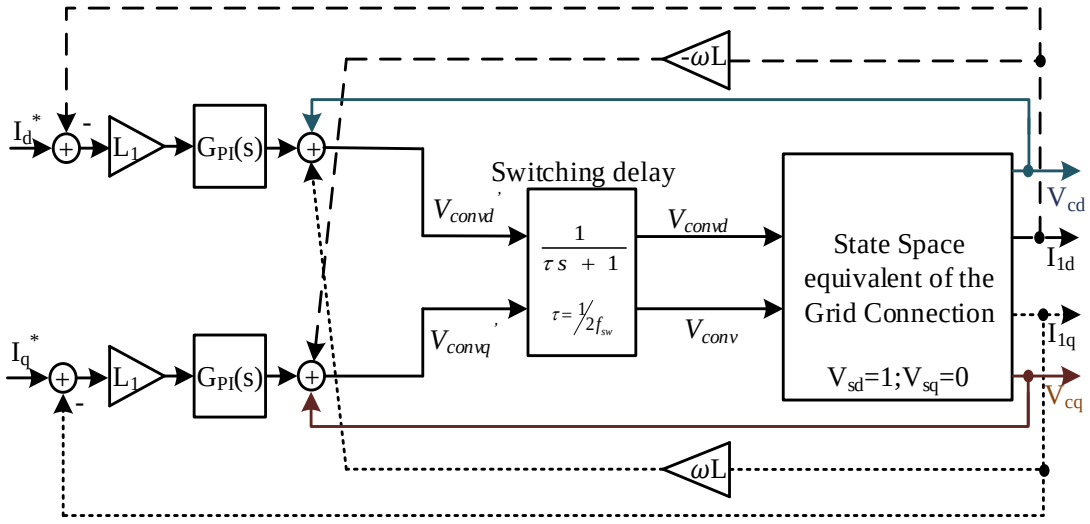


Fig. 3.11. Schematic block diagram of the MIMO model of the grid connected VSC

## 3.4. Phase locked Loop Modelling

As mentioned in Section 2.3.3, the PLL is used to capture the phase angle of the filter bus voltage, which is used to transfer current and voltage to the dq frame (i.e. SRF) for the controller and to transfer the output of the converter control from dq frame to the abc frame for PWM modulation. Therefore, to have the true and accurate model of the overall system for stability studies, the PLL needs to be integrated into the model developed in Section 3.3.4.

Under ideal operating conditions, the angle measured by the PLL ( $\theta_{PLL}$ in Fig. 3.12) is identical to the actual phase angle of $V_C$ ( $\theta_C$ in Fig. 3.12), and the phase error $\Delta\theta$ between the angle of the filter bus voltage and the PLL measurement is zero as shown in Fig. 3.12 (a) [124]. If a disturbance occurs (e.g. a change in the current / power, a fault, etc.), the filter bus voltage $V_C$ will change accordingly resulting in misalignment between the phase angle measured by the PLL and actual phase angle of $V_C$, leading to a substantial phase angle error of $\Delta\theta$ between $\theta_C$ and $\theta_{PLL}$ (Fig. 3.12(b)) [124]. As the real control system only sees $\theta_{PLL}$, to include the full dynamics of the PLL in the control system requires that the converter output voltage in the model is phase shifted by $\Delta\theta$.

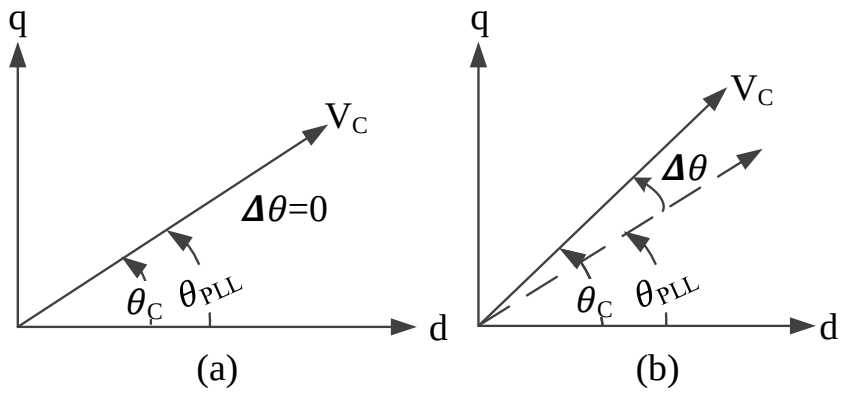


Fig. 3.12. Positions of the actual and PLL measured filter bus (PCC) voltage

A method of modelling the impacts of PLL and AC side voltage on the dynamic model of LCC converters has been presented in [125]. In this method, the phase angle of the AC side voltage is used to calculate the phase difference between the actual voltage and the PLL output, and then the calculated phase difference is added to the firing angles. A similar concept has been adopted for modelling the impact of the PLL on the dynamics of the VSC where the phase difference was used to rotate the converter output voltage (i.e. $\boldsymbol{V_{conv}}$ ).

In the state-space model shown in (3.21), $V_{Cd}$and $V_{Cq}$ are considered as the states and are also used as the feed-forward term. As previously described, to include the impact of the PLL on system dynamics, the phase error between the PLL measurement and the actual filter bus voltage is used to rotate the converter output terminal voltage vector as schematically shown in Fig. 3.13. As shown, the phase angle rotation is shown as $e^{j\Delta\theta}$ and a new vector for converter terminal voltage is then obtained ($\boldsymbol{V'_{conv}}$).

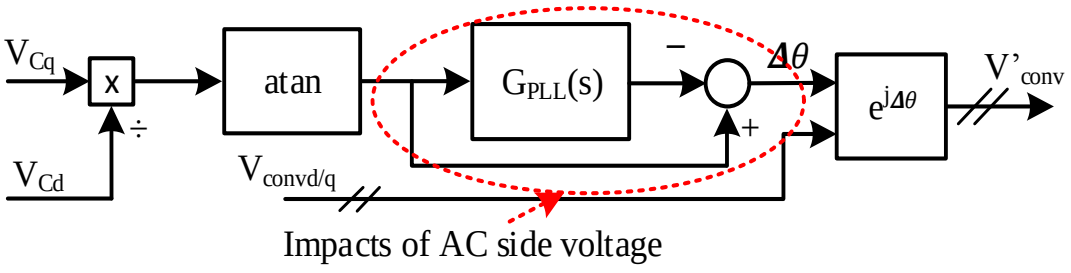


Fig. 3.13. Simplified schematic of rotation due to the PLL.

Considering the angle error is usually small, rotation of the converter voltage can be simplified as

$$e^{j\Delta\theta} = \begin{bmatrix} cos\Delta\theta & -sin\Delta\theta \\ sin\Delta\theta & cos\Delta\theta \end{bmatrix} = \begin{bmatrix} 1 & -\Delta\theta \\ \Delta\theta & 1 \end{bmatrix} \tag{3.33}$$

The PLL function is represented by $G_{pll}(s)$ as the closed-loop transfer function, which can be expressed as

$$G_{PLL}(s) = \frac{k_{p_{PLL}}s + k_{i_{PLL}}}{s^2 + k_{p_{PLL}}s + k_{i_{PLL}}} \tag{3.34}$$

where $k_{p_{PLL}}$ and $k_{i_{PLL}}$ are the proportional and integral gains respectively. Using Taylor's Expansion, the process of $arctan(V_{C_d}/V_{C_q})$ in Fig. 3.13 can be linearized as

$$arctan\frac{V_{C_q}}{V_{C_d}} \approx \frac{V_{C_{q_0}}}{V_{C_{d_0}}} + \frac{d}{d\left(\frac{V_{C_q}}{V_{C_d}}\right)}\left(arctan\frac{V_{C_q}}{V_{C_d}}\right)\Bigg|_{\frac{V_{C_q}}{V_{C_d}} = \frac{V_{C_{q_0}}}{V_{C_{d_0}}}} \left(\frac{V_{C_q}}{V_{C_d}} - \frac{V_{C_{q_0}}}{V_{C_{d_0}}}\right)$$

$$= \frac{V_{C_{q_0}}}{V_{C_{d_0}}} + \frac{1}{1+\frac{V_{C_{q_0}}^2}{V_{C_{d_0}}^2}}\left(\frac{\boldsymbol{V_{C_q}}}{\boldsymbol{V_{C_d}}} - \frac{V_{C_{q_0}}}{V_{C_{d_0}}}\right) \tag{3.35}$$

where $V_{C_{q_0}}$ and $V_{C_{d_0}}$ are the operating point of the filter bus voltage. The final block diagram of the grid connected VSC with integrated PLL dynamics is shown in Fig. 3.14.

## 3.5. Model Validation and Case Studies for Developed MIMO Models

Table 3.1 shows the parameters of the VSC and AC grid that are used in this section for validating the developed models. The converter is considered as a lumped model of 10 wind turbines each rated at 6 MW in a wind farm giving a total rated power of 60 MW. The state-space model performance is compared with that of an equivalent time domain model developed in Matlab/Simulink. The time domain model is

developed using the system layout shown in Fig. 3.6. In the developed time domain model, an average model of the VSC with a first order delay to model the switching delays is used. All the parameters for the time domain model are also as shown in Table 3.1.

### 3.5.1. Simplified Grid Connection

For the simplified circuit shown in Fig. 3.6, the time domain and state-space step responses of the d- and q- axis currents for two different operating points are shown in Fig. 3.15 with SCR=5. As seen in Fig. 3.15 (a) and 3.15 (b), a small step of 0.1 p.u. is used and the step responses for the time domain and frequency domain match well (their rise time, peak time, settling time, etc. are all very close). Furthermore, in Fig. 3.15 (c) and 3.15 (d), a step of 0.05 p.u. is applied to both time domain and frequency domain models when the converter was initially operating 0.7 p.u. power. As seen in Fig. 3.15 (c) and 3.15 (d), the d- and q- axis step responses for the time domain and frequency domain also match well. As seen in Fig. 3.15, there is a small misalignment between the time domain simulation results and those from the state space model. This is due to a switch used in time domain simulations whose internal impedance is not modelled in the state space representation. This means that the frequency domain model is a good representation of the actual system and can be used for further studies. The root loci of the d-axis current of the system for variation of the SCR value of the model shown in Fig. 3.6 is shown in Fig. 3.16 . The direction of arrows indicates the movement of poles when the SCR value decreases from 100 to 1 and the converter exports 1 p.u. active power. The poles of the system move to the unstable region with SCR values less than 1.6.

Table 3.1. Parameters for the VSC connected to the grid

| Parameter | Value |
|---|---|
| Rated power | 60 MW |
| Rated AC voltage | 690 V |
| $L_1$ and $R_1$ | 0.2 p.u. and 0.01 p.u |
| $L_{tx}$, $L_{tx\ net}$, and C | 0.1 p.u. |
| $f_b$ | 50 Hz |
| Short Circuit Ratio (SCR) and XRr | 5 and 4 |
| Cable length | 10 km |
| Cable capacitance, inductance and resistance | 0.38 μF/km, 0.31 mH/km, and 0.012 Ω/km |

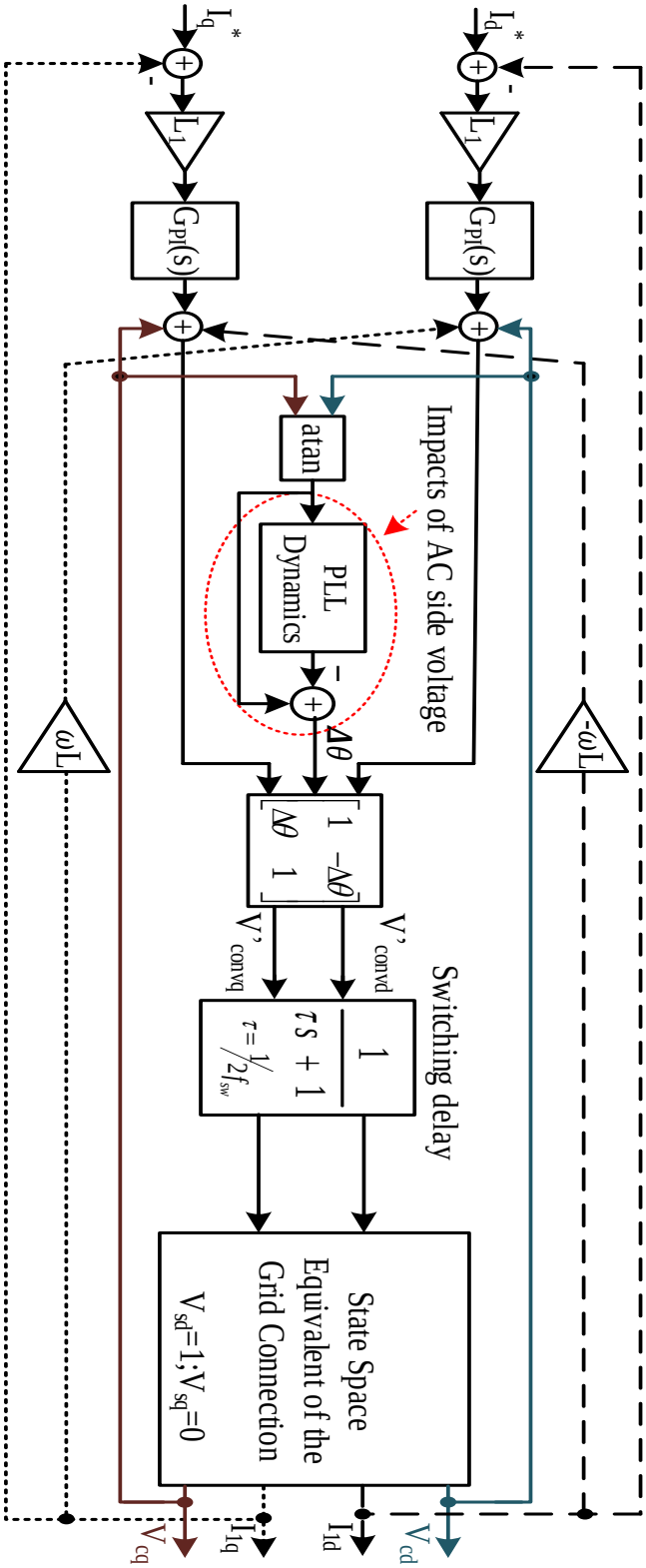


Fig. 3.14. Schematic block diagram of the MIMO model of the grid connected VSC with integrated PLL.

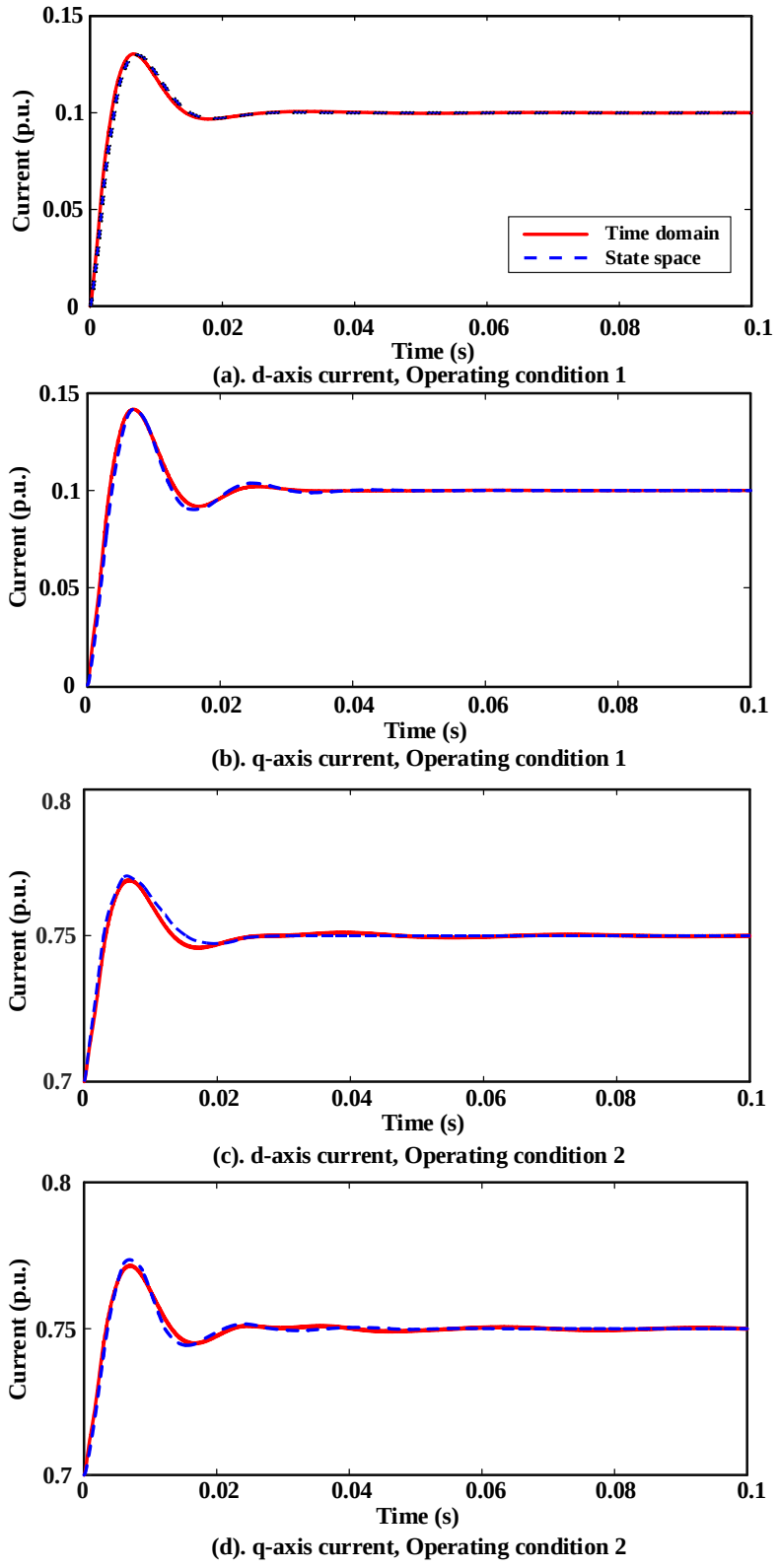


Fig. 3.15. Step responses of the d- and q- axis currents for a small current step, operating condition 1: a step of 0.1 p.u. is applied to zero current; operating condition 2: a step of 0.05 is applied when converter is operating with 0.7 p.u. current.

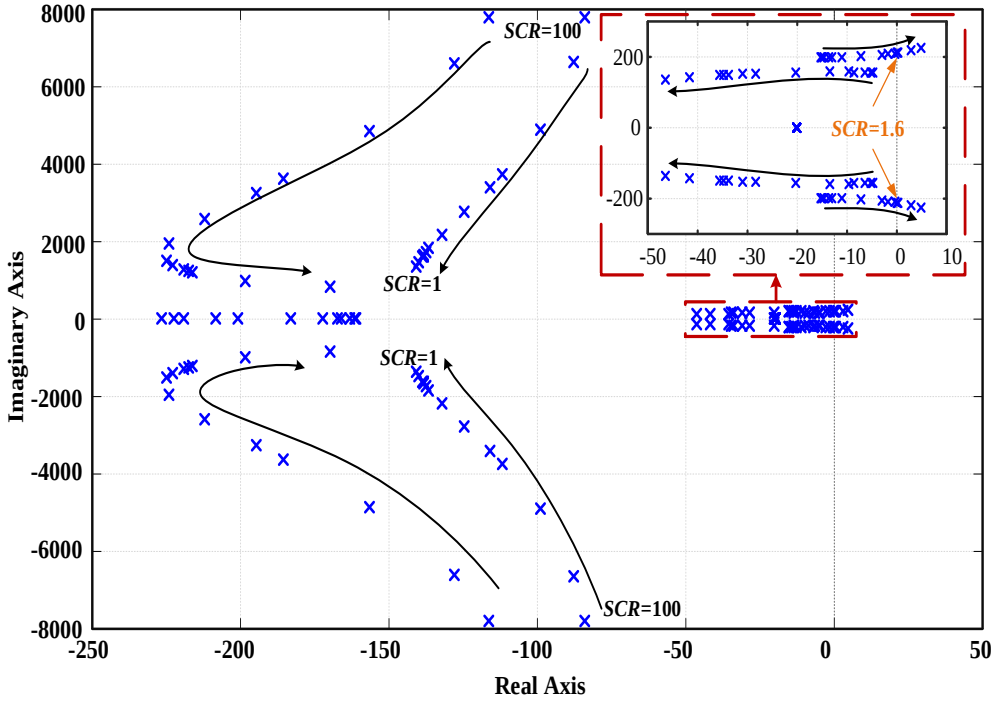


Fig. 3.16. Root loci of the d-axis current for different SCR levels

### 3.5.2. System Model with Inter-Array Cables (T model)

If the grid connection of the wind turbine involves a significant amount of inter-array cables, by using the AC grid connection model in (3.21), some of the system dynamics are ignored as the capacitance of the inter-array cables is not modelled. Therefore, to improve the frequency domain model, the inter-array cables are modelled using the T equivalent of the cables as (3.25).

Fig. 3.17 shows the step responses of the d-axis current for a 60 MW converter connected to a grid with SCR=5 and the cable length of 10 km. As seen in Fig. 3.17, the step response for the T equivalent model of the cables is quite similar to the step responses of the other two.

The open loop Bode diagrams for the simplified state-space model and state-space model with T equivalent of the cables and a cable length of 50 km are shown in Fig. 3.18. This Bode diagram indicates that for low frequencies ($<10^3$ rad/s) and very high frequencies ($> 10^4$ rad/s) both systems have the almost identical behaviour, but

for the middle range frequencies, the model incorporating the T equivalent of cables has an extra resonant peak at around approximately 5000 rad/s. This additional resonance peak is due to the inclusion of the cable capacitance in the model. This resonance is the result of inclusion of the cable model in the simulation, and the resonant frequency corresponds with that predicted by the cable parameters shown in Table 3.1.

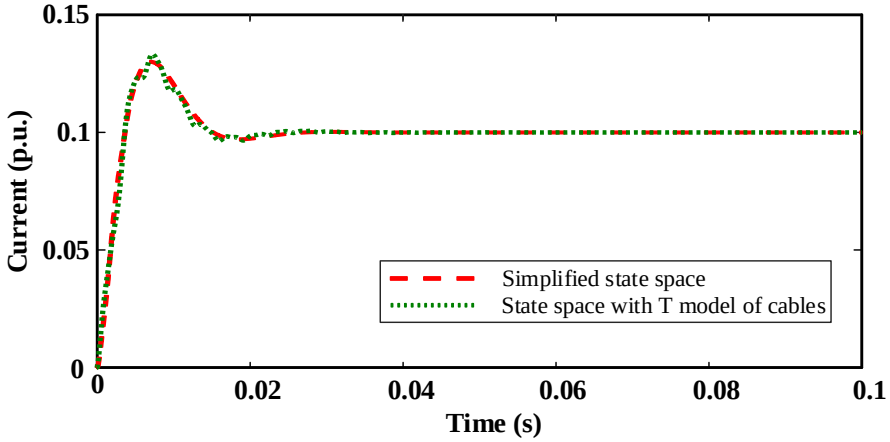


Fig. 3.17. Step responses of the d-axis current for T equivalent of the medium voltage cables

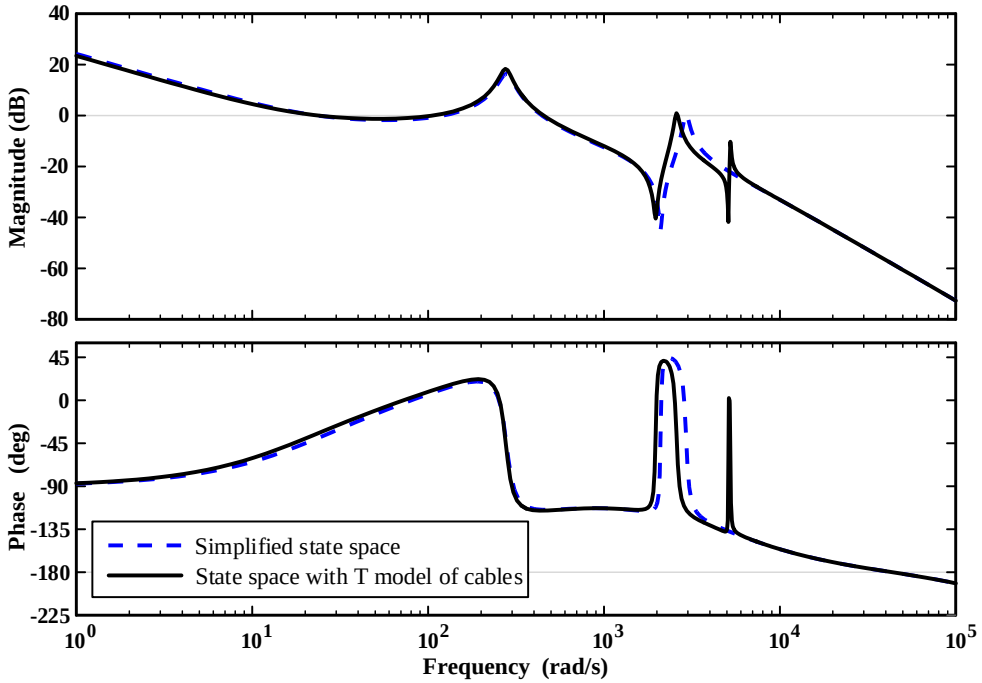


Fig. 3.18. Open loop Bode diagram of the simplified state-space model and T equivalent of cables

### 3.5.3. System Model with Inter-Array Cables (Pi model)

Further tests using the state-space model with the cables modelled using the Pi equivalent of the system as shown in (3.26) are carried out. Considering only one Pi section, the step responses of the d-axis current for different models are compared in Fig. 3.19. As seen in Fig. 3.19, the step responses from the different models are similar.

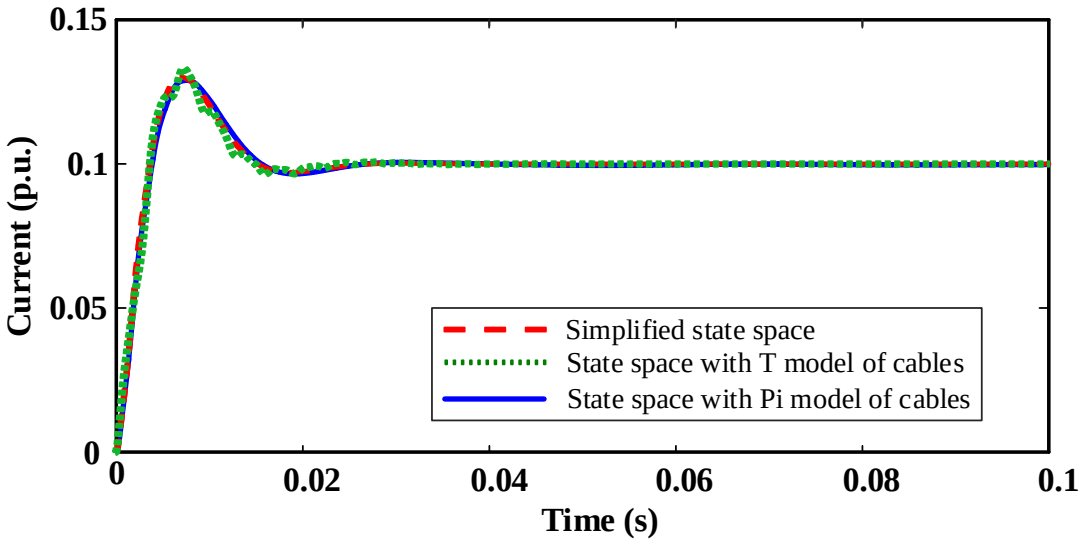


Fig. 3.19. Step response of the system for various AC grid connections

The Bode plot of the system for different types of the grid connection models and cable lengths of 20 km is shown in Fig. 3.20. The three systems shown in this section (i.e. different connection networks) are different representations of the same system with a different level of complexity. The three systems have very similar time responses. As the presented Bode diagram depict, these three AC connections have relatively similar frequency domain behaviour at low frequency. In this thesis, as the frequency of interest is relatively low in range of below 300 Hz. Therefore, the simplified state-space AC connection model is used, which needs less computational power than other models.

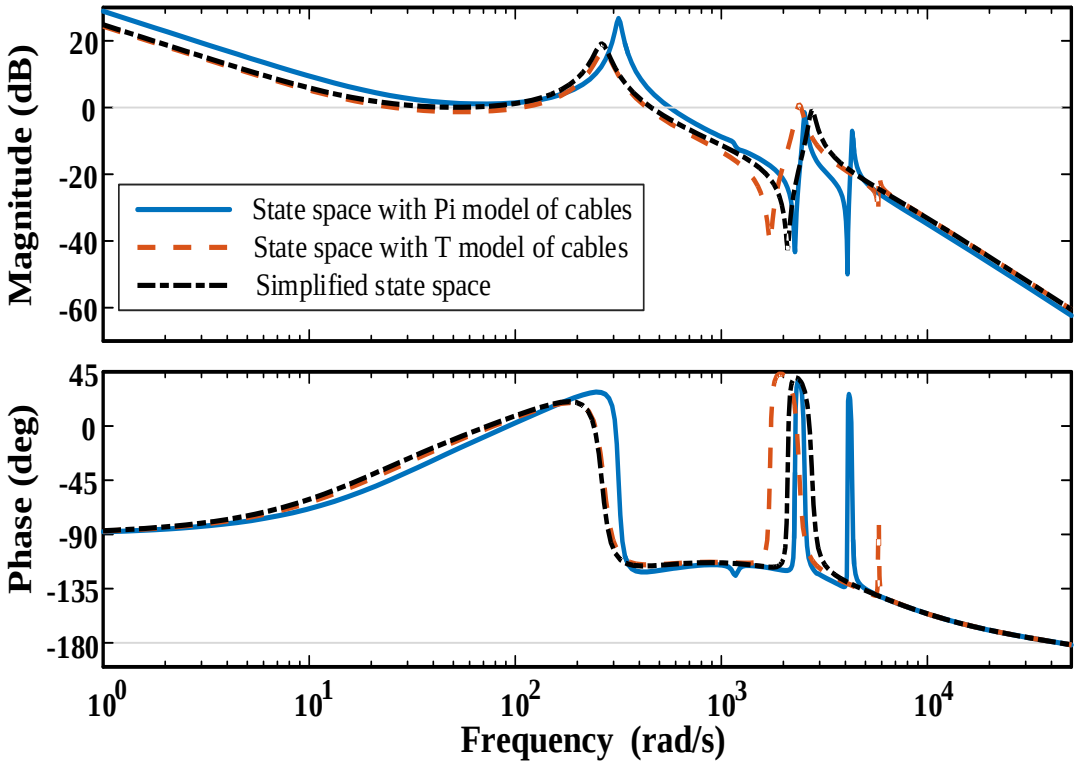


Fig. 3.20. Open loop Bode diagram of the system for various AC connections and cable length =20 km, SCR=5.

## 3.6. Modelling of Parallel Converters

In this section, the dynamic model of parallel VSCs is developed. Fig. 3.21 shows the single line circuit of two parallel converters connected to the main grid through a step-up transformer (modelled by the inductance $L_{tx_{net}}$) and transmission lines. Each converter is represented by the model developed in Section 3.4.4. In the time domain model, the outputs of the two clusters are current sources which are then connected to the step up transformer $L_{tx_{net}}$ (also modelled as a current source in the simulation) in the model. A problem arises due to series connection of current sources and thus a very small capacitor ( $C_{net} = 0.0001\ p.u.$) is added to the model as shown in Fig. 3.21 to solve the simulation issue without affecting the results.

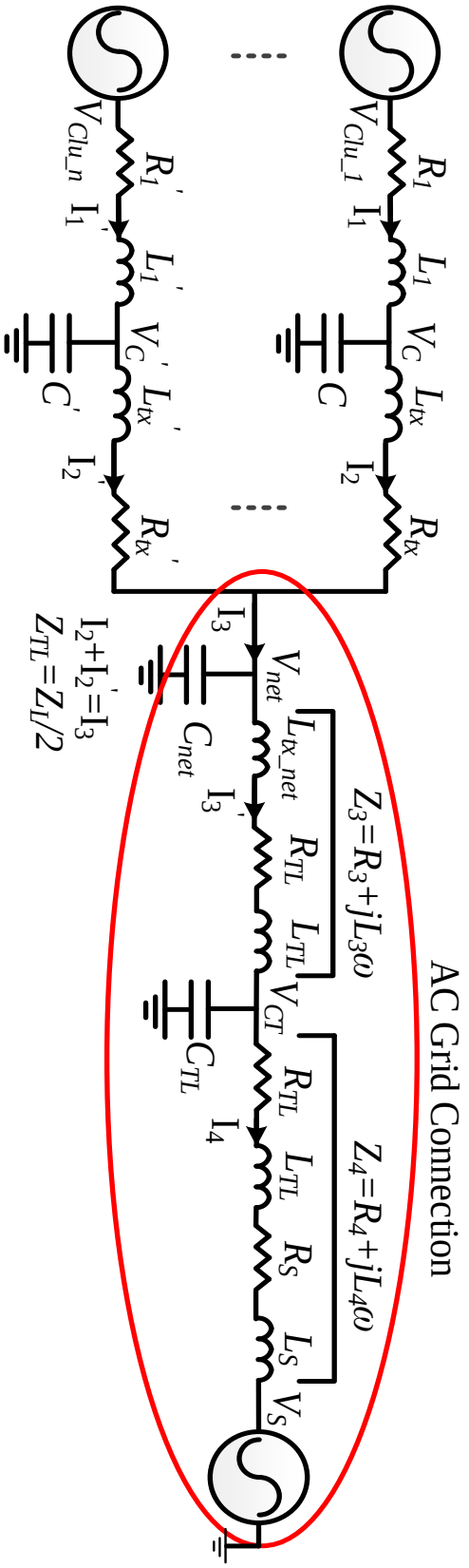


Fig. 3.21. Single line circuit diagram of two parallel converters with T line model.

The transmission line is modelled as a simple T section as shown in Fig. 3.21. The Pi equivalent representation of a transmission line could also be used, but with a T section model, the order of the state-space system is reduced by 4 (80 fewer elements in the state matrix) which reduces the complexity of the model as well as the computation requirements. The state-space representation of the AC grid connection in the SRF consists of 8 states as shown in

$$\begin{cases} \dot{x}(t) = \boldsymbol{A_3} x(t) + \boldsymbol{B_3} u(t) \\ Y = \boldsymbol{C_3} x(t) + \boldsymbol{D_3} u(t) \end{cases} \tag{3.36}$$

where

$$u = \left[ I_{3_d} \; I_{3_q} \; V_{S_d} \; V_{S_q} \right]^T ; x = \left[ I_{3_d}' \; I_{3_q}' \; V_{net_d} \; V_{net_q} \; I_{4_d} \; I_{4_q} \; V_{CT_d} \; V_{CT_q} \right]^T$$

$$\dot{x} = \frac{d}{dt} \left[ I_{3_d}^{'} \; I_{3_q}^{'} \; V_{net_d} \; V_{net_q} \; I_{4_d} \; I_{4_q} \; V_{CT_d} \; V_{CT_q} \right]^T$$

$$\boldsymbol{A_3} = \omega_b \begin{bmatrix} -\frac{r_3}{L_3} & w & \frac{1}{L_3} & 0 & 0 & 0 & -\frac{1}{L_3} & 0 \\ -w & -\frac{r_3}{L_3} & 0 & \frac{1}{L_3} & 0 & 0 & 0 & -\frac{1}{L_3} \\ -\frac{1}{C_{net}} & 0 & 0 & -w & 0 & 0 & 0 & 0 \\ 0 & -\frac{1}{C_{net}} & w & 0 & 0 & 0 & 0 & 0 \\ 0 & 0 & 0 & 0 & -\frac{r_4}{L_4} & w & \frac{1}{L_4} & 0 \\ 0 & 0 & 0 & 0 & -w & -\frac{r_4}{L_4} & 0 & \frac{1}{L_4} \\ \frac{1}{C_{TL}} & 0 & 0 & 0 & -\frac{1}{C_{TL}} & 0 & 0 & -w \\ 0 & \frac{1}{C_{TL}} & 0 & 0 & 0 & -\frac{1}{C_{TL}} & w & 0 \end{bmatrix}$$

$$\boldsymbol{B_3} = \omega_b \begin{bmatrix} 0 & 0 & \frac{1}{C_{net}} & 0 & 0 & 0 & 0 & 0 \\ 0 & 0 & 0 & \frac{1}{C_{net}} & 0 & 0 & 0 & 0 \\ 0 & 0 & 0 & 0 & \frac{1}{L_4} & 0 & 0 & 0 \\ 0 & 0 & 0 & 0 & 0 & \frac{1}{L_4} & 0 & 0 \end{bmatrix}^T$$

As can be seen, the state parameters of the AC grid connection are the voltages of the capacitors $C_{net}$ and $C_{TL}$, and the currents flowing through inductances $L_3$ and $L_4$ (Fig. 3.21). The inputs are the total current feeding from the turbine converter models and the source voltage $V_S$ ($V_{s_d} = 1\ p.u.$ and $V_{s_q} = 0$). By selecting the d-axis grid voltage as the reference instead of the output voltage of each cluster, multiple clusters of converters can be easily added into the model, and each cluster is a stand-alone state-space model which is connected to the state-space model of the AC grid.

Fig. 3.22 shows the block diagram of the dynamic equivalent model of the parallel converter system. As shown in Fig. 3.22 the output currents of the clusters are the input for the AC grid connection state-space model. It is possible to study the stability of any numbers of parallel clusters of turbines that are connected to the grid as long as the output current of all the clusters is available. Fig. 3.23 shows the step response of the d-axis current for a system consisting of 2 parallel converters each of them rated 60 MW (lumped model of grid side converter of ten 6MW wind turbines) and SCR=5 (based on 120 MW system) for time domain simulation and state-space model developed in Fig. 3.22. As can be seen in Fig. 3.23, the two step responses are very similar, validating that the state-space model is sufficiently good to represent the wind farm in the stability studies.

The root locus for the closed loop d-axis current of the 2-converter system is shown in Fig. 3.24 when the SCR reduces from 100 to 1 with both converters exporting 1 p.u. active power. The direction of the arrows indicates the trend of poles with reducing SCR. As shown in Fig. 3.24, the poles move to an unstable region when the SCR becomes less than 1.67.

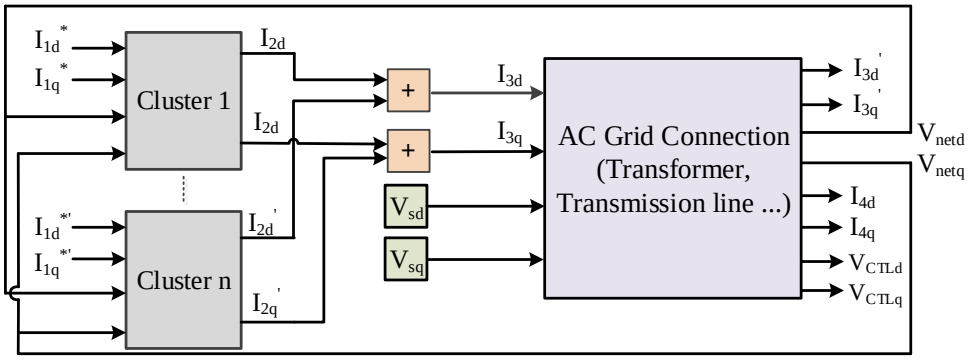

Fig. 3.22. Block diagram of a dynamic model of parallel converters.

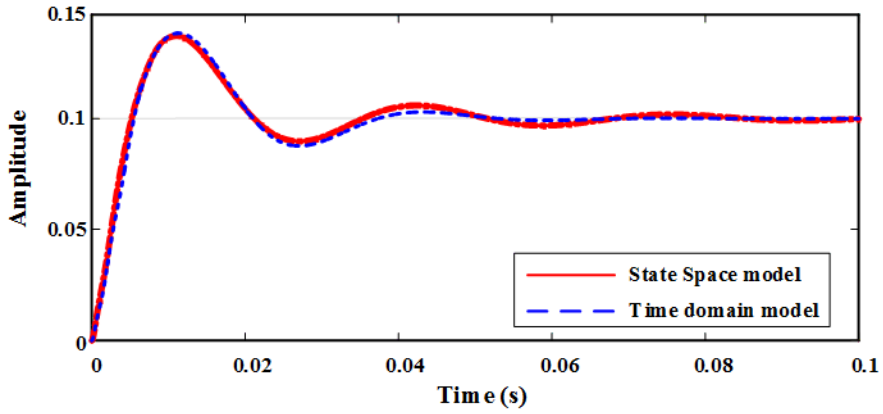


Fig. 3.23. Step response for d-axis current of a multiple converter system, SCR=5.

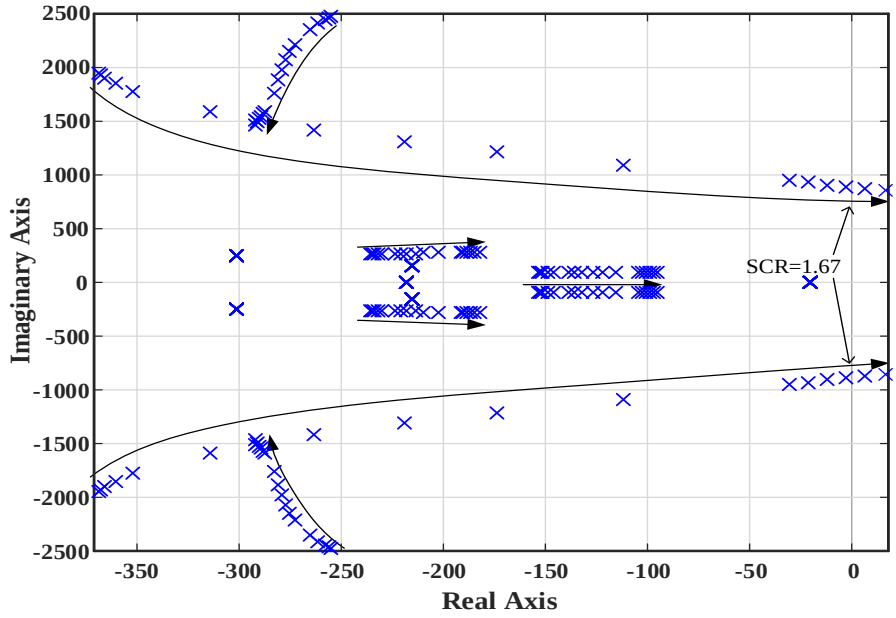


Fig. 3.24 . Root loci for d-axis current of one of the converters in a 2-converter system

For the two-converter system, the dependency of one converter stability on the other converter in weak grid condition is studied considering a step of 0.1 p.u. in the d-axis reference current of the second converter as the input to the system. The time response of the d-axis current of the first converter is shown in Fig. 3.25 for different grid strengths and the root locus for the same system is shown in Fig. 3.26. During the test, the power of the first converter is set at 0. The step change in the d-axis reference current of the second converter is seen as a disturbance to the other converter and as seen in Fig. 3.25, the oscillations of its output current increase with decreasing the

SCR value. This means that these oscillations might be added to the dynamics of the first converter and influence the stability of the system.

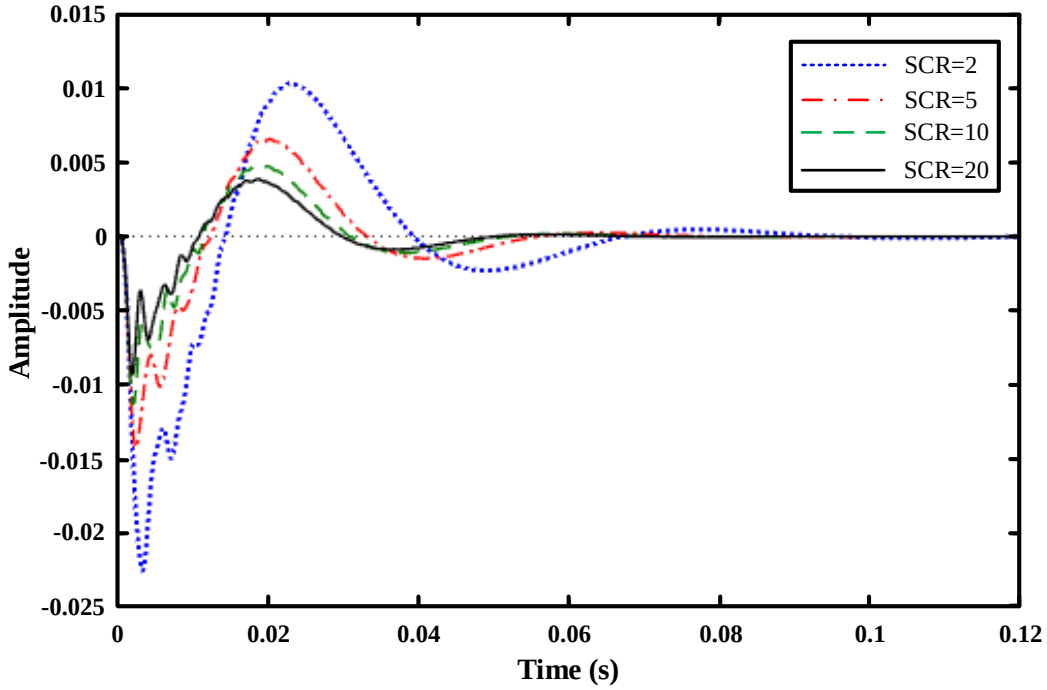


Fig. 3.25. Step response for d-axis current with input from the second converter and output of the first converter

On the other hand, it is seen in Fig. 3.26 that by weakening the grid the damping of the system decreases as the main poles of the system tend to move further right in a similar way as shown in Fig. 3.24. This means that the controller of the converter must be able to deal with the lack of damping in the system even when the other converters in the system add up adverse impacts on the system.

## 3.7. Outer Loop Modelling

The studies conducted so far only contain the current control loop (inner control loop). To have a comprehensive system model, it is required to include the outer control loops into the developed MIMO model. Active power/DC voltage control and reactive power/AC voltage control loops are usually utilised to provide the d-axis and q-axis current references respectively for the inner control loop.

Considering wind farm applications, the active power loop which controls the output power of the wind farm is investigated. Furthermore, an AC voltage droop controller which generates the q-axis current is used to regulate the AC voltage at the connection point of the wind farm to the grid.

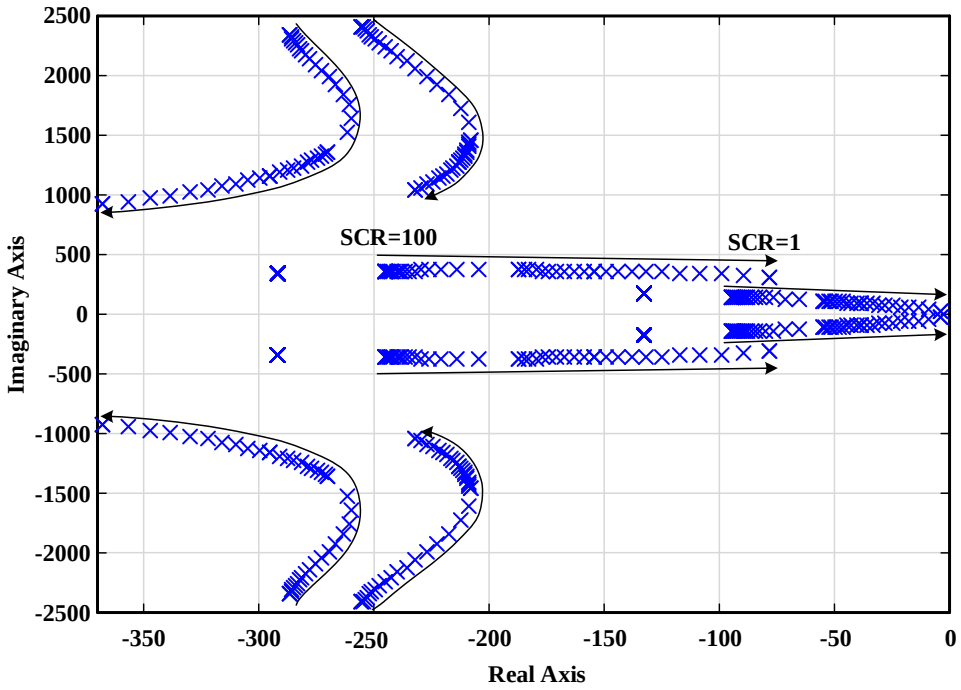


Fig. 3.26. Root locus for d-axis current with input from the second converter and output of the first converter

In the developed models, the grid source voltage is aligned with the d-axis of the synchronous reference frame. This means that the outputs of the system shown in Fig. 3.14 are calculated according to the grid voltage (i.e. $V_S$) angle reference. However, to model the outer control loop the filter bus voltage of each converter is employed. This means that the d-axis and q-axis current references ($I_{Cd}^*$ and $I_{Cq}^*$) obtained using this method have different SRF compared to that for the real active and reactive current values. Therefore, the calculated current reference values need to be adjusted according to the SRF of the grid voltage to be able to use them in the dynamic model of the system. As the phase angle of $V_S$ is zero, therefore, the calculated reference currents ($I_{Cd}^*$and $I_{Cq}^*$) can be transferred to the SRF of $V_S$ by considering only the phase angle of $V_C$ which is calculated by

$$\theta_C = arctan\frac{V_{Cq}}{V_{Cd}} \tag{3.37}$$

Hence, the reference currents based on the SRF of $V_S$ are obtained as

$$\boldsymbol{I}^*_{\boldsymbol{V}_{\boldsymbol{sdq}}} = \boldsymbol{I}^*_{\boldsymbol{dq}} e^{j\theta_C} = \begin{bmatrix} I_C{}^*_d \\ I_C{}^*_q \end{bmatrix} \begin{bmatrix} cos\theta_C & -sin\theta_C \\ sin\theta_C & cos\theta_C \end{bmatrix} \tag{3.38}$$

The complete system model is shown in Fig. 3.27.

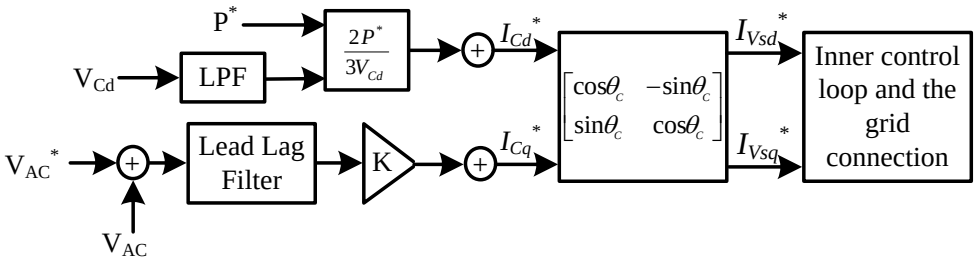


Fig. 3.27. Block diagram of the frequency domain model of the outer control loop

The d-axis current step responses of the model are compared in Fig. 3.28 for time domain and state-space simulations with SCR=5. These two responses match reasonably well. The developed model will be used later in Chapter 5 for further investigation and studies.

The root locus of the MIMO system including the outer control loops for different values of SCR is shown in Fig. 3.29. This also indicates that the system becomes unstable for very weak grids.

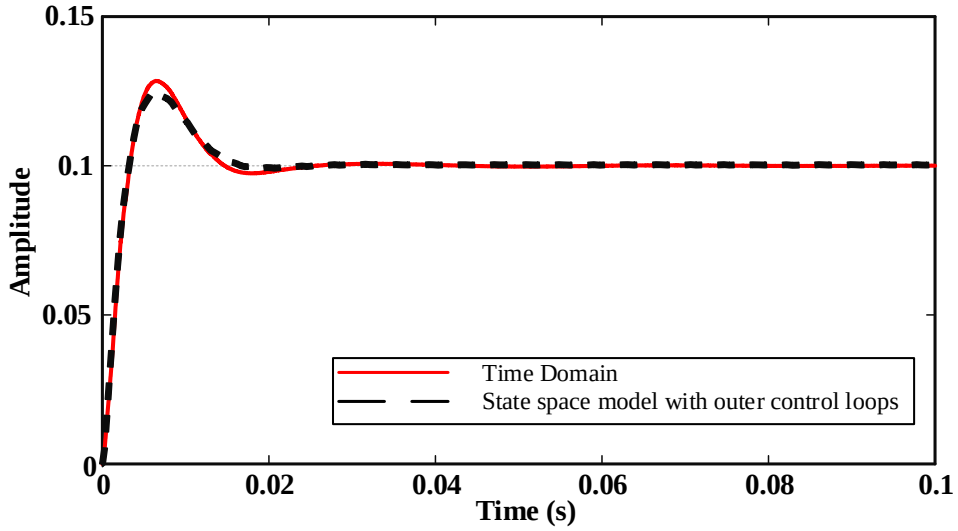


Fig. 3.28. The d-axis current step response for the MIMO model of system including an outer control loop

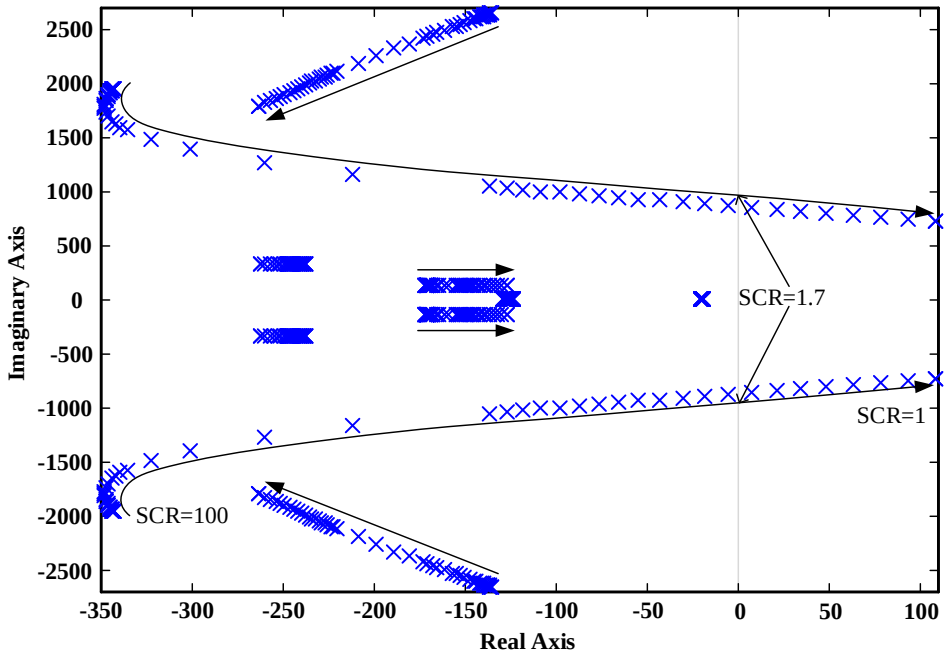


Fig. 3.29. d-axis current root loci for the MIMO model of a system including an outer control loop (direction of arrows: SCR=100 to SCR=1).

## 3.8. Summary

In this chapter, a grid connected VSC is modelled as a multiple-input-multiple-output system. The model includs the dynamics of the PLL and was verified by comparing the step responses of the developed MIMO system with a time domain model.

The AC grid connections in the system are modelled in three different ways with different levels of complexity. The presented results in this chapter show that as the frequency of interest is in the relatively low range (< 300 Hz), the simple model is sufficient for the frequency domain studies.

Furthermore, a MIMO model for a system including multiple converters is developed for stability studies. The studies show that the presence of multiple converters can lead to a reduction of damping in the overall system under weak grid conditions and could potentially make the system unstable. Finally, outer control loops are added to the developed state-space model for providing dynamic analysis of the complete system.

# 4. Improved Current Control of VSC with Current Error Based Compensation

In this chapter, a current error based angle and magnitude compensation control strategy is proposed which is implemented along side classical VSC vector control. This control strategy improves overall system stability and enables the VSC to deliver full rated power to a very weak grid. In contrast with the synchronous generator based control strategies [75, 88-94], the proposed control method eliminates the requirement of mode switching during steady state and transient operations. Further, the proposed strategy also benefits from easy implementation, simple control configuration and good robustness against variations of grid strength.

The main principles of the proposed control strategy are presented first and are followed by the system modelling and control analysis. Case studies during both steady state and AC fault conditions are presented to demonstrate the effectiveness of the proposed controller.

## 4.1. Principles of VSC Control and the Proposed Current Error Based Voltage Angle and Magnitude Compensation

A simplified single line schematic diagram of a 3-phase VSC connected to a power grid is shown in Fig. 4.1, where $R_1$ and $L_1$ represent the resistance and inductance of the VSC line inductor, respectively. C is the harmonic filter capacitance, $L_{tx}$ is the equivalent inductance of the converter transformer, and $R_{Net}$ and $L_{Net}$ are the equivalent resistance and inductance of the grid, respectively. $\boldsymbol{V_c}$ and $\boldsymbol{V_{conv}}$ refer to the respective AC filter capacitor voltage and the converter output voltage. $R_2$ and $L_2$ represent the equivalent grid side resistance and inductance seen at the converter side of the transformer. As in this chapter the main focus is on AC side integration, the impact of wind farm dynamics is assumed to be negligible and is not considered.

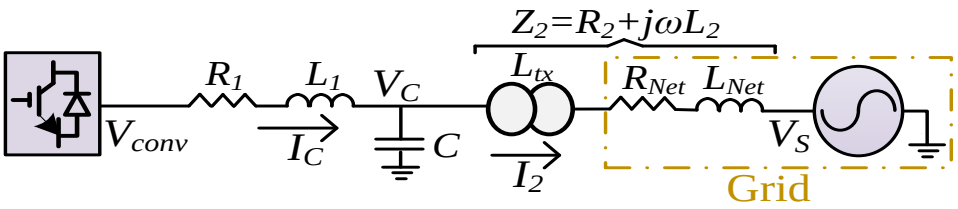


Fig. 4.1. Schematic of VSC connected to power grid.

As mentioned in Chapter 3, for the grid connected VSC shown in Fig. 4.1, there is

$$\boldsymbol{V_{Cdq}} = \boldsymbol{V_{convdq}} - L_1\frac{\mathrm{d}\boldsymbol{I_{Cdq}}}{dt} - j\omega L_1\boldsymbol{I_{Cdq}} - \boldsymbol{I_{Cdq}}R_1 \tag{4.1}$$

where $\boldsymbol{I_{cdq}}$ and $\boldsymbol{V_{cdq}}$ are the converter current and voltage vector in the dq reference frame respectively, and $\omega$ is the synchronous angular velocity.

The conventional vector current control strategy for VSC has been discussed in Section 3.2, and the simplified block diagram is shown in Fig. 4.2 [119] where a dq based control scheme is used in which the d-axis of the SRF is aligned to the AC voltage vector $V_c$ at the AC filter bus.

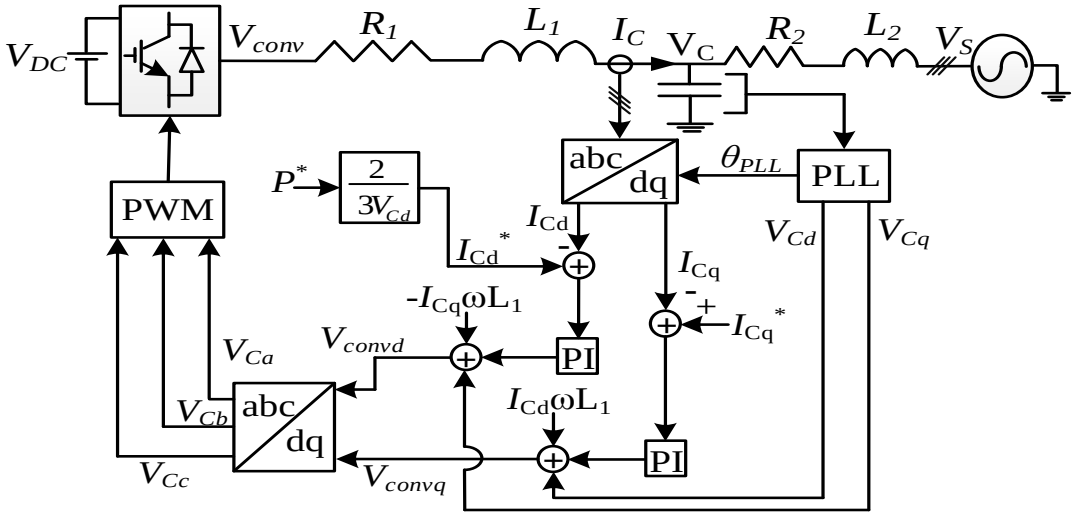


Fig. 4.2. Classical current vector control for VSC

Considering a very small time step $T_s$, the change of converter current during the $T_s$ period can be approximated from (4.1) as

$$\boldsymbol{\Delta I_{cdq}} \approx \frac{T_S}{L_1}\boldsymbol{V_{convdq}} - \frac{T_S}{L_1}\boldsymbol{V_{Cdq0}} - \frac{T_S}{L_1} j\omega L_1 \boldsymbol{I_{Cdq0}} - \boldsymbol{I_{Cdq}} R_1 \quad (4.2)$$

where $\boldsymbol{V_{cdq0}}$ and $\boldsymbol{I_{cdq0}}$ are the initial converter voltage and current at the start of the $T_s$ period, respectively.

Equation (4.2) shows the linearised relationship between $\boldsymbol{\Delta I_{cdq}}$ and $\boldsymbol{V_{convdq}}$. Therefore in conventional vector current control, $\boldsymbol{V_{convdq}}$ is used as the current regulation output to control the current $\boldsymbol{I_{Cdq}}$. The closed-loop control scheme shown in Fig. 4.2 is designed based on (4.2). Converter current error is set as the input and converter voltage as the output, as $\boldsymbol{V_{convdq}}$ is directly controllable for a VSC. As described in Section 2.4, using classical control for controlling a VSC connected to a weak grid can give rise to undesirable voltage and current oscillations [126].

Fig. 4.3 shows the results for a ramp power test for the grid connected VSC shown in Fig. 4.1 and conventional vector current control strategy of Fig. 4.2 with system parameters presented in Table 4.1. Current loop proportional and integral gains are set at $200\pi L_1$ and $10000\pi^2 L_1$ respectively for 50 Hz current loop bandwidth with 2.5 kHz switching frequency [124].

Table 4.1. Parameters for the simulated VSC system

| Parameter | Symbol | Value |
|---|---|---|
| Rated power of VSC | P | 60 MW |
| Short circuit ratio | SCR | 1 |
| Converter reactor inductance | $L_1$ | 0.2 p.u. |
| Converter reactor resistance | $R_1$ | 0.001 p.u. |
| Filter capacitor | C | 0.1 p.u. |
| Transformer inductance | $L_{tx}$ | 0.1 p.u. |

As shown in Fig. 4.2, conventional vector control is able to regulate the current/power when the generated power is low, and the error between the actual and PLL measured AC voltage angles of $\boldsymbol{V_C}$ converges to around 0. However, when the power output of the VSC rises to approximately 65% of the rated power, the system becomes unstable, the angle error between the actual and PLL measured AC voltage starts to oscillate as does the power. It can be seen that the oscillation frequency is approximately 40 Hz for this case.

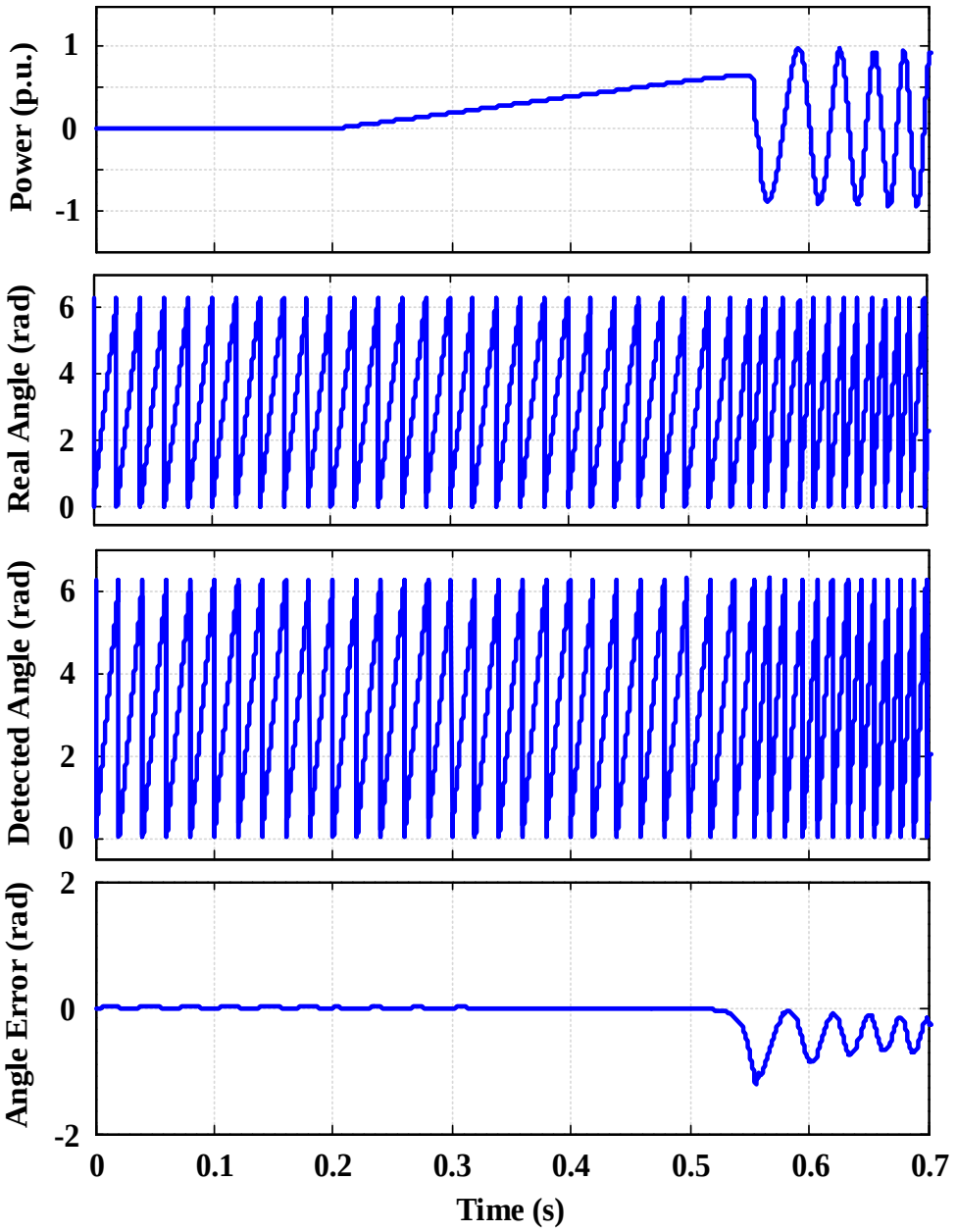


Fig. 4.3. Power ramp test with conventional vector control (from top to bottom: active power, actual voltage angle of ***Vc***, PLL detected voltage angle of ***Vc***, error between the actual and measured angle of ***Vc***)

In order to overcome the angular error oscillations and to avoid system instability, an angular tracking strategy is proposed in this chapter to enhance system performance and damp the angular and power oscillation, thereby improving system stability.

Assuming the voltage vector is aligned with the d-axis, and the resistance $R_1$ of the VSC coupling inductor is negligible, the VSC steady-state output active power P is expressed as [121]

$$P = \frac{3}{2} V_{Cd} I_{Cd} = \frac{V_{conv} V_{Cd}}{\omega L_1} sin\delta \tag{4.3}$$

where δ is the voltage angle difference between the converter output $\boldsymbol{V_{conv}}$, and grid integration point $\boldsymbol{V_C}$. Assuming $V_{Cd}$ remains constant, (4.3) is linearized as

$$\frac{2dP}{3V_{Cd}} = dI_{Cd} = \frac{2V_{conv0}}{3\omega L_1} d(sin\delta) + \frac{2sin\delta_0}{3\omega L_1} dV_{conv} \tag{4.4}$$

Rearranging (4.4) gives

$$\Delta I_{Cd} \approx \frac{2\boldsymbol{V_{conv0}}}{3\omega L_1} \Delta\delta + \frac{2sin\delta_0}{3\omega L_1} \Delta \boldsymbol{V_{conv}} \tag{4.5}$$

where $\boldsymbol{V_{conv0}}$ and $\delta_0$ are the static operating points of $\boldsymbol{V_{conv}}$ and δ, respectively. Using (4.5), the incremental current $\Delta I_{Cd}$ is approximated as a function of $\Delta\delta$.

Equation (4.5) consists of two independent terms, $\Delta V_{conv}$ and $\Delta\delta$, where each has a linear relationship with $\Delta I_{Cd}$. Since $\delta_0$ is in vicinity of zero and $\boldsymbol{V_{conv0}}$ is around 1

$$\left|\frac{2\boldsymbol{V_{conv0}}}{3\omega_s L_1}\right| \gg \left|\frac{2sin\delta_0}{3\omega_s L_1}\right| \tag{4.6}$$

It can be concluded that Δδ has a bigger impact on active current change than $\Delta V_{conv}$ and hence is used as the output of angle compensation, shown in Fig. 4.4 (a). This is similar to the control design in Fig. 4.2 based on (4.2). Thus, an additional active current control is proposed to add regulation with angle compensation as another output in parallel with the conventional vector control, as shown in Fig. 4.4 (a). By adding this additional control loop, angle tracking in the system is improved by adding extra damping and meanwhile the main current control loop continues providing a fast dynamic response during the occurrence of large perturbations and transients in the system.

Similar to (4.3)-(4.5), for reactive power, there is [121]

$$\mathrm{Q} = -\frac{3}{2}V_{Cd}I_{Cq} = \frac{\boldsymbol{V_{conv}}(\boldsymbol{V_{conv}}-V_{Cd})}{\omega L_1}cos\delta \tag{4.7}$$

Assuming that $V_{Cd}$remains constant, there is

$$\frac{dQ}{\mathrm{dt}} = -\frac{3V_{Cd}}{2}\frac{dI_{Cq}}{\mathrm{dt}} = \frac{\boldsymbol{V_{conv0}}(\boldsymbol{V_{conv0}}-V_{Cd})}{\omega L_1}\frac{d(cos\delta)}{\mathrm{dt}} - \frac{cos\delta_0}{\omega L_1}(2.\boldsymbol{V_{conv}} - V_{Cd})\frac{d\boldsymbol{V_{conv}}}{\boldsymbol{dt}} \tag{4.8}$$

$$\frac{2dQ}{3V_{Cd}} = dI_{Cq} = -\frac{2\boldsymbol{V_{conv0}}(\boldsymbol{V_{conv0}}-V_{Cd})}{3\omega L_1}d(cos\delta) - \frac{2cos\delta_0}{3\omega L_1}(2\cdot\boldsymbol{V_{conv0}} - V_{Cd})d\boldsymbol{V_{conv}} \tag{4.9}$$

Rearranging (4.9) gives

$$\Delta I_{Cq} \approx \frac{2\boldsymbol{V_{conv0}}}{3\omega L_1}sin\delta\Delta\delta - \frac{2cos\delta_0}{3\omega L_1}(2\boldsymbol{V_{conv0}} - V_{Cd})\Delta\boldsymbol{V_{conv}} \tag{4.10}$$

Similar to the active current case, taking into account that $\Delta\delta$ has been used for active current control and considering the linear relationship between $\Delta I_{Cq}$ and $\boldsymbol{\Delta V_{conv}}$, an enhanced reactive current control with voltage magnitude compensation is proposed with $\boldsymbol{\Delta V_{conv}}$ as the output of the controller, as shown in Fig. 4.4 (b). This control loop helps to stabilise the AC voltage of the system by accurately controlling the reactive current. The impact of the proposed compensation control method on system stability will be analysed and validated later in this chapter.

In addition to dynamic regulation, the static AC voltage control has to be considered taking into account that the reactive power flow plays a very important role in the system stability for a very weak AC grid [83]. A voltage magnitude feedback closed-loop droop controller is placed in Fig. 4.4(c) and a lead-lag filter is employed here to ensure that a sufficient phase margin is available for the AC voltage controller if a large proportional gain, K, is used [120].

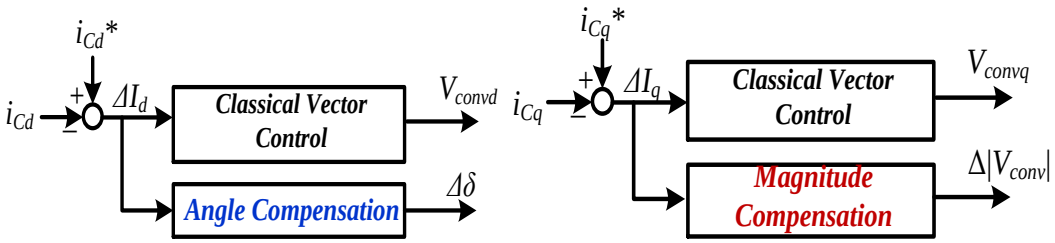


(a) angular compensation (b) voltage compensation

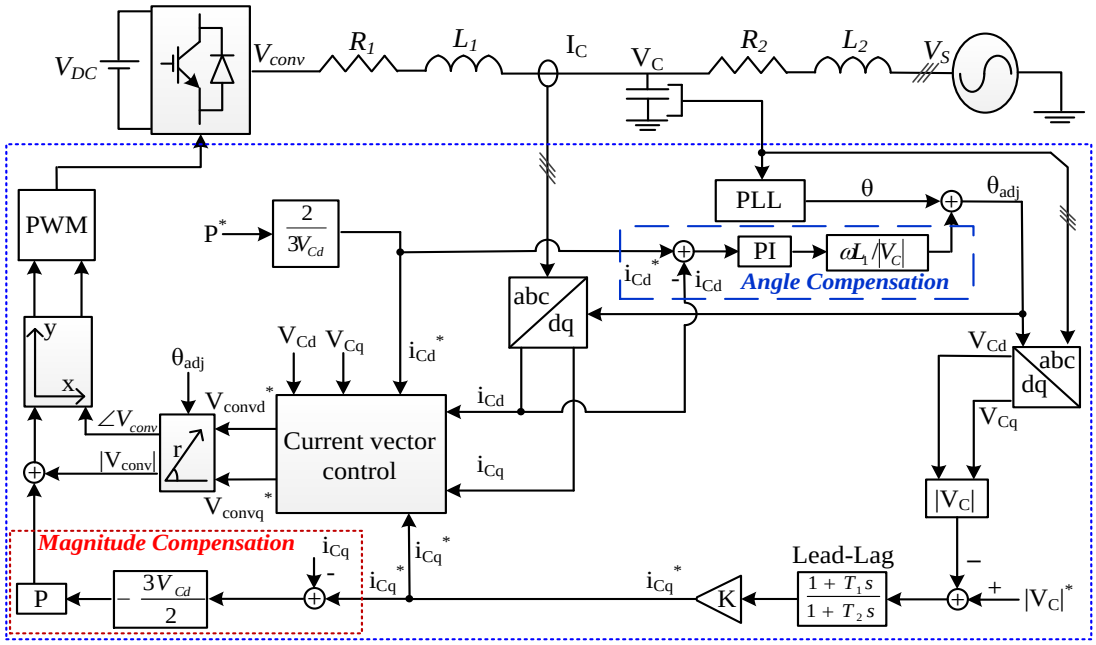


(c) VSC vector control scheme with compensation

Fig. 4.4. VSC with current vector control and proposed current error based compensation

## 4.2. Analytical Model and System Analysis

A small-signal analytical model of the whole system including the proposed angle and voltage magnitude compensation control is established in the SRF based on Chapter 3, and the relevant frequency domain analysis is presented using root locus method. In this section, for simplicity, the modelling and analysis focus on the current loop.

The block diagram in Fig. 4.5 shows the comprehensive small-signal analytical model that includes the dynamic system model developed in Chapter 3 and the proposed current error based compensation control loops. In Fig. 4.5, $K_{pdC}$ and $K_{idC}$ are the proportional and integral gains of the angle compensation respectively, and $K_{pdC}$ is the proportional gain of the voltage magnitude compensation. $V_{cd0}$ and $\theta_0$ refer to the static operating points of $V_{cd}$ and $\theta$ respectively. $K_{pd}$ and $K_{id}$ are the PI regulator gains of the d-axis current loop, whereas $K_{pq}$ and $K_{iq}$ refer to the gains of the PI regulator of the q-axis current loop.

Based on the block diagram in Fig. 4.5, root locus analysis is carried out for the closed-loop system of the d-axis current with various SCR values. Assuming the VSC power and grid AC voltage are set at rated values, and the other parameter values are shown in Table 4.2, the static operational point is obtained as

$$x_0 = [0.910, -0.414, 0.917, -0.417, -0.867, 0.502]^{\mathrm{T}}$$

$$u_0 = [1\ ,0\ ,0.980\ ,0.347]^{T}$$

where $x_0$ and $u_0$ are the initial values for the states and the input vector of the system presented in (3.21).

The root locus for the poles of the system for classical vector current control of VSC shown in Fig. 4.1 is obtained as Fig. 4.6 (a) when the proposed compensation controls are not included in the system analysis. From Fig. 4.6 (a), it is seen that the dominant poles of the d-axis current loop system move towards the right plane when the SCR value is decreased from 100 to 1. This shows that a VSC controlled using the classical vector control tends to become poorly damped or even unstable when the main grid connection becomes very weak. The corresponding natural frequency of the dominant pair of closed-loop poles can be calculated from Fig. 4.6 and is around 40 Hz when the SCR is close to 1, which corresponds well with the time domain simulation shown in Fig. 4.3.

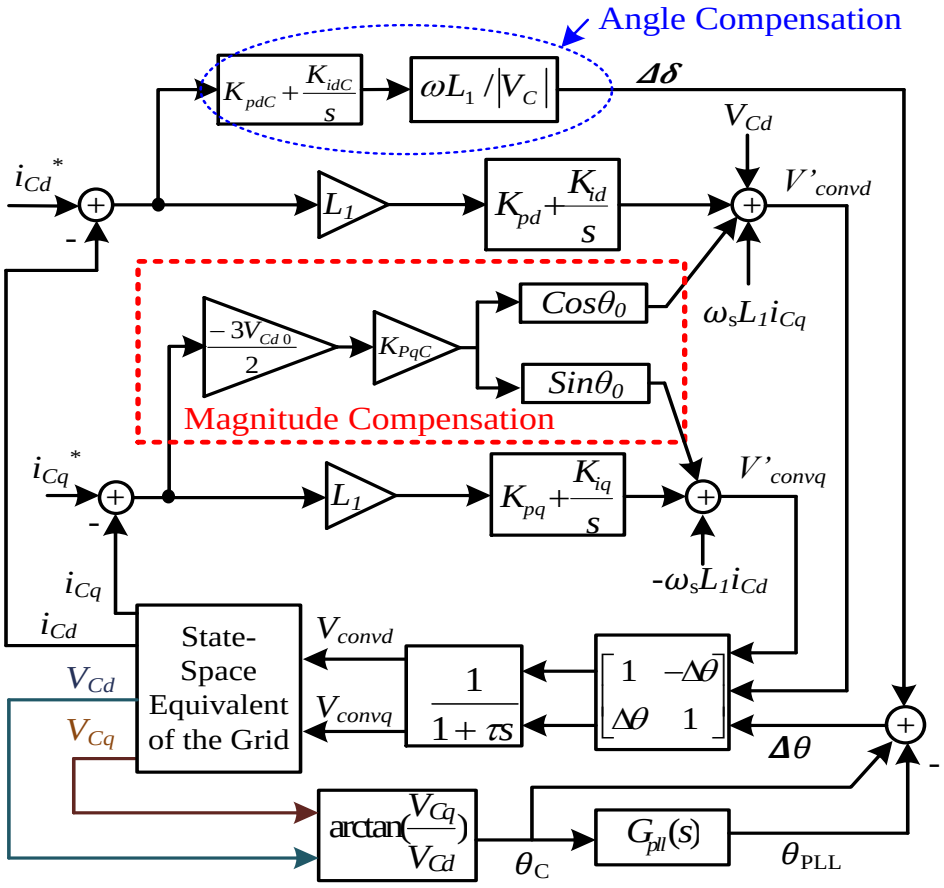


Fig. 4.5. Block diagram of the VSC analytical model in the frequency domain

Table 4.2. System initial parameters

| Parameter | Symbol | Value |
|---|---|---|
| Transformer inductance | $l_{tx}$ | 0.1 p.u. |
| Transformer ratio | $N_{tx}$ | 0.69/33 kV |
| VSC nominal voltage | $V_n$ | 690 V |
| Reactor inductance | $L_1$ | 0.2 p.u. |
| Filter capacitance | $C_f$ | 0.1 p.u. |
| Current controller proportional gains | $K_{pd} = K_{pq}$ | $141\pi$ |
| Current controller integral gains | $K_{id} = K_{iq}$ | $10000\pi^2$ |
| PLL proportional gain | $k_{p_{PLL}}$ | 178 |
| PLL Integral gain | $k_{i_{PLL}}$ | 3947 |
| Voltage controller droop gain | K | 13 |
| Short circuit ratio | SCR | 1 |
| Angle compensation proportional gain | $K_{pdC}$ | 0.2 |
| Angle compensation integral gain | $K_{idC}$ | 4 |
| Magnitude compensation gain | $K_{pqC}$ | 0.2 |
| Lead-lag filter nominator time constant | $T_1$ | 0.002 s |
| Lead-lag filter denominator time constant | $T_2$ | 0.01 s |

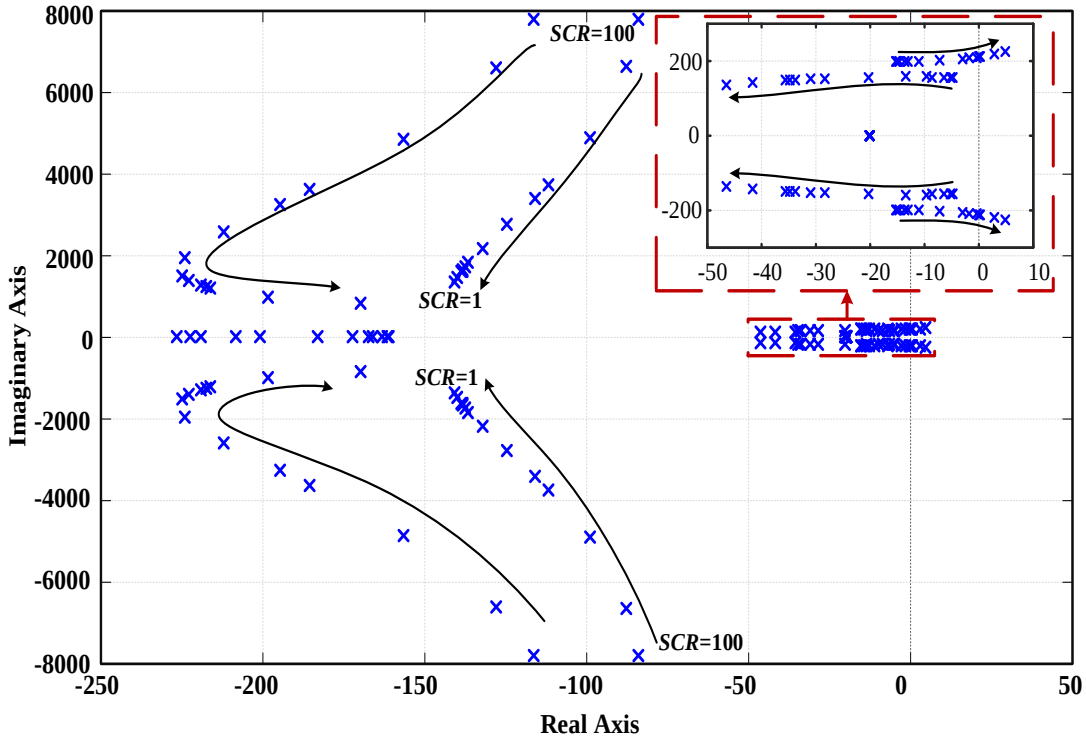


(a) Conventional control without compensation

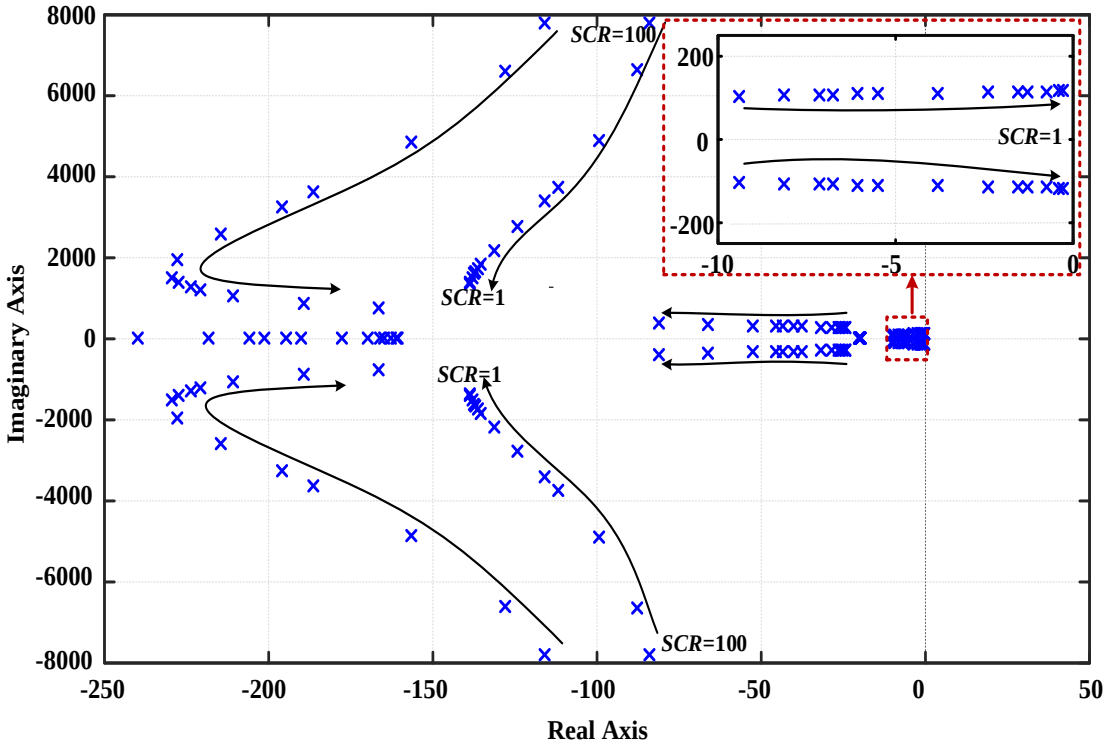


(b) With angle compensation only

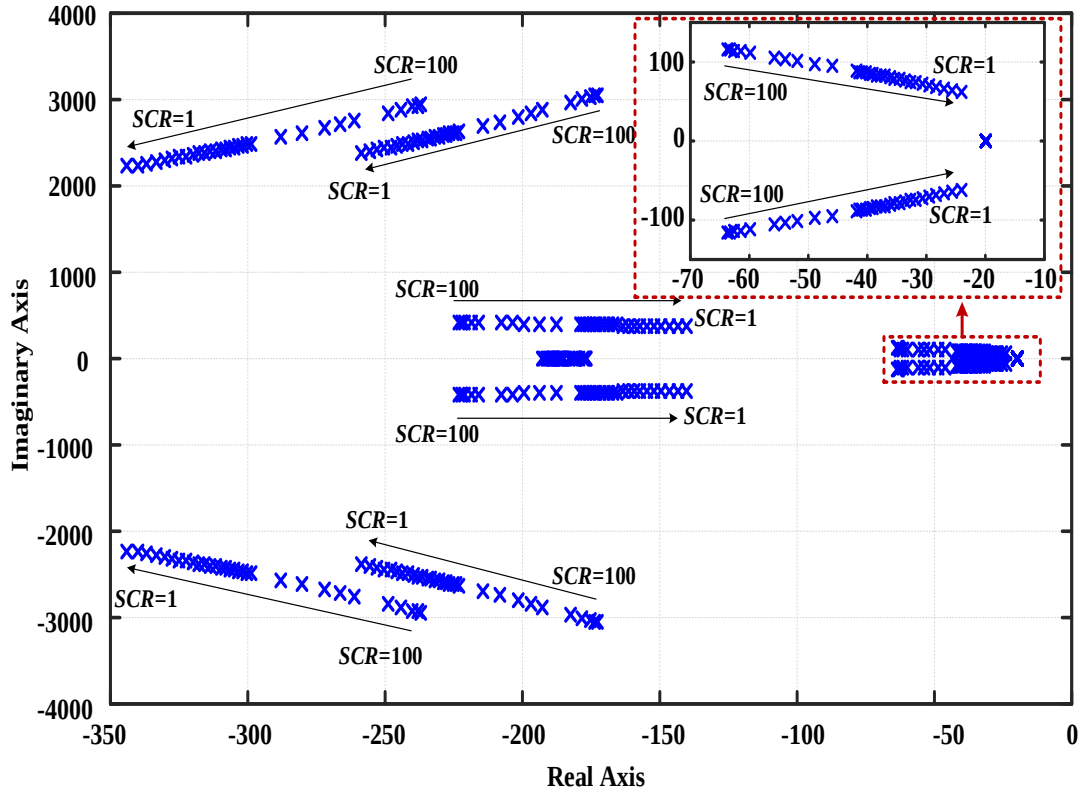


(c) With angle and magnitude compensation

Fig. 4.6. Root locus (rated current, SCR = 100 to 1)

By adding the proposed angle compensation control only, the corresponding root locus of the dominant poles of the system shown in Fig. 4.6 (b) reveals that the dominant poles are kept in the left plane even when the grid connection is very weak as the SCR goes to 1. This confirms that the proposed angle compensation control can stabilise the VSC system with current control loop when connected to a very weak grid. However, although the stability of the system has been significantly improved, the damping of the system is relatively low when the SCR becomes as low as 1. As can be seen in Fig. 4.6 (b), the real part of the dominant poles reaches -0.5 and the imaginary part is just over 100 for SCR = 1, which means that the system has a poor damping ratio of 0.0025. Therefore, it can be concluded that the proposed current-error based angular compensation can stabilise the system by pushing the poles to the left plane, which is a significant improvement from the unstable cases with conventional vector current control. However, when the grid connection is very weak, the system has relatively poor damping.

Fig. 4.6 (c) shows the root locus of the dominant poles of the system with both angle and voltage magnitude compensation. It can be seen in Fig. 4.6 (c) that the dominant poles in the system show an improved damping performance as the damping ratio of the dominant pole pairs at SCR = 1 increased to 0.4 (i.e. Approximately 160 times larger than the case shown in Fig. 4.6 (b)).

## 4.3. Time Domain Case Studies

In this section, time domain simulation results for the proposed current error based compensation control loop are presented. Different cases, including power ramp, parallel converters and AC fault conditions, are tested for the system shown in Fig. 4.1 with parameters shown in Table 4.2.

### 4.3.1. Power Ramp Case Study

In this section, a power ramp test using the proposed current error based control is performed for a lumped VSC model representing a cluster of 10 wind turbines each rated at 6 MW and connected to a very weak grid (i.e. SCR = 1). The simulation results in Fig. 4.7 show the case in which the active power is ramped up at t= 0.5 s from 0 to 1 p.u. at a rate of 6.66 p.u./s and down to 0 again with the same rate. It is seen in Fig. 4.7 that the AC voltage is well controlled, and the active power stays stable during this test which means that the proposed angle and voltage magnitude compensation control regulate the VSC effectively even when connected to a very weak grid. The error between the real and the detected voltage angles is shown in Fig. 4.7 . It can be seen that this angle error is maintained in the vicinity of 0 during the ramp and in the steady state, which proves that the proposed active current error based angle compensation leads to stable AC voltage and improved PLL angle tracking. Thus, the overall system stability is improved as the active and reactive components of power and current are well controlled.

Fig. 4.8 illustrates the maximum power transferring capability of the VSC for different grid strengths (i.e. different SCR values). As shown in Fig. 4.8, the classical vector control is not capable of transferring the rated power (i.e. 1 p.u.) when SCR is less than

1.5. For example, when the SCR decreases to 1, the maximum power that can be transferred by the VSC before the occurrence of system instability is only 0.63 p.u.. this will make problems for connection of new offshore wind farms to the grid. In contrast, as shown by the dotted line in Fig. 4.8, the VSC controlled by the proposed compensation technique is capable of transferring 1 p.u. power even with SCR=1.

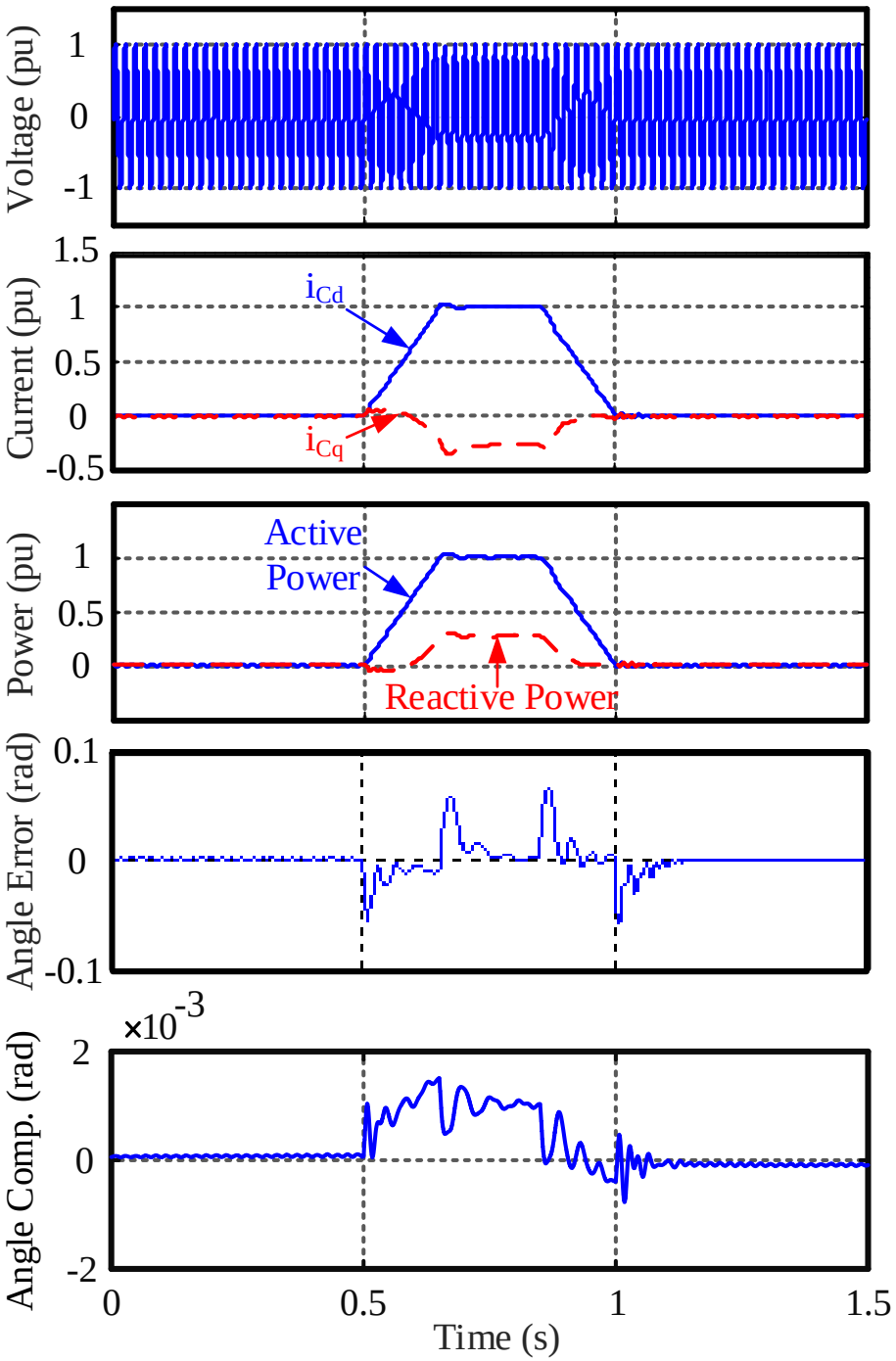


Fig. 4.7. Power ramp test (full power, SCR=1)

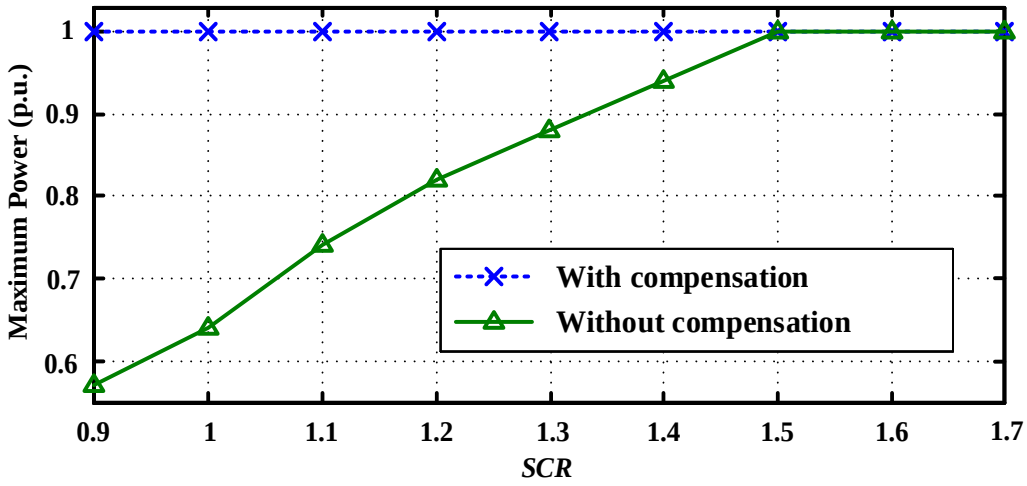


Fig. 4.8. Power transferring capability

### 4.3.2. Multiple Parallel VSC Test

Large onshore and offshore wind farms consist of many wind turbines and to improve the overall wind farm reliability, all the turbines are divided into clusters [23]. In this section, simulations are carried out considering two parallel lumped VSCs representing two clusters in a large wind farm. Each of the VSCs is rated at 0.5 p.u. of the rated power of the wind farm, and the grid connection is again very weak (i.e. SCR=1). Power transfer capability of the wind farm is tested using a ramp power reference to the VSCs for conventional vector current control and the proposed current error based compensation control loops.

Fig. 4.9(a) shows the results of the power ramp test for the two parallel VSCs using conventional vector current control. In Fig. 4.9(a), the output power of VSC 1 is ramped up first from 0 to 0.5 p.u. from t=0.05 s at a rate of 2.5 p.u. /s. VSC 2 starts to power up with the same ramp rate from t=0.15 s. As shown, the output power of both VSCs starts to oscillate before VSC 2 reaches its rated value. This means that the wind farm is not capable of transferring full power with SCR=1. However, using the proposed compensation control method, full rated power of the two VSCs can be transferred without compromising system stability as shown in Fig. 4.9 (b).

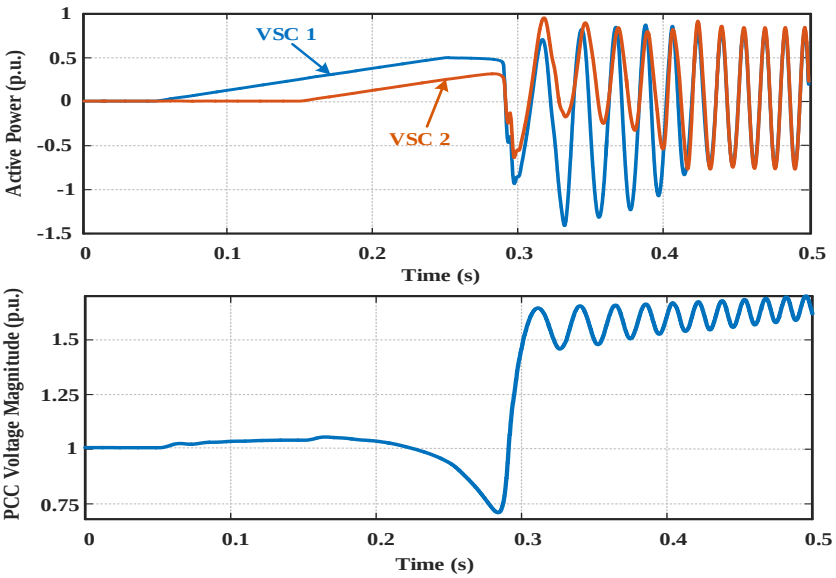


(a) Conventional vector control

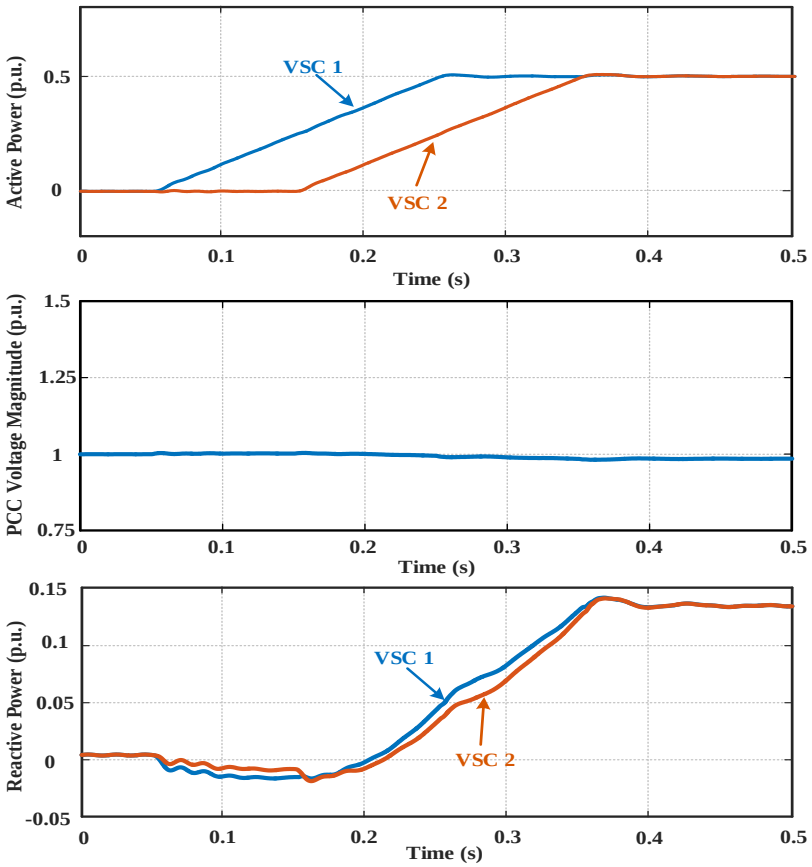


(b) With the proposed control

Fig. 4.9. Parallel VSC power ramp test (full power, SCR=1)

### 4.3.3. AC Fault Test (Fault-Ride-Through Test)

As mentioned in Section 4.1 of this chapter, the proposed compensation control retains the capability of controlling the VSC current during large voltage perturbation without the need for switching the control mode as required in the other control methods based on the virtual synchronous generator [75]. Since the three-phase fault is considered as the most severe fault case when considering fault current, relevant tests are carried out during three-phase faults to demonstrate the effectiveness and robustness of the proposed compensation control with various grid strengths.

As the grid connection is very weak, a voltage dependent current limit (VDCL) as shown in Fig. 4.10 is employed in order to reduce AC voltage overshoot after fault clearance [119]. By employing the VDCL, the VSC active current is limited according to the AC voltage level during the AC fault. Moreover, the reactive current is also capped at ±0.5 p.u. during the AC fault.

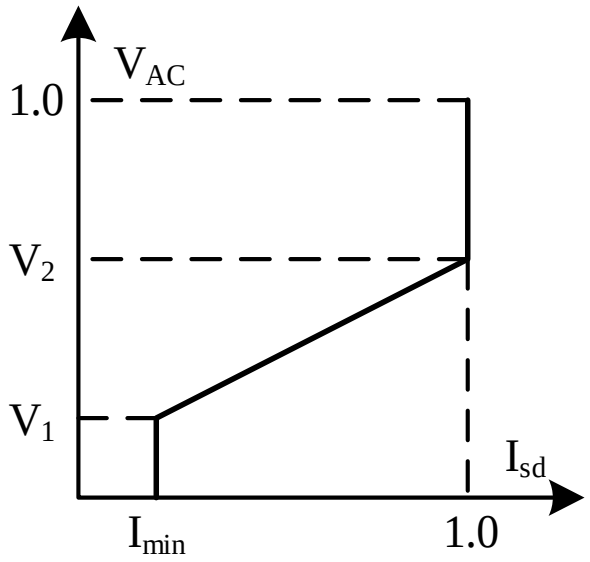


Fig. 4.10. Voltage dependent active current limit

Simulation results for three different SCR values (SCR=1, 2, and 10) are presented in Fig. 4.11 (a), (b) and (c), respectively. For all the simulations with different SCRs, the control parameters are kept constant as shown in Table 4.2 and the VSC exports rated active power (1 p.u.) prior to the three-phase AC fault.

Fig. 4.11 (a) illustrates the simulation results for SCR = 1 with a solid (zero impedance) three-phase AC fault at the secondary side of the transformer at t=0.1 s. As a consequence, the AC voltage drops to almost zero immediately after the fault occurrence. However, the VSC continues controlling the AC current and limits the maximum instant current overshoot to around 0.15 p.u..

As seen in Fig. 4.11 (a), both the d- and q-axis current components of the VSC are well controlled within their specified limits during the fault, demonstrating one of the advantages of this control method.

The fault is cleared at t=0.18 s, and the active power is recovered to the rated power according to the VDCL shown in Fig. 4.10. Due to the very weak grid, fault clearance introduces small oscillation of the PCC voltage leading to some current variations during the transient. However, the VSC current remains within its limits (rated current) throughout the recovering process. The voltage comes back to its nominal values quickly, and the VSC resumes its pre-fault operating condition in approximately 0.12 s after fault clearance.

The test in Fig. 4.11(a) confirms that the proposed current error based compensation control is capable of regulating the VSC current during both steady state and large transients.

For SCR values of 2 and 10 with identical control parameters to those for the previous case where SCR = 1, the results shown in Fig. 4.11 (b) and (c) indicate that the VSC currents remain well controlled between the limits during the fault and recovery process. This demonstrates the robustness of the proposed control against grid strength variation, which could happen in power systems in the case of line trips, load changes, etc.

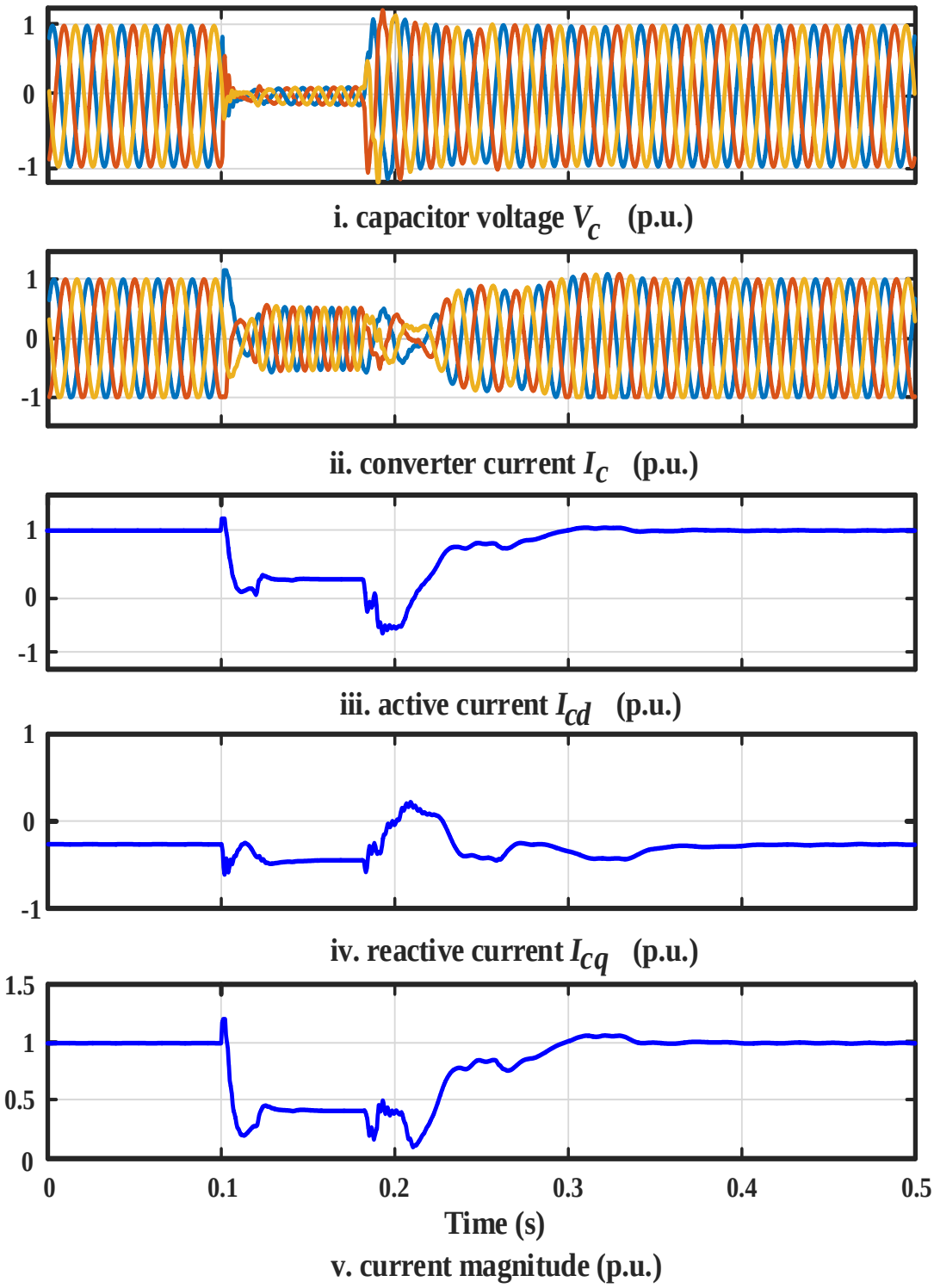
1
0
-1
i. capacitor voltage $V_c$ (p.u.)
1
0
-1
ii. converter current $I_c$ (p.u.)
1
0
-1
iii. active current $I_{cd}$ (p.u.)
1
0
-1
iv. reactive current $I_{cq}$ (p.u.)
1.5
1
0.5
0
0
0.1
0.2
0.3
0.4
0.5
Time (s)
v. current magnitude (p.u.)

(a) SCR = 1

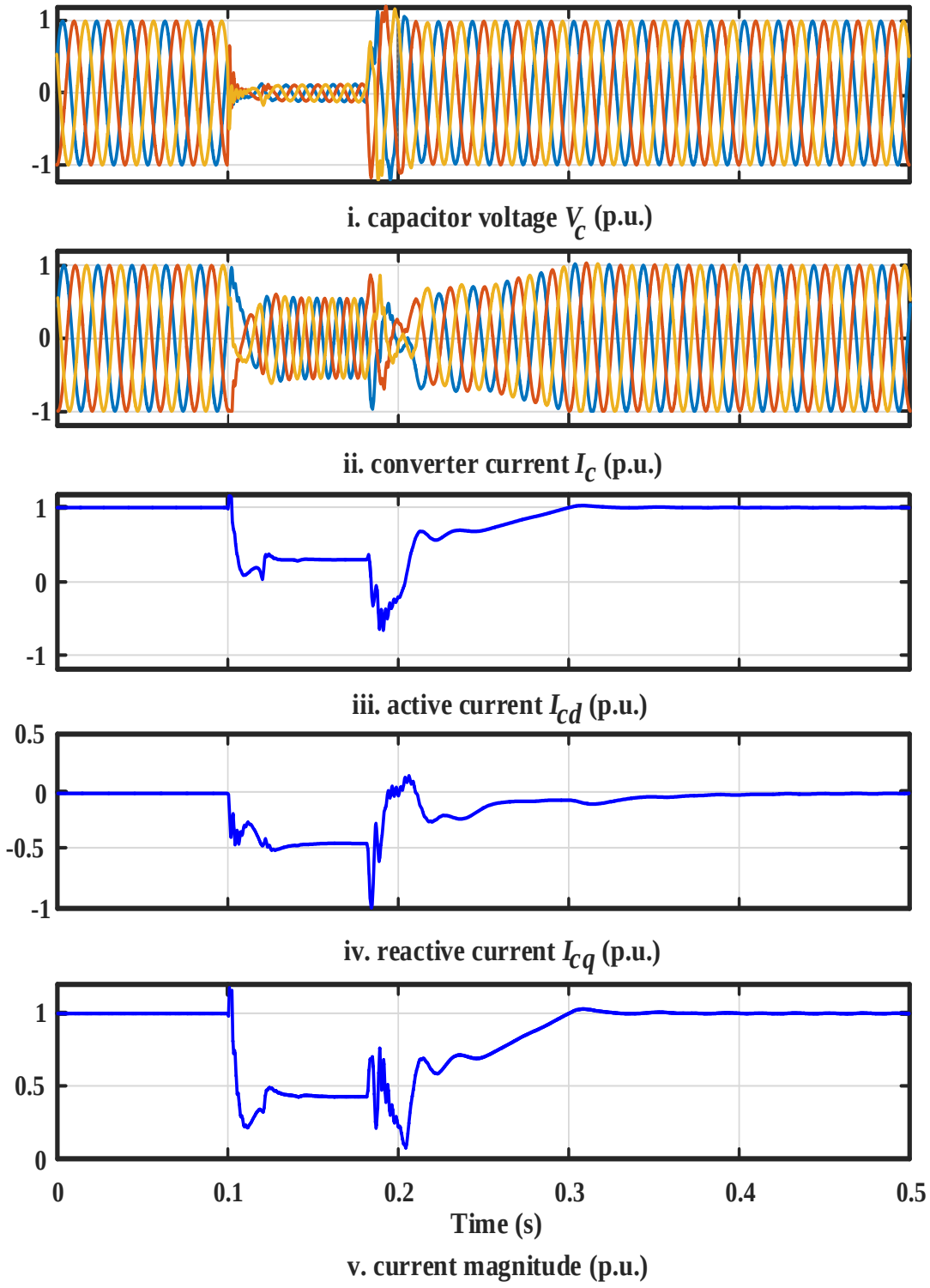
1
0
-1
i. capacitor voltage $V_c$ (p.u.)
1
0
-1
ii. converter current $I_c$ (p.u.)
1
0
-1
iii. active current $I_{cd}$ (p.u.)
0.5
0
-0.5
-1
iv. reactive current $I_{cq}$ (p.u.)
1
0.5
0
0
0.1
0.2
0.3
0.4
0.5
Time (s)
v. current magnitude (p.u.)

(b) SCR=2

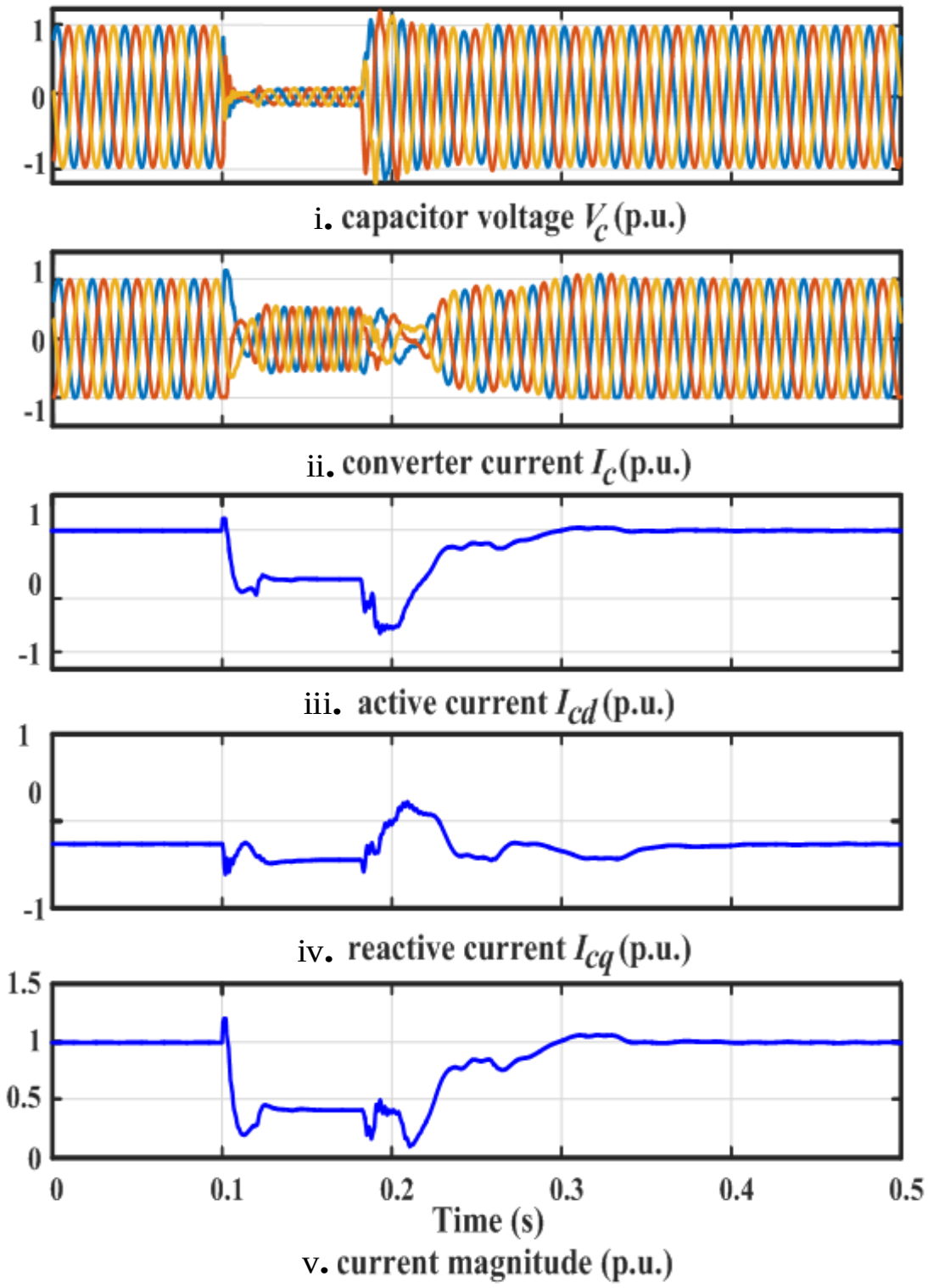


(c) SCR = 10

Fig. 4.11. Fault ride through

## 4.4. Summary

A VSC controlled by the conventional vector control normally has stability problems when it is transferring more than 60% of the rated power to a very weak grid. In this chapter, novel current error based compensation controls are proposed for a VSC connected to weak AC grid with closed-loop current regulation. The proposed compensation can be applied by considering the small-signal linear relationships between active current and voltage angle, and reactive current and voltage amplitude, respectively.

In the weak grid condition, the PLL cannot precisely track the voltage angle during transients which leads to active power/current error. Thus, the proposed control method uses the d-axis current error to calculate a correction to be added to the output angle of the PLL. Furthermore, the q-axis current error is used to calculate an enhanced reactive current control to compensate the voltage magnitude to stabilise the AC voltage of the system by accurately controlling the reactive current.

Based on frequency domain analysis, the proposed active current compensation can significantly improve stability performance by enhancing the conventional angular tracking method with a PLL, and meanwhile, the reactive current compensation can further enhance system damping under weak grid conditions.

Time domain simulations show that the proposed control can significantly increase the power transferring capability of a wind farm connected to a weak grid. The case study also demonstrates that the proposed current control can work well both in single or multiple converter situations and during a severe AC fault. The proposed methods can further benefit from its simple implementation and robustness against grid strength variations.

# 5. Virtual Impedance Based Stabiliser for Wind Farm Integration into Very Weak Grids

In this chapter, a virtual impedance based stabilising controller is proposed to improve system stability when VSCs are connected to very weak grids. Similar to the current error based compensation proposed in Chapter 4, this method retains the main property of current vector control and requires no control mode switching during transients. Thus, for practical applications, the proposed method offers high flexibility in implementation.

In Chapter 2, different control methods for connecting VSCs to a weak grid were presented, whereas, in Chapter 4, a current error based compensation control method was proposed to enable the integration of VSC to a very weak grid. All of these methods have to be integrated into the VSC controllers necessitating the amendment of every wind turbine control unit.

The proposed control method in this chapter can be either embedded in the VSC controllers or used separately in a relatively low power VSC system with a small-scale energy storage system.

In order to prove the effectiveness of the proposed virtual impedance control, a comprehensive frequency domain model is established based on the previously developed one, and the root locus of the system is analysed. Time domain simulations are carried out using Matlab/Simulink to validate the performance of the proposed controller in different test cases e.g. power ramp, transient, etc.

## 5.1. Principles of operation of Virtual Impedance Voltage Stabiliser

### 5.1.1. Dynamic Operating Point Based on System Power Flow

The single-line schematic diagram of the VSC connected to a grid that includes the power flow directions is shown in Fig. 5.1 which was used for the studies in previous chapters. The power flow constraints of the system shown in Fig. 5.1 is discussed in this section.

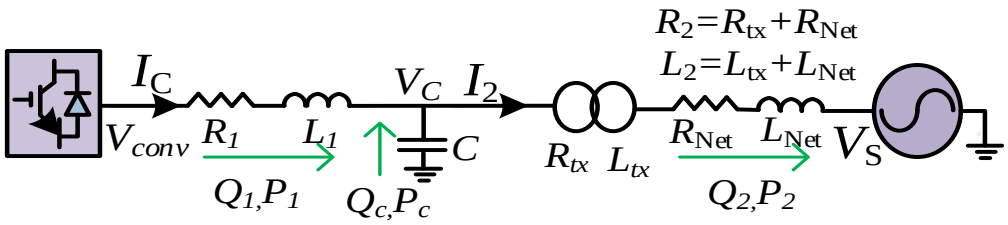


Fig. 5.1. Schematic of VSC connected to power grid with power flow direction

The system shown in Fig. 5.1 is a non-linear system, and therefore the operational point of the system needs to be determined using power flow analysis before the small-signal analysis can be carried out using the calculated operational points.

To estimate the power flow of the system, the resistance of the transmission line is assumed to be negligible compared with its reactance. Therefore, the system shown in Fig. 5.1 can be redrawn in phasor variables as in Fig. 5.2.

Under steady-state, from Fig. 5.2 there is

$$|V_C|e^{j(\theta_C)} = |V_S| + \boldsymbol{I_2} \cdot j\omega L_2 \tag{5.1}$$

The current to the grid (i.e. $I_2$) is then calculated as

$$\boldsymbol{I_2} = conj\left(\frac{P_2+jQ_2}{V_C}\right) = \frac{P_2-jQ_2}{conj(\boldsymbol{V_C})} \tag{5.2}$$

where $P_2$ and $Q_2$ are the active and reactive power transferred to the grid, respectively.

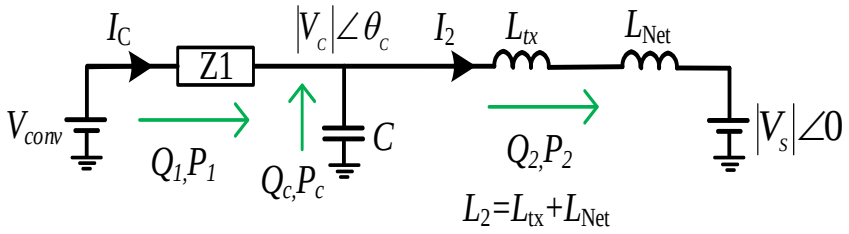


Fig. 5.2. Schematic circuit diagram for power flow analysis

Substituting (5.2) into (5.1) gives

$$|V_C|^2 = conj(\boldsymbol{V_c})\boldsymbol{V_S} + jP_2\omega L_2 + Q_2\omega L_2 \tag{5.3}$$

It is assumed that the grid voltage is the 'base voltage' for the per unit calculation. Therefore $V_S = 1$ p.u. and hence (5.3) is rearranged as

$$|V_C|^2 = |V_C|\,cos(\theta_C) + Q_2\omega L_2 + j(P_2\omega L_2 - |V_C|\,sin\,\theta_C) \tag{5.4}$$

As in (5.4), the left side of the equation is a positive real number. Hence, the imaginary part of the right side of (5.4) needs to be zero. Therefore, the remaining parts of (5.4) form a quadratic equation with respect to $|V_C|$. As the amplitude of the filter bus voltage is a real number, to ensure that there is a valid solution for $|V_C|$ in the quadratic equation, the discriminant of the quadratic equation needs to be greater or equal to zero. Therefore, to ensure a stable voltage and power flow, the power operating points have to comply with

$$\begin{cases} sin\,\theta_C = \frac{P_2\omega L_2}{|V_C|} \le 1 \\ Q_2 + \frac{1}{4\omega L_2} - \frac{P_2^2\omega L_2}{4|V_C|^2} \ge 0 \end{cases} \tag{5.5}$$

As seen in Fig. 5.1, $L_2$ is the combination of the transformer and grid impedances. Based on (2.2), the per unit term of $\omega L_2$ is then approximated as

$$L_2 \approx \frac{1}{SCR} + \omega L_{tx} \tag{5.6}$$

By considering (5.5) and (5.6), the operating point criteria for ensuring stable operation can be rewritten as

$$\begin{cases} |V_C| \geq P_2(\frac{1}{SCR} + \omega L_{tx}) \\ Q_2 \geq \frac{P_2^2}{4|V_C|^2}\left(\frac{1}{SCR} + \omega L_{tx}\right) - \frac{1}{4(\frac{1}{SCR}+\omega L_{tx})} \end{cases} \tag{5.7}$$

As resistances are assumed to be negligible, the real and reactive power transferred to the grid can be written as

$$\begin{cases} P_2 = P_1 \\ Q_2 = Q_1 + Q_C \end{cases} \tag{5.8}$$

Therefore, by substituting (5.8) into (5.7), the minimum voltage magnitude and reactive power required to deliver $P_1$ from the converter are then set by

$$\begin{cases} |V_C| \geq P_1(\frac{1}{SCR} + \omega L_{tx}) \\ Q_1 \geq \frac{P_1^2}{4|V_C|^2}\left(\frac{1}{SCR} + \omega L_{tx}\right) - \frac{1}{4\left(\frac{1}{SCR}+\omega L_{tx}\right)} - Q_C \end{cases} \tag{5.9}$$

From (5.9), it can be concluded that under weak grid conditions, higher capacitor voltage and converter capacitive reactive power are needed in order to deliver a large amount of active power. If a larger filter capacitor is used, the minimum required reactive power from the converter is reduced for delivering higher active power to the grid.

Therefore, according to (5.9), to enable the converter to deliver the required active power the required voltage magnitude (i.e.$|V_C|$) must be maintained. Thus, a converter reactive power/voltage droop control is employed with the droop equation as

$$Q_1 = k_{rec1}(V_{ref} - |V_C|) \tag{5.10}$$

The droop control of AC voltage/reactive power presented in (5.10) is implemented as

$$i_q = -k_{rec}(V_{ref} - |V_C|) \tag{5.11}$$

The q-axis current droop gain (i.e. $k_{rec}$) in (5.11) has to be large enough so that the reactive power complies with (5.9). However, selecting a large $k_{rec}$ might cause a poor damping in the system, and therefore, a lead-lag regulator is utilised to provide the reference for the q-axis current as shown in Fig. 5.3.

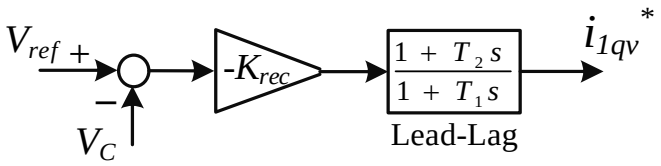


Fig. 5.3. The block diagram of the reactive power/AC voltage Droop control

The operating point for the small signal analysis of the system shown in Fig. 5.1 can be obtained by combining (5.4) and (5.11), and using the grid voltage (i.e. $V_S$) and required active power (i.e. $P_1$).

The system in Fig. 5.1 is tested for the worst case scenario in which the grid is assumed to be very weak (i.e. SCR=1), and the VSC is controlled by the classical vector control as shown in Fig. 4.2. The power ramp test as shown in Fig. 5.4 is used to demonstrate the performance of the system under weak grid condition, and the system control parameters are set as shown in Table 5.1. Fig. 5.4 shows the simulation results for the AC voltage, active power and reactive power when the VSC ramps its active power output with the rate of 5 p.u./s. The solid blue and dotted red lines depict the results with and without the AC voltage compensation (reactive power droop), respectively. The dotted red lines show that as the active power of VSC increases to around 0.6 p.u., the system becomes unstable. The P-V curve of the converter connected to the grid with different SCRs are shown in Fig. 5.5 when the reactive power flow to/from the grid is considered zero. As seen in Fig. 5.5, the ability of system to transfer power is decreased as the system strength decreased.

The solid blue line in Fig. 5.4 shows that the system becomes unstable around 0.7 p.u despite the incorporation of reactive power compensation to the conventional vector current control (Fig 4.2). This shows that the instability that occurs when a VSC is integrated into weak grid is not only because of the lack of enough reactive power, but also the small signal problems that are caused by the interaction of different elements of the system under weak grid conditions. This means that the overall damping in the system is not enough to ensure the system stability under weak grid conditions, hence to overcome to this problem, a virtual impedance based voltage oscilation damping method is proposed in the following section.

Table 5.1. System parameters for illustration

| Parameter | Value |
|---|---|
| Rated voltage at converter side of the transformer | 690 V |
| Rated voltage at the grid side of the transformer | 33 kV |
| Rated frequency | 50 Hz |
| Rated power | 60 MW |
| Transformer leakage impedance $L_{tx}$ | 0.1 p.u. |
| SCR | 1.0 |
| Grid X/R ratio | 4 |
| VSC reactor impedance (50 Hz) | (0.001+j0.2) p.u. |
| Filter capacitance (50 Hz) | 0.10 p.u. |
| Current loops nature frequency | 50 Hz |
| Current loops damping coefficient | 1.414 |
| PLL proportional gain $K_{p\theta}$ | 125 |
| PLL integral gain $K_{i\theta}$ | 3947 |
| Reactive power droop gain $K_v$ | 8 |
| Reactive droop lead-lag time constant (nominator) $T_2$ | 0.002 s |
| Reactive droop lead-lag time constant (denominator) $T_1$ | 0.01 s |

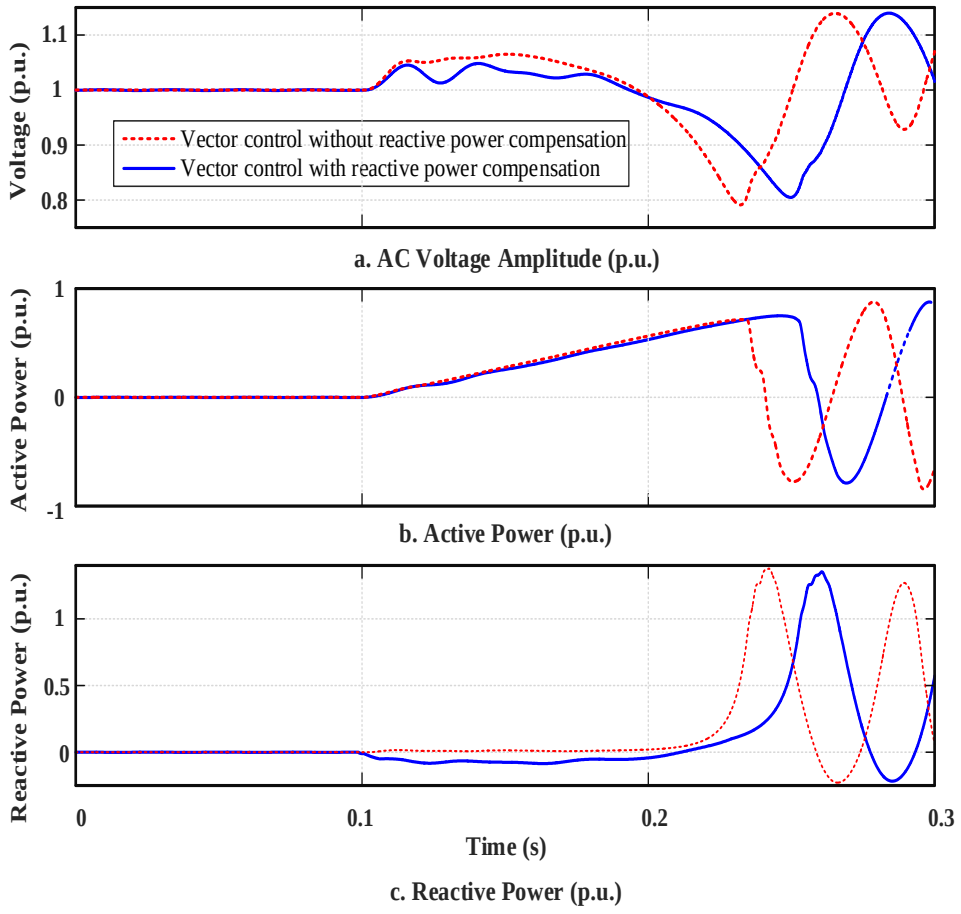


Fig. 5.4. Power ramp of the converter

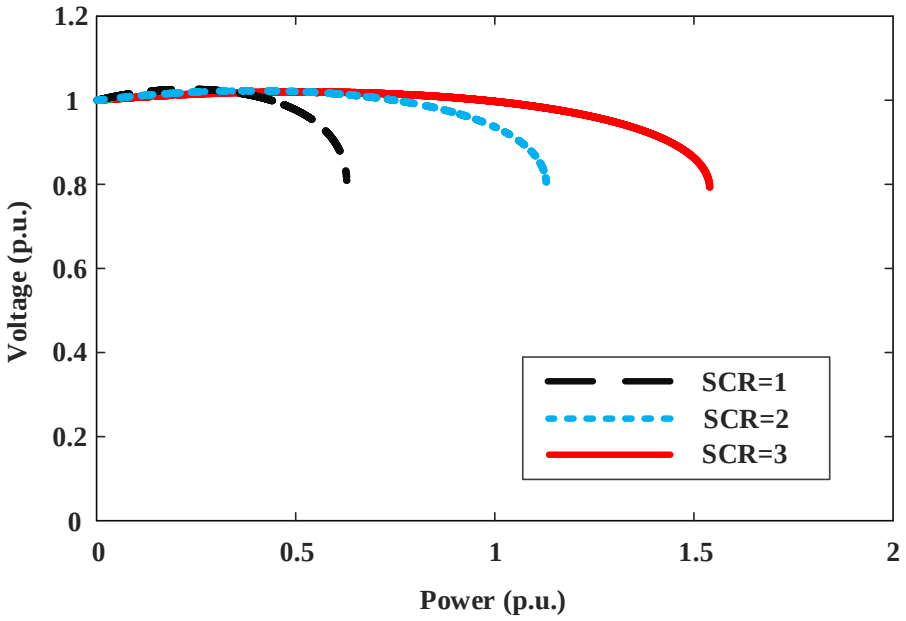


Fig. 5.5. P-V curve of converter connected to grid with different SCRs

### 5.1.2. Principles of the Proposed Virtual Impedance Control for Voltage Stabilisation

In this section, a method based on virtual impedance is proposed to stabilise the local voltage under different operational conditions and to improve the small signal stability of the system voltage.

The proposed virtual impedance control method is based on the fact that utilisation of a shunt resistance ($R_D$) with the filter capacitor as shown in Fig. 5.6 can improve system damping and small signal stability. A power ramp test is conducted for a VSC connected to a very weak grid (i.e. SCR=1) with a shunt $R_D$ of 0.08 p.u. shown in Fig. 5.6. The voltage magnitude of the filter capacitor and the transferred active power from the VSC are shown in Fig. 5.7 (a) and (b), respectively. The active power ramps up at a rate of 2 p.u./s at t=0.1 s and as seen in Fig. 5.7, the local voltage ($V_C$) is stabilised even when the active power is raised to 1.0 p.u.. In other words, the presence of physical resistance ($R_D$) helps to damp the oscillations in the system. However, the resistance consumes energy and is not practical in real systems.

The equivalent circuit of the system shown in Fig. 5.6 in the SRF is illustrated in Fig. 5.8. The voltage equation at the filter capacitor in the SRF is defined as

$$\boldsymbol{V_{C_{dq}}} = \boldsymbol{V_{S_{dq}}} - L_2 \frac{d\boldsymbol{I_{2_{dq}}}}{dt} - j\omega L_2 \boldsymbol{I_{2_{dq}}} - \boldsymbol{I_{2_{dq}}} R_2 \tag{5.12}$$

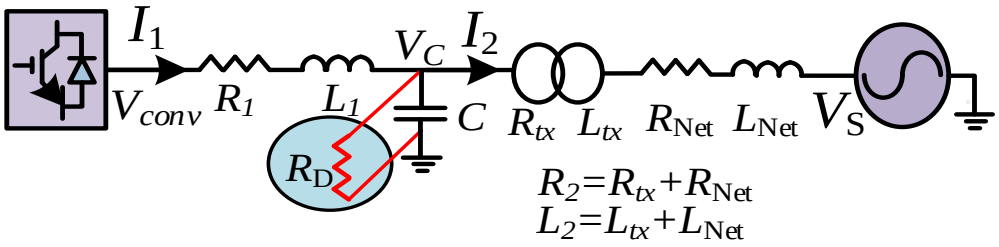


Fig. 5.6. Schematic of circuit with physical damping resistance

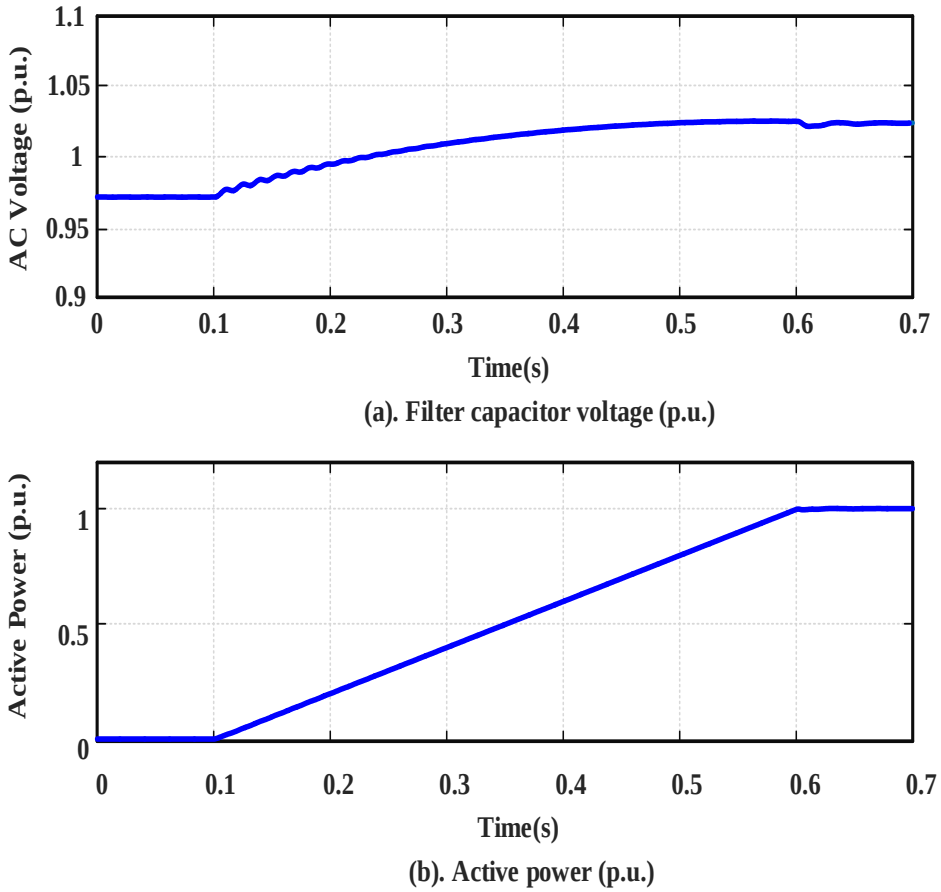


Fig. 5.7. Power ramp test and capacitor voltage with physical damping resistance

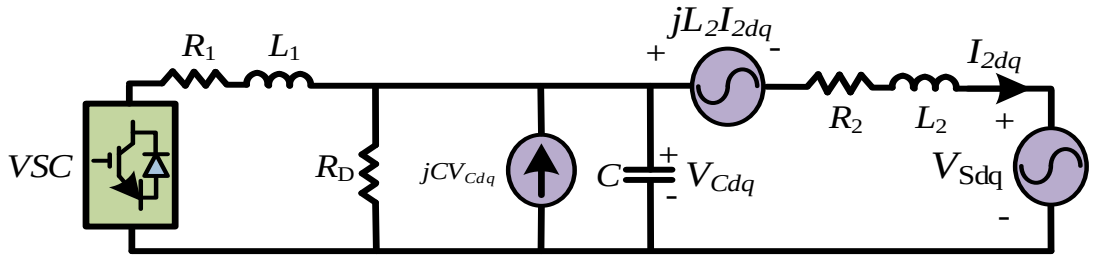


Fig. 5.8. Equivalent circuit of the system in the SRF with physical resistance $R_D$

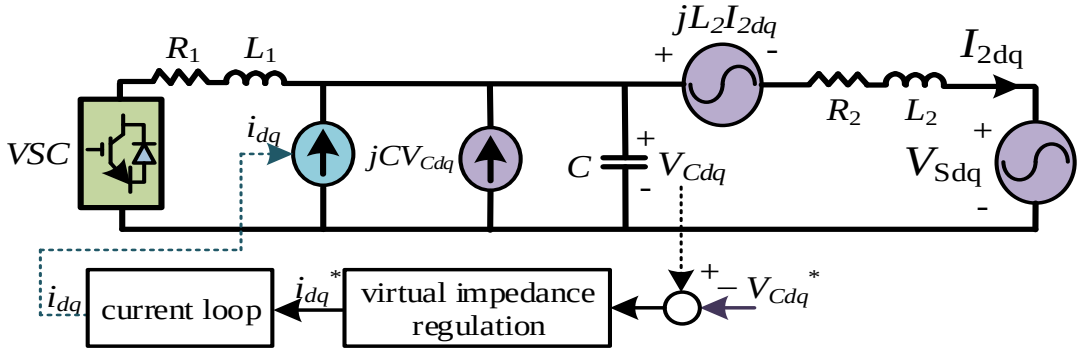


Fig. 5.9. Equivalent circuit of the system in dq frame with virtual impedance

To mimic the effect of the physical resistor, a virtual impedance control is introduced to the system as shown in Fig. 5.9 where an extra control loop is used to provide adequate d- and q-axis damping current. The virtual resistant is modelled to emulate the small signal behaviour of the physical shunt resistance ($R_D$) to damp the oscillations of the system and avoid energy losses in the system, and hence maintain the efficiency of the system [127]. The virtual resistance control can be designed as a closed loop voltage regulation as shown in Fig. 5.10 (a) and the virtual resistance gain (i.e. $K_{pdq}$) is set as

$$K_{p_{dq}} = \frac{1}{R_{D_{dq}}} \tag{5.13}$$

A high-pass filter is used to eliminate the DC offset in the d- and q-axis voltages and therefore eliminate the average power flow of the virtual resistance as shown in Fig. 5.10 (b). Considering the open-loop transfer function of the controller shown in Fig. 5.10 (b), there is

$$\frac{\Delta I_{dq}^{*}}{\Delta V_{C_{dq}}} = \frac{K_{p_{dq}} T_{h_{dq}} s}{1 + T_{h_{dq}} s} \tag{5.14}$$

Rearranging (5.14) and taking into account Ohm's Law gives the virtual impedance as

$$Z_V = \frac{1}{K_{p_{dq}}} + \frac{1}{K_{p_{dq}} T_{h_{dq}} s} \tag{5.15}$$

Equation (5.15) shows that the controller shown in Fig. 5.10 (b) is effectively a series connected RC circuit with the equivalent resistance of $\frac{1}{K_{p_{dq}}}$, and capacitance of $K_{p_{dq}} T_{h_{dq}}$.

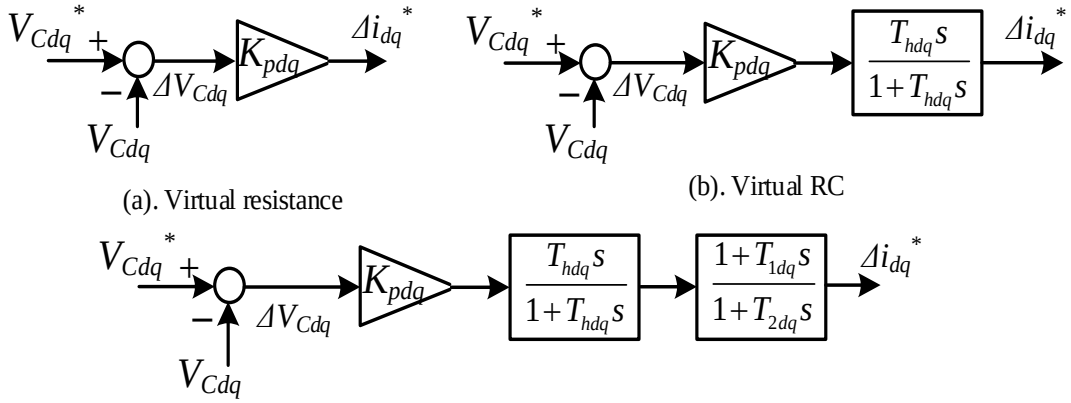


Fig. 5.10. Block diagrams of virtual impedance control

The virtual impedance is different from the actual impedance due to delays in the control loops, and a large gain ($K_{pdq}$) in the virtual impedance could also result in reduced phase and gain margins in the system leading to potential instability. Thus, a lead-lag regulator is again added as shown in Fig. 5.10 (c). Considering the low pass behaviour of the lead-lag regulator in the low-frequency region the transfer function of the block diagram shown in Fig. 5.10 (c) is approximated as

$$\frac{\Delta I_{dq}^*}{\Delta V_{C_{dq}}} = \frac{K_{p_{dq}} T_{h_{dq}} s}{(1+T_{h_{dq}} s)(1+T_{2_{dq}} s)} \tag{5.16}$$

Rearranging (5.16) and taking into account Ohm's Law gives the virtual impedance as

$$Z_V = \frac{1}{K_{p_{dq}} s} + \frac{T_{h_{dq}} + T_{2dq}}{K_{p_{dq}} T_{h_{dq}}} + (T_{h_{dq}} T_{2dq}) s \tag{5.17}$$

Such a system effectively emulates the behaviour of a series connected RLC circuit.

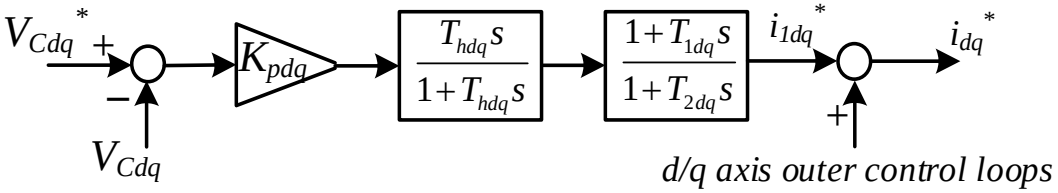


Fig. 5.11. Block diagram of the proposed virtual impedance control

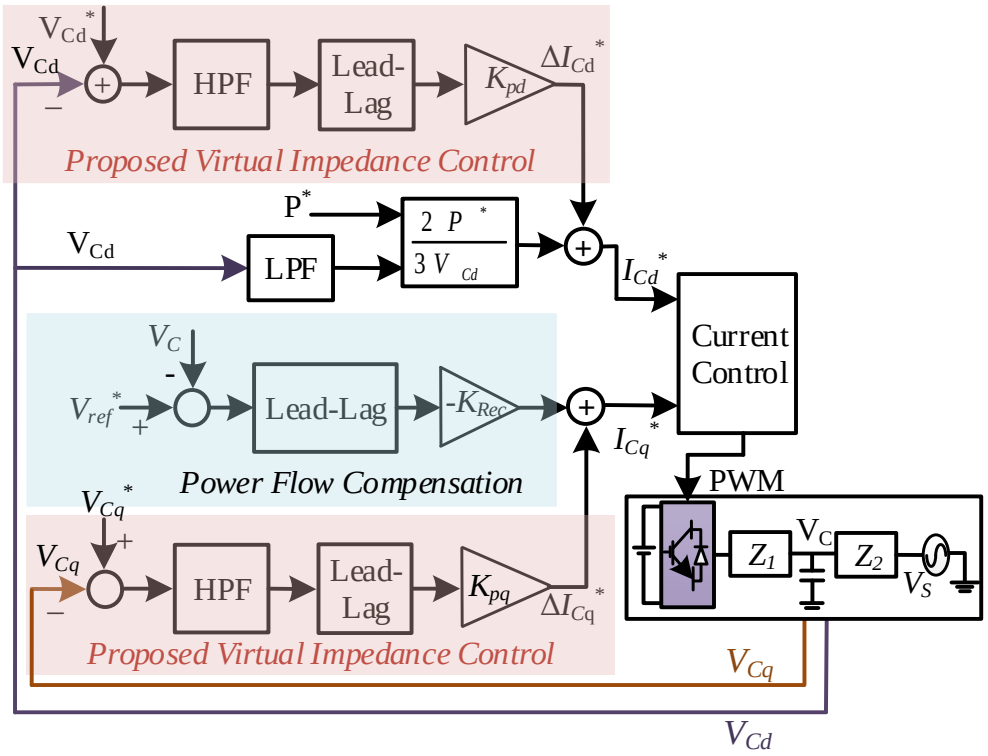


Fig. 5.12. Schematic block diagram of the proposed virtual impedance controller in the overall system

The main aim of the proposed virtual impedance controller for grid-connected VSC is to ensure system stability and full power transfer capability under very weak grid connection without the necessity of active power loss by removal of resistance. Furthermore, as the proposed control method is based on dq reference frame, two different references (for d- and q-axis currents) are available, and hence the virtual impedance parameters can be different for the d- and q-axis, which offers additional

flexibility for the control parameters configuration and tuning. The proposed control method is therefore added to the output of the conventional outer control loop of the converter as shown in Fig. 5.11 and the overall outer loop control block diagram of the VSC is shown in Fig. 5.12.

## 5.2. Analytical Model of the Overall System for Dynamic Analysis

In this section, the small-signal behaviour of the proposed virtual impedance based stabilisation controller is studied using the MIMO frequency domain model of the grid connected VSC developed in Chapter 3. The frequency domain studies are carried out using root locus for the conventional control method considering the outer loops (as discussed in Chapter 3) and the proposed controller.

The state-space model of the system shown in Fig. 5.1 was previously developed and presented in Chapter 3. The overall schematic block diagram of the system including the proposed virtual impedance based stabiliser is shown in Fig. 5.13. The system parameters used for the small-signal analysis and the parameters for the virtual impedance controller are presented in Table 5.2 and Table 5.3, respectively. The static operating points for the circuit in Fig. 5.1 are calculated using static power flow analysis and taking into account the constraint in (5.9).

The root locus of the closed loop d-axis current of the system shown in Fig. 5.13 when d- and q-axis compensation is not activated is presented in Fig. 5.14. The transferred power to the grid increases from 0.1 p.u. to 1.0 p.u.. As seen in Fig. 5.14, the main poles of the system tend to move to the RHP when the VSC power increases from 0.1 to 1.0 p.u. This means that the system tends to become unstable with large power transfer from VSC to the grid, i.e. for $P_1 \geq 0.7$ p.u. the system becomes unstable, which corresponds well to the time domain simulation shown in Fig. 5.4. This confirms that although the reactive power at the connection is compensated to comply with the power flow requirement, the system still suffers from small signal instability under very weak grid connection.

With the proposed control enabled, as shown in Fig. 5.13 the associated root loci of the d-axis, and q-axis currents for variations in VSC active power are plotted in Fig. 5.15 and Fig. 5.16, respectively. As can be seen, by using the proposed virtual impedance voltage stabiliser, the main poles of the system for transferred power from 0.1 p.u. to 1.0 p.u. for both d- and q- axis currents are pushed to the LHP, indicating improved system stability.

Table 5.2. Model parameters for small-signal analysis

| Parameter | Value |
|---|---|
| SCR | 1 |
| X/R | 4 |
| $V_S$ | 1.0 p.u. |
| VSC reactance ($j\omega L_1$) | j0.2 p.u. |
| Filter capacitor impedance | -j0.1 p.u. |
| $K_{Rec}$ | 12 |
| $V_{Ref}$ | 1.0 p.u. |

Table 5.3. Proposed virtual impedance control parameters

| Control parameter | Value |
|---|---|
| d-axis lead-lag time constant (nominator) $T_{2d}$ | 0.02 s |
| d-axis lead-lag time constant (denominator) $T_{1d}$ | 0.004 s |
| q-axis lead-lag time constant (nominator) $T_{2q}$ | 0.02 s |
| q-axis lead-lag time constant (denominator) $T_{1q}$ | 0.002 s |
| d-axis gain $K_{pd}$ | 12.4 |
| q-axis gain $K_{pq}$ | 6.2 |
| d-axis high-pass filter time constant $T_{hd}$ | 0.002 s |
| q-axis high-pass filter time constant $T_{hq}$ | 0.001 s |

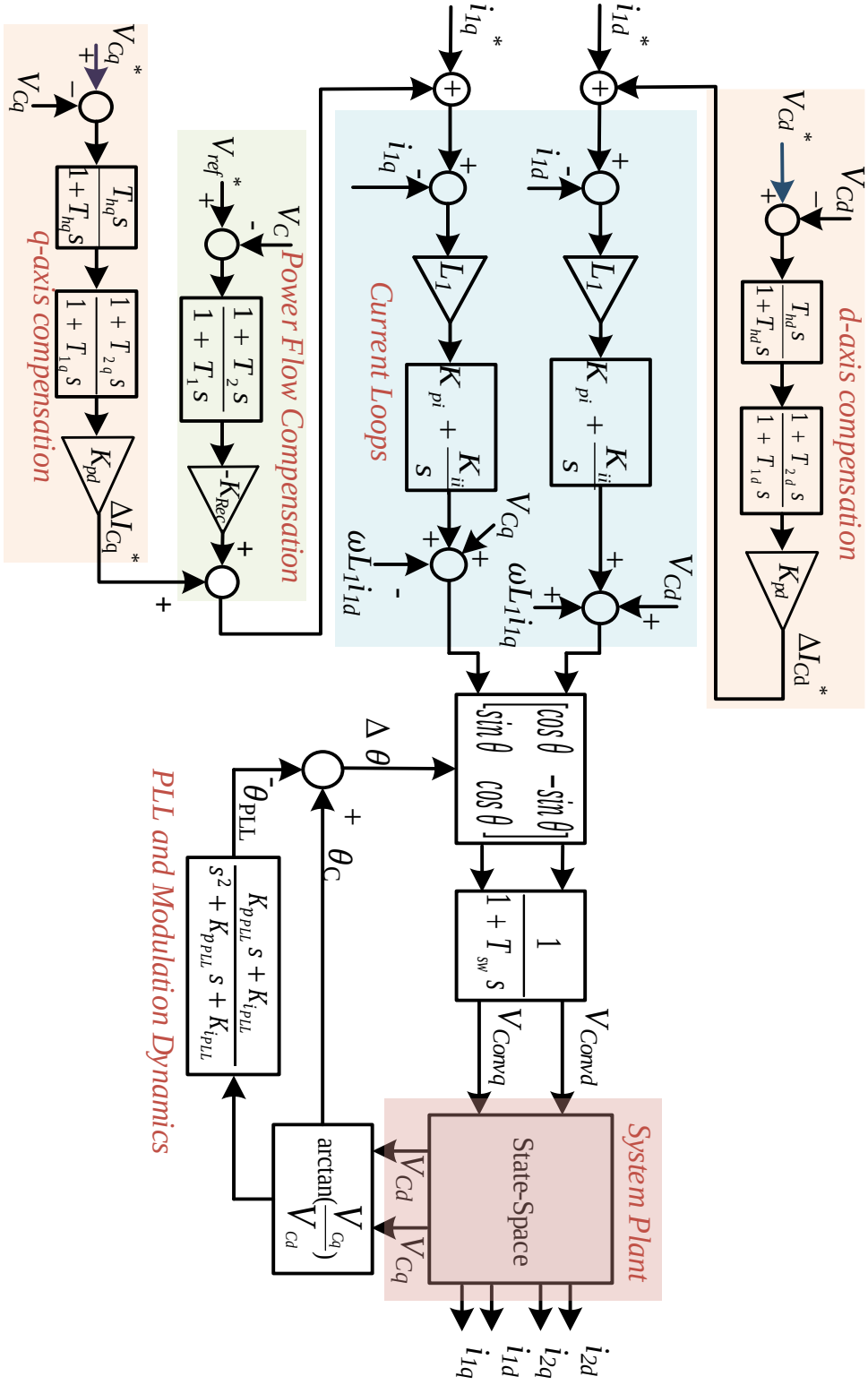


Fig. 5.13 .Block diagram of the MIMO model of the system including the proposed control method

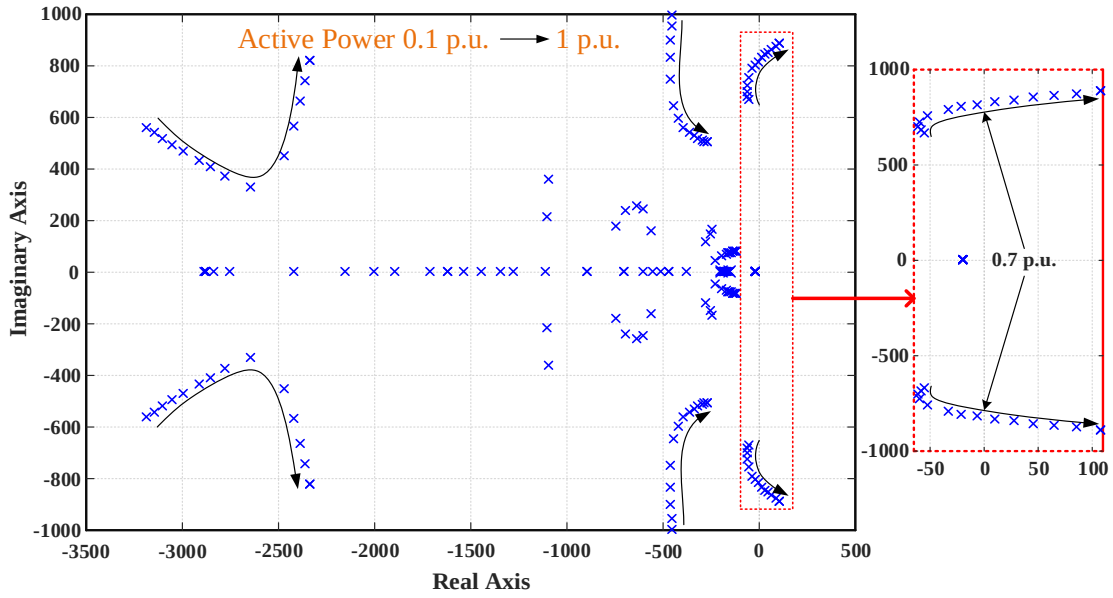


Fig. 5.14. Root locus of the d-axis current without proposed virtual impedance based voltage stabiliser control

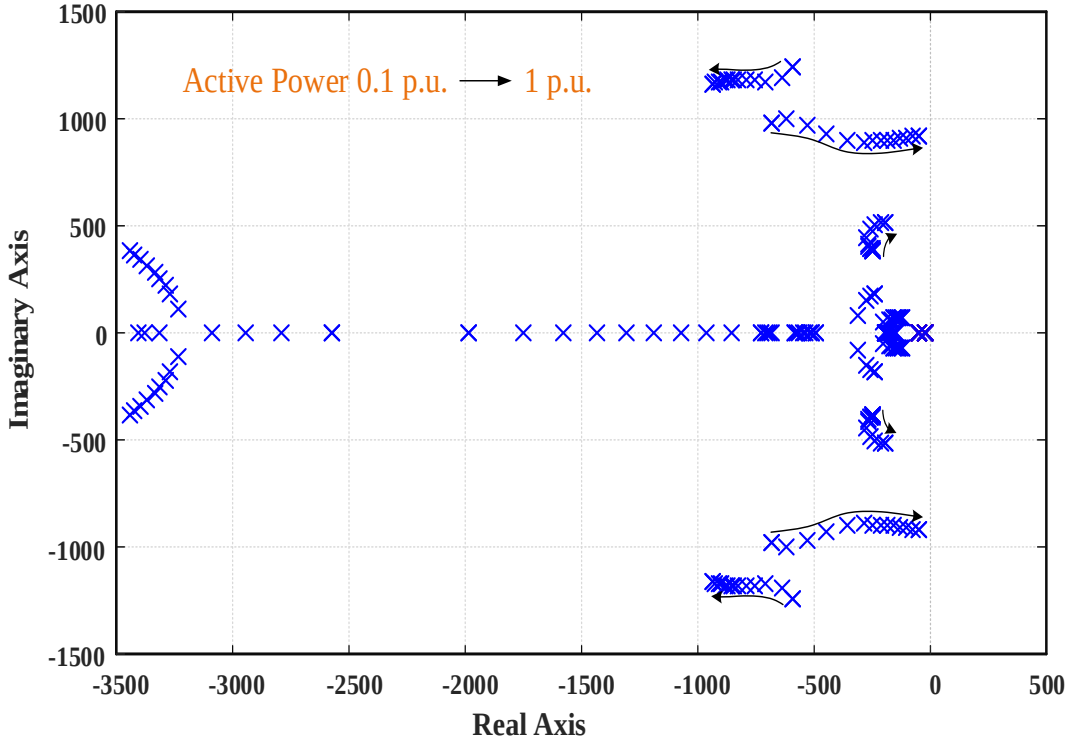


Fig. 5.15. Root locus of the d-axis current with proposed virtual impedance based voltage stabiliser control

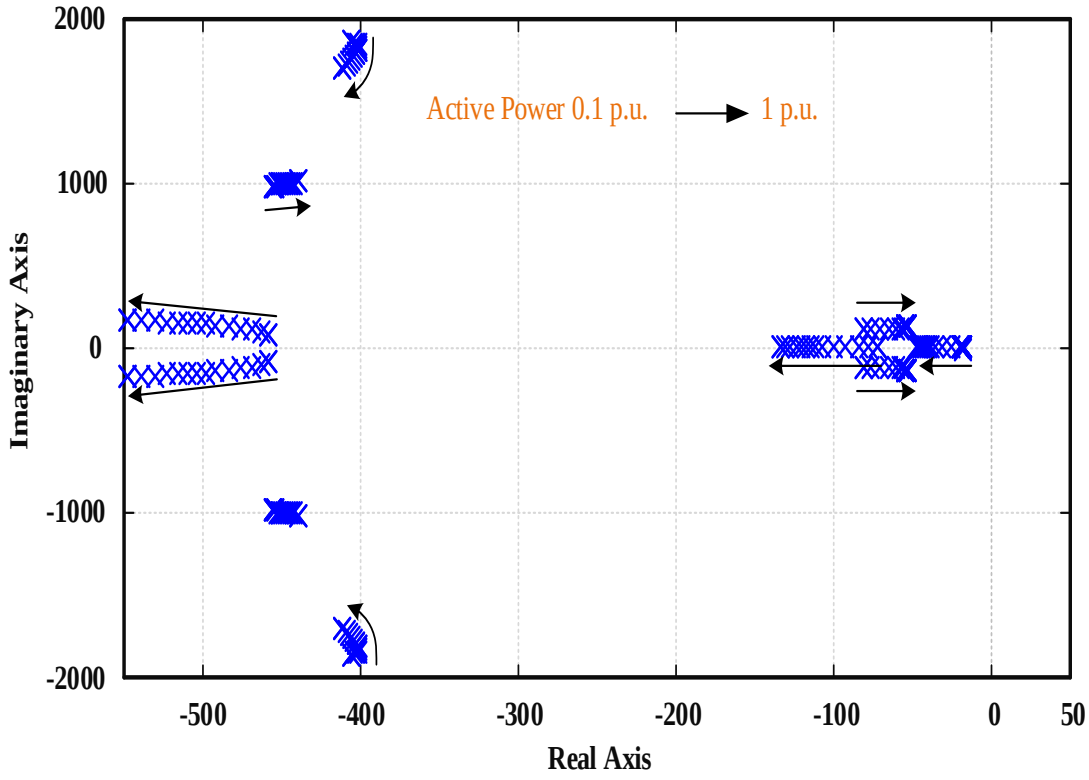


Fig. 5.16. Root locus of the q-axis current with proposed virtual impedance based voltage stabiliser control

For the system shown in Fig. 5.13, the root locus of the d-axis current for different values of $K_{pd}$ with $K_{pq}$ kept at zero is presented in Fig. 5.17 (a). As Fig. 5.17 (a) shows, for $K_{pd} = 0$, the poles of the system are in the RHP. By increasing $K_{pd}$, the poles move to the left, and for all $K_{pd}$ values greater than 26, the system becomes stable.

In Fig. 5.17 (b), the d-axis root locus of the system shown in Fig. 5.13 is presented for different values of $K_{pq}$ and $K_{pd} = 0$. The root locus in Fig. 5.17 (b) shows that the system is stable with $5.5 < K_{pq} < 18.5$.

The results presented in Fig. 5.17 indicate that the virtual impedance gains (i.e. $K_{pd}$ and $K_{pq}$) should be selected differently.

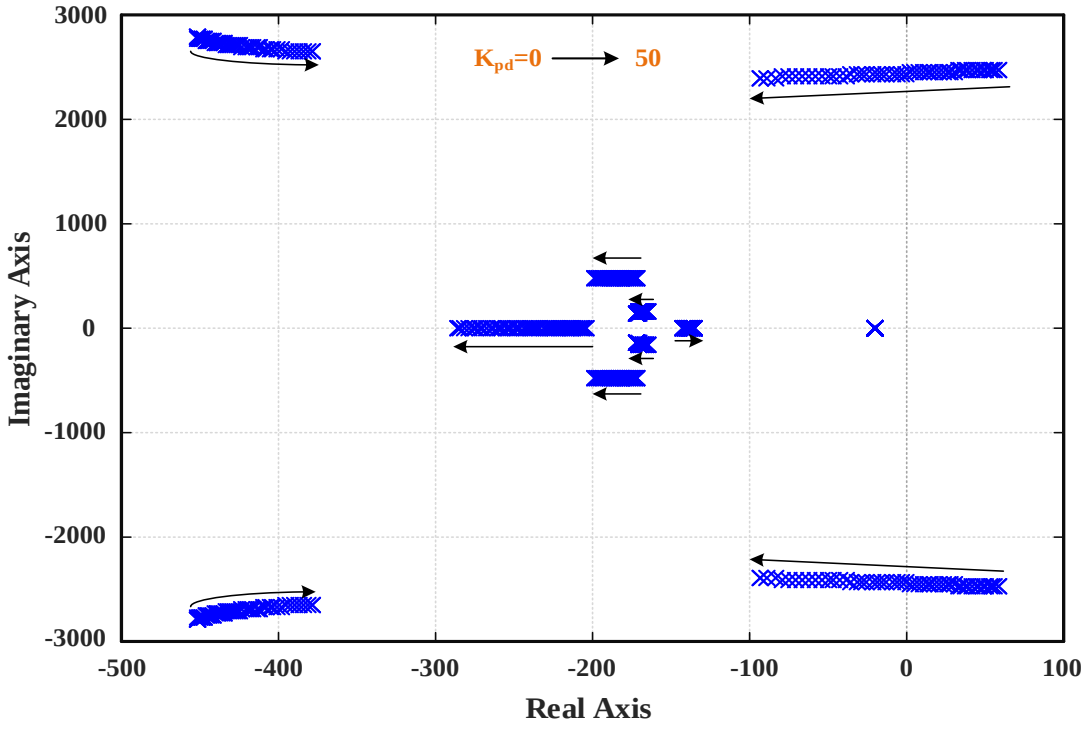


(a) $K_{pd}$ varies and $K_{pq}$=0

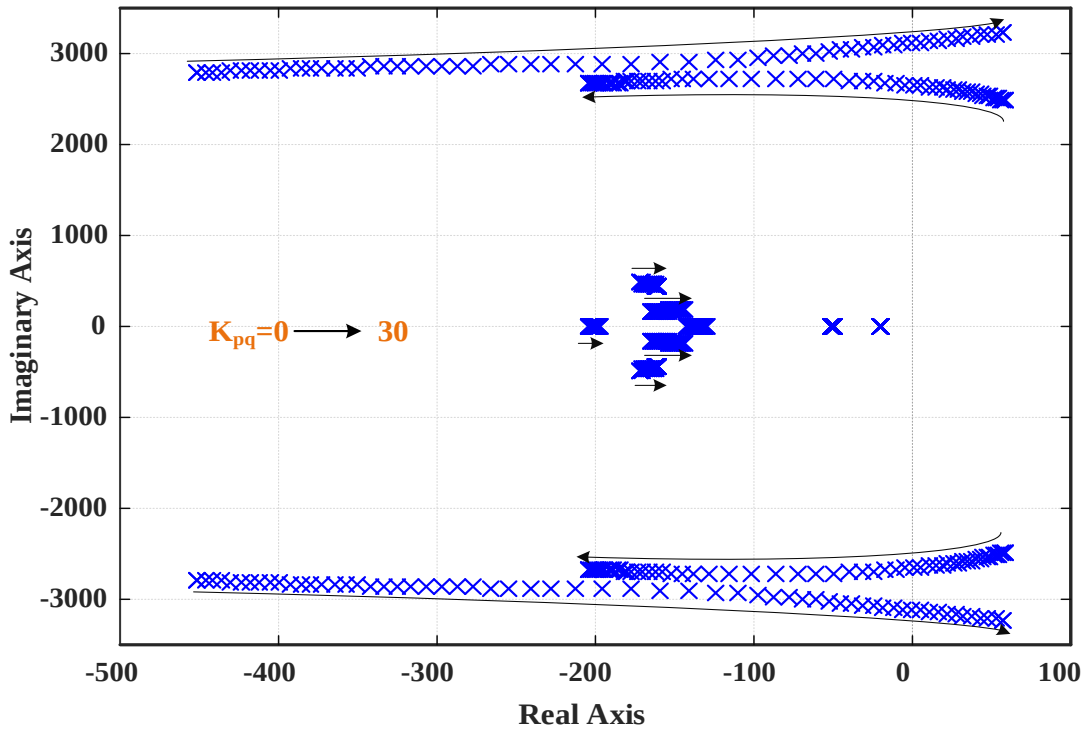


(b) $K_{pq}$ varies and $K_{pd}$=0

Fig. 5.17. Root locus of the d-axis current for d- and q- axis gains of the virtual impedance

## 5.3. Case Studies and Validation of the Proposed Control Method

Case studies of the proposed control method are presented in this section. Power ramp up/down tests are carried out first, and the proposed controller performance during a three-phase fault is then simulated. Different grid strengths have also been considered to test the robustness of the proposed controller. All the simulations are carried out in the sim power system toolbox of Matlab.

### 5.3.1. Power Ramp Test for the Proposed Controller

A power ramp test is carried out for the system configuration shown in Fig. 5.1 in which the VSC is controlled using the proposed virtual impedance stabiliser control. For the simulations, the system parameters are the same as in Table 5.1, and the parameters for the proposed virtual impedance stabiliser control are set as in Table 5.3. The results of the power ramp with the proposed virtual impedance based controller test are shown in Fig. 5.18. It should be mentioned that the results for the case without proposed controller is already presented in Fig. 5.4.

At time t=0, there is no power transfer, and at t=0.1 s, a power ramp is applied to the system with a ramp rate of 6.6 p.u./s. As can be seen in Fig. 5.18, the voltage and current are stable during and after the power ramp. This shows a very significant improvement compared to the power ramp test shown in Fig. 5.4 for the classic vector control.

Furthermore, the power is then ramped down at t=0.45 s to 0 with a ramp rate of -6.6 p.u./s. The results clearly show that the voltage and current are stable across the whole active power range. In the presented results, the terminal voltage drops to 0.974 p.u. at maximum power transfer, in which the q-axis current is around -0.22 p.u. As the q-axis current droop gain ($k_{rec}$) is set at 8, the results correspond well with those predicted by (5.11).

The results presented in Fig. 5.18 clearly show that the proposed virtual impedance based voltage stabiliser control method enables the VSC to transfer full power into a very weak point of the grid.

### 5.3.2. Transient Test for Proposed Controller

A 3-phase fault test is carried out in this section for the same system configuration and control parameters used in Section 5.3.1. The simulation results for the 3-phase short circuit fault as shown in Fig. 5.19 are presented in Fig. 5.20.

In Fig. 5.20, the VSC initially transfers full power to the grid. At t=0.1 s, a 3-phase solid short circuit happens at the grid integration point as shown in Fig. 5.19. As seen in Fig. 5.20, the capacitor bus voltage (converter side of the transformer) drops to 0.1 p.u. immediately after the fault occurs.

When the fault occurs, the current rises to 1.2 p.u. for a few milliseconds and then drops to around 0.5 p.u. due to the VDCL as previously described in Chapter 4, and stays at that level until fault clearance. Finally, the fault is cleared in t=0.18 s, and the VSC resumes delivery of full power (i.e. 1 p.u.) to the grid according to the VDCL. The proposed control method requires no control mode switching during large transients as the current control loop is retained by the controller.

### 5.3.3. Test for Different Grid Strengths

In this section, the proposed controller is tested with power ramps and three-phase faults for different grid strengths i.e. SCR=2 (relatively weak grid) and SCR=10 (solid connection). In the simulation, the same system configuration and controller parameters are used as in Section 5.3.1 and the simulation results are presented in Fig. 5.21. The effectiveness of the controller is tested during different operating conditions as the grid strength might change in different operational situations.

In Fig. 5.21, the system was initially started from zero power, and a power ramp test at a rate of 6.66 p.u./s is applied to the system. During the process of the ramp up for

both cases (SCR=2 and SCR=10), the voltage stayed approximately at 1 p.u. A three-phase short circuit is then applied at the grid integration point as shown in Fig. 5.19. For both cases the voltage drops to approximately 0.1 p.u. After the fault clearance, the voltage recovers smoothly, and the active current also returns to 1 p.u.. Therefore, the results confirm the effectiveness of the proposed virtual impedance voltage stabiliser with different grid strengths which means that the controller does not need to be re-tuned in the case that the grid strength changes.

Furthermore, the root locus of the d-axis current with the proposed virtual impedance based voltage stabiliser control for different SCR values and active power of 1.0 p.u. is shown in Fig. 5.22. It can be seen that without any change in the system configuration and control parameters, the system is stable for all the SCR values.

The results of the case studies presented in this section demonstrate that the proposed control method ensures the converter delivers full power in steady state. The system can also ride-through severe transients due to the presence of the current control loop. It offers flexibility for operation in different operating conditions and grid strengths without the requirement of re-tuning the parameters.

## 5.4. Grid Stabiliser for Weak Grid Integration of VSC

So far, the proposed virtual impedance based voltage stabiliser of Fig. 5.12 is used as an embedded component of the controller of the wind turbine grid side VSC. In this section, the proposed control method in Fig. 5.12, is used as an external stabiliser for VSC interfaced generation (e.g. a wind farm) connected to a very weak grid. This means that the wind turbine grid interfaced converter controller can use conventional vector current control, whereas an external device is utilised in order to provide damping and stabilisation to the system.

The external stabiliser may be desirable in some situations. For example, a wind farm may use turbines from more than one manufacturers, or two large wind farms may be integrated into a very weak point of the grid, and thus the grid owner may be

responsible for ensuring the stability of the grid. Thus, an external stabiliser based on the virtual impedance voltage stabiliser can bring extra flexibility for the grid operator.

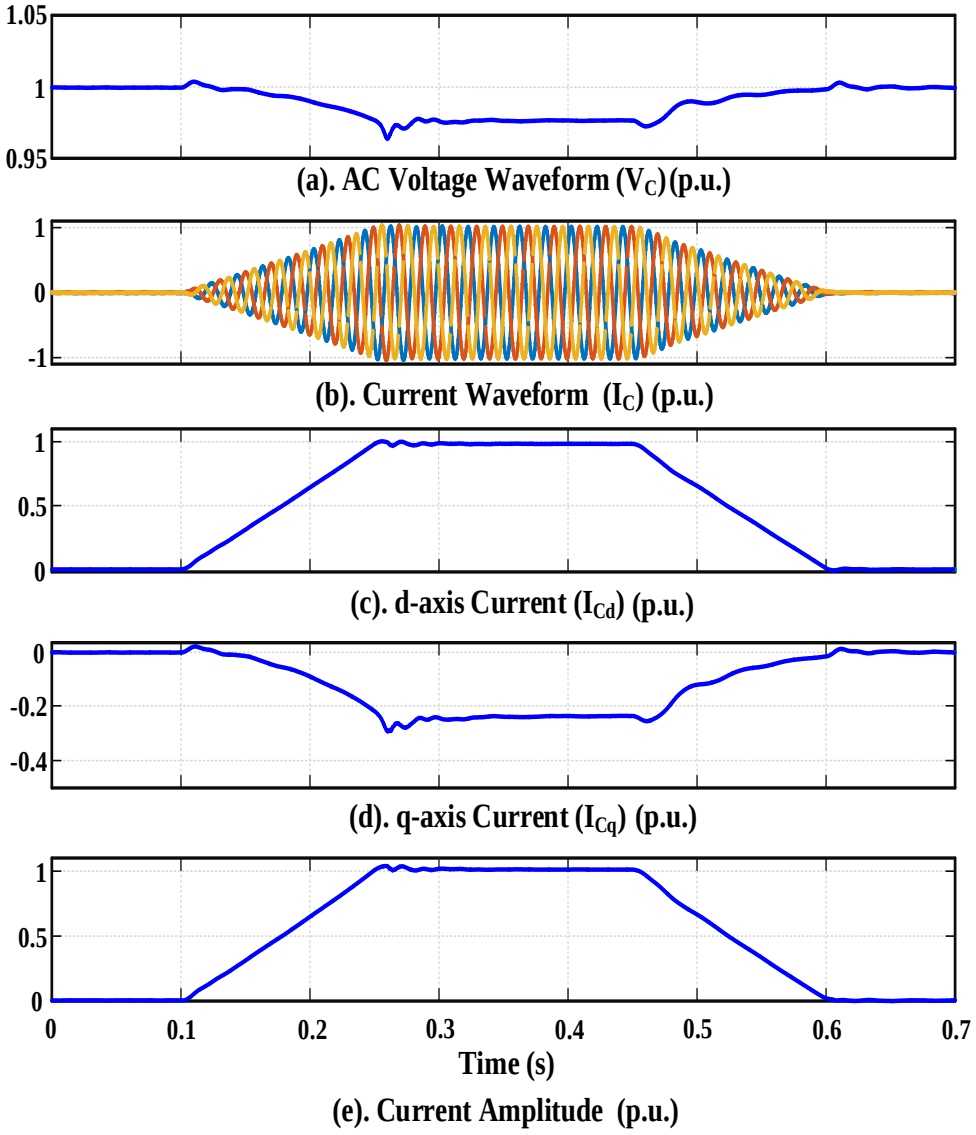


Fig. 5.18. Power ramp test with the virtual impedance voltage stabiliser control embedded into the VSC control

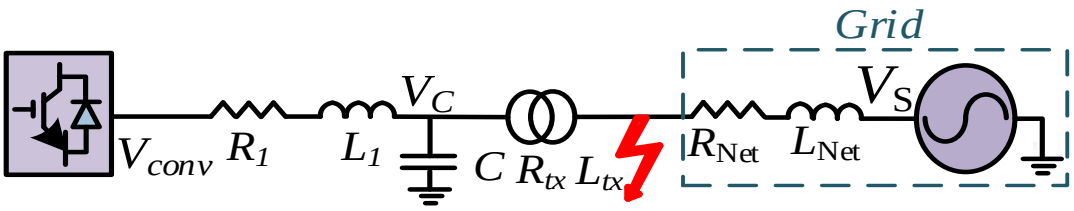


Fig. 5.19. The system configuration with fault location

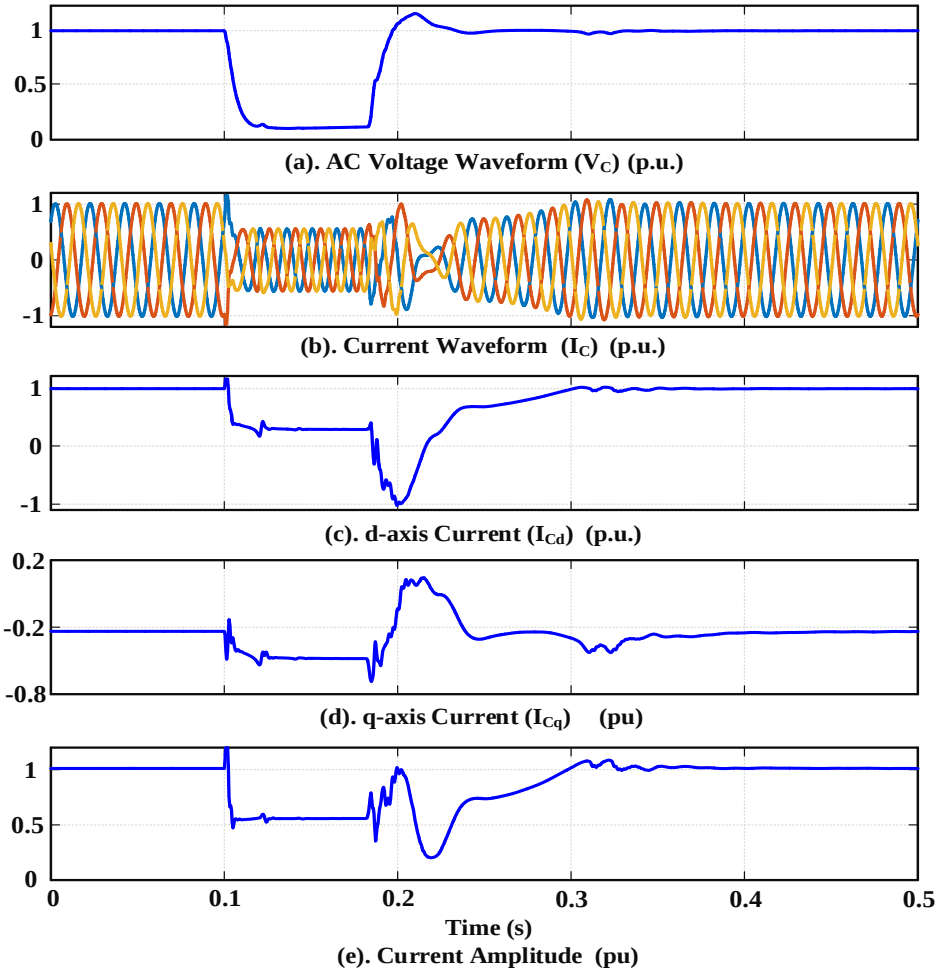


Fig. 5.20. Transient performance with virtual impedance stabiliser control

The same control method as shown in Fig. 5.12 is therefore employed for controlling the external stabiliser and the system layout is shown in Fig. 5.23. As seen in Fig. 5.23, an energy storage system is connected to the eternal VSC stabiliser. For wind farms located offshore or in a rural area, the external stabiliser may have to be located away from the wind farm PCC point, resulting in a substantial impedance ($Z_L$) between the PCC and the stabiliser as shown in Fig. 5.23.

The proposed system configuration in Fig. 5.23, when the stabiliser is located at the PCC ($Z_L$=0), has been tested first for a power ramp up/down (6.6 p.u./s) with the same test scenario as Section 5.3.1 and the simulation results are presented in Fig. 5.24. The parameters for the test system are the same as given in Table 5.1, and the parameters for the stabiliser virtual impedance controller are the same as those in Table 5.3, except $K_{pd}$ and $K_{pq}$ which are 34 and 17, respectively. As the results presented in Fig. 5.24

illustrate, when the VSC interfaced generation unit is controlled using conventional vector current control, employing the external stabiliser allows VSC to deliver the rated power (i.e. 1 p.u.). The stabiliser current stays low during both the steady-state and dynamic processes, which means that the stabiliser in the proposed configuration only provides small signal compensation to the system (due to the presence of the high pass filter in the virtual impedance based voltage stabiliser). As seen in Fig. 5.24, the power variation in the stabiliser during the power variation in the main VSC interfaced generation is very small (i.e. less than 0.05 p.u. based on 6.6 p.u./s power ramp). The energy flow from the stabiliser to the grid shown in Fig. 5.24 indicates that only a relatively low amount of energy is required. This means that only very small energy storage and conversion systems are required in order to stabilise a very large wind farm.

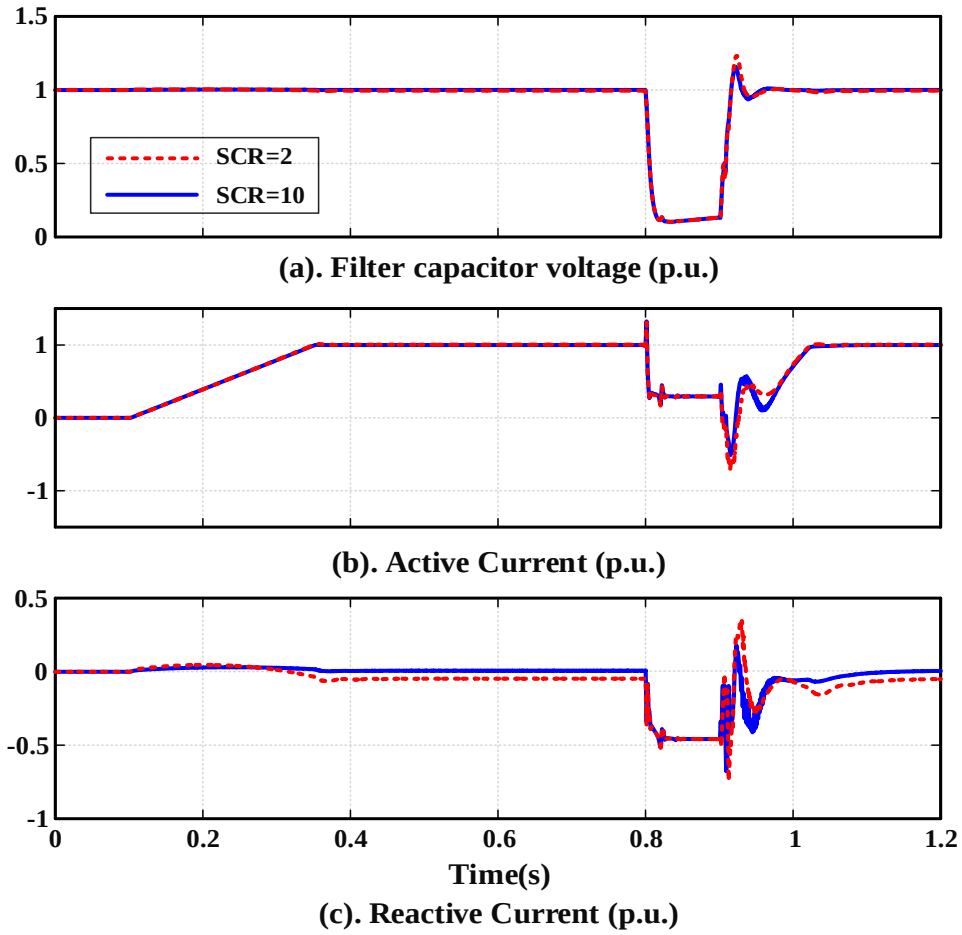


Fig. 5.21. Power ramp test and transient performance with the proposed virtual impedance stabiliser control for relatively weak and strong grids

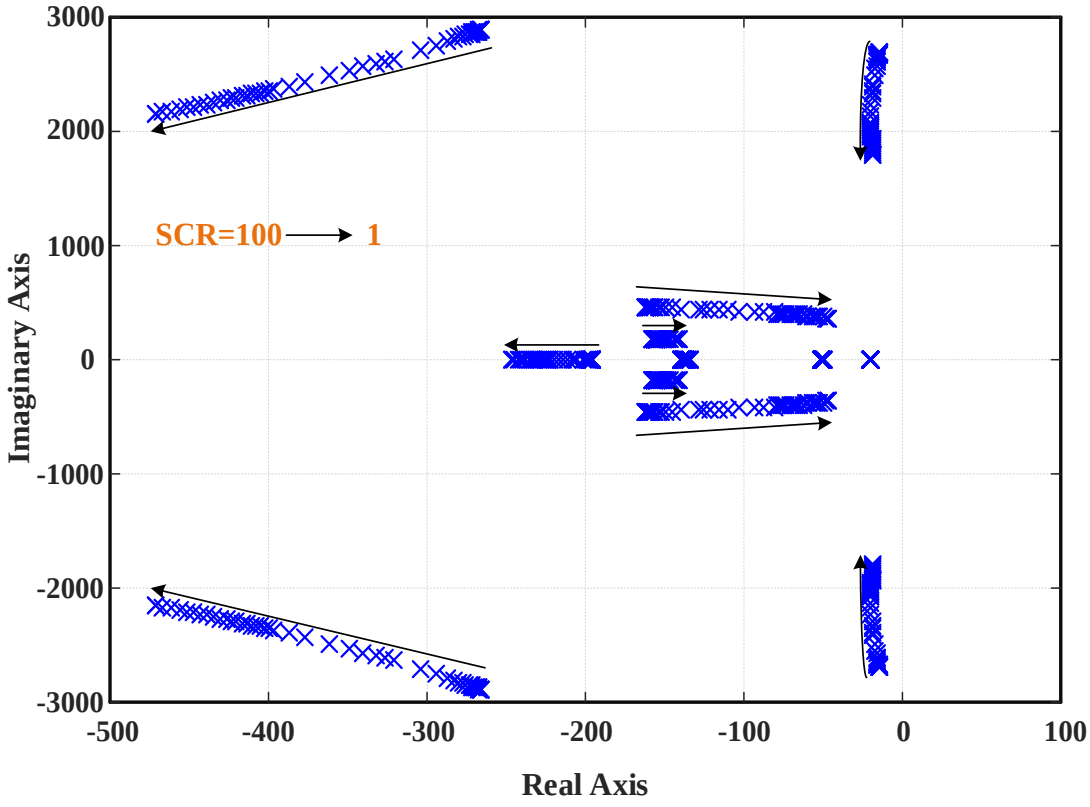


Fig. 5.22. Root locus of the d-axis current with proposed virtual impedance based voltage stabiliser control

The proposed stabiliser is further tested for three different distances between the PCC and the stabiliser, i.e. 1 km, 20 km and 50 km. The impedances between the PCC and stabiliser are calculated using the cable parameters shown in Table 5.4.

Power ramp up/down tests similar to Fig. 5.24 with SCR=1 are performed for different impedances (i.e. line lengths) between the PCC and stabiliser, and the results are presented in Fig. 5.25. All the system and control parameters are the same as those for Fig. 5.24, except $K_{pd}$ and $K_{pq}$ that are presented in Table 5.5. The parameter values in Table 5.5 are chosen to have the best time domain simulation results.

As seen in Fig. 5.25, using the proposed configuration, the VSC is capable of transferring 1 p.u. power to the grid when SCR=1. The stabiliser's current for different cases also stays low during both steady-state and dynamic process. As seen in Fig. 5.25, as the impedance between the PCC and the external stabiliser increases, the current and active power of the stabiliser increase and the voltage at the stabiliser

terminal decreases. Furthermore, the power of the stabilisers in all cases after the transients returns to zero.

The energy flow is calculated for all the different cases in Fig. 5.24 and 5.25 for the ramp up of the active power as shown in Table 5.6. The energy is calculated from the start of the power ramp until the system reaches a new steady state operating point.

As the results in Table 5.6 show, in the ramp up test, energy is injected from the storage system to the grid. It also can be seen from Table 5.6 that the total required energy during the ramp test is increased as $Z_L$ increases.

Therefore, the storage capability of the stabiliser needs to be sized according to $Z_L$. For example, if the distance between PCC and the external stabiliser is 50 km and the DC link voltage of the storage converter is 1.3 kV, for a storage capacitor of 767.5 mF, the DC link voltage is reduced by 24.6% during the power ramp up.

Table 5.4. Cable parameters

| Cable parameter | Impedance |
|---|---|
| Inductance | 0.31 mH/km |
| Resistance | 0.012 Ω/km |
| Capacitance | 0.38 μF/km |

Table 5.5. External stabiliser parameters for different impedances

| Line length | $K_{pd}$ | $K_{pq}$ |
|---|---|---|
| 1 km | 36 | 18 |
| 20 km | 40 | 20 |
| 50 km | 44 | 22 |

Table 5.6. Required energy from the storage unit for different impedances

| Line length | Energy from storage (kJ) (Ramp up) |
|---|---|
| No line (0 km) | 47.88 |
| 1 km | 54.53 |
| 20 km | 113.46 |
| 50 km | 216.19 |

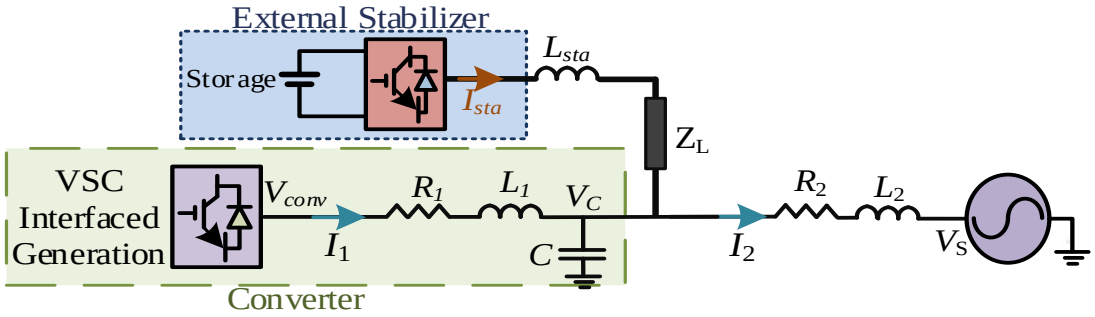


Fig. 5.23. System Schematic including external stabiliser

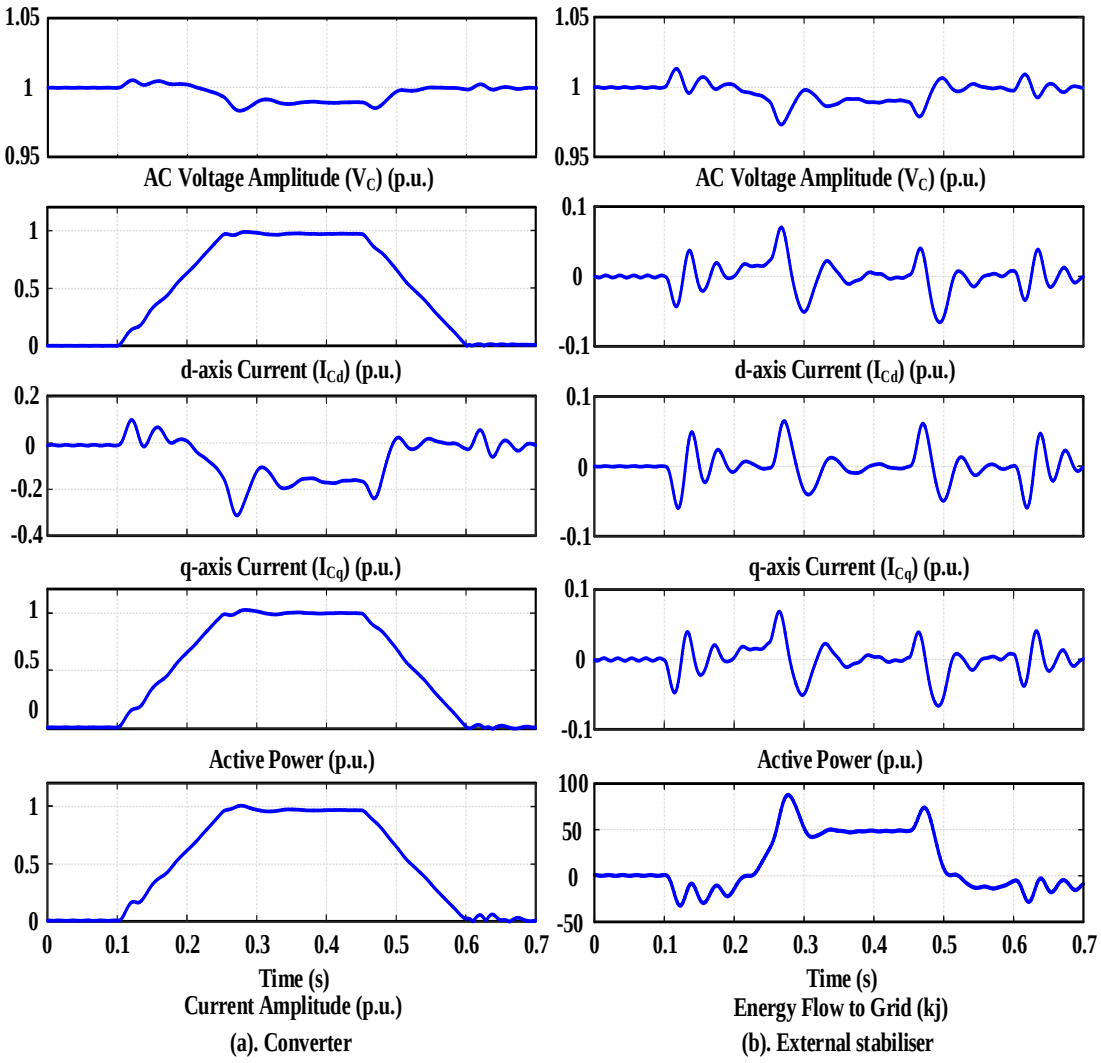


Fig. 5.24. External stabiliser for weak grid stabilisation

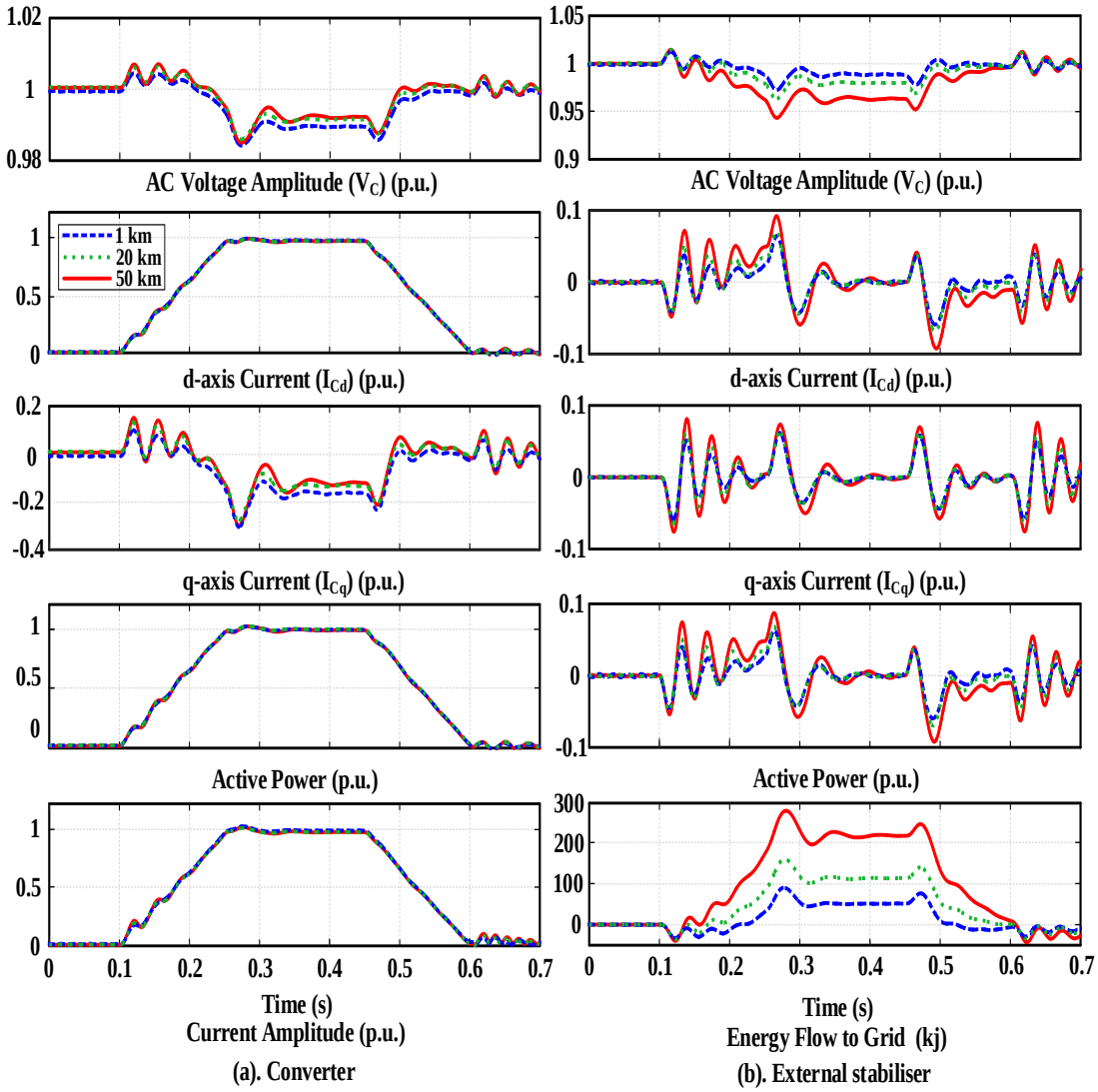


Fig. 5.25. The external stabiliser for weak grid with impedance between the converter and stabiliser

## 5.5. Summary

When VSC interfaced generation is integrated into a very weak point, the system can become unstable due to the reactive power flow and voltage small signal stability issues. To ensure stable operation of the system, reactive power compensation and small signal voltage stability need to be considered.

In this chapter, a virtual impedance based small signal voltage stabiliser is proposed. In the proposed control method, the conventional current control loop is maintained, and the proposed controller works as a complementary output control loop providing extra damping to the system without any energy/power loss. The proposed control method enables the VSC to deliver full rated power to the weak point of the grid.

Furthermore, the presence of the current loop allows the VSC to deal with large transients without requiring any control mode changes. The proposed controller also offers the possibility to be used with different grid strengths which might change during the VSC operation (e.g. line trips, etc.).

The proposed control method benefits from the fact that it can be used as an external stabiliser for very weak points in the grid by providing extra damping to the system. The rated power of the external stabiliser is very small compared to the overall system rating with real power average of zero.

# 6. Conclusion and Future Work

In this chapter, the conclusion of the thesis is drawn, the thesis contributions are outlined, and potential future work is highlighted.

## 6.1. Conclusions

The primary focus of this thesis is the integration of VSCs to very weak electrical grids. Grid connected VSCs are traditionally controlled by vector current control in which the decoupled SRF (d-q) currents are used to separately control the active and reactive power flow of the converter. This control structure provides fast dynamic response and allows the converter to limit the current during transients. However, when the VSC is connected to a very weak point of the grid, the converter is not able to transfer full power to the grid due to potential system instability. This problem is largely caused by the interaction between PLL dynamics and different parts of controller and system, and voltage instability at the connection point to the grid.

In this thesis, first a MIMO frequency domain model of a single grid connected VSC is developed. In this model, different parts of the system are modelled including the current controller, grid connection network, PWM switching, and PLL dynamics. Three different grid connection networks were modelled including simplified connection, T model of the connection cables, and Pi model of the connection cables. The three models have different complexity and varied frequency response at higher frequency range. As the frequency of interest is in the relatively low range, the simple model is sufficient for the frequency domain studies.

The developed model is then used as a basis for modelling parallel converters in the frequency domain. In the developed model, the d-axis of the SRF is aligned with the grid voltage and hence, all the VSCs are modelled by the same reference frame enabling any number of VSCs to be added to the MIMO model of the parallel VSC system. The studies show that in a multi-converter system, as the strength of the grid decreases, the sensitivity of each VSC to the disturbances in the other converters is increased.

To tackle the instability issue when the grid is very weak, e.g. SCR=1, a current error based controller is proposed as a complementary control in parallel with the conventional vector current control. The current error based controller consists of two different parts. The first part calculates a phase angle based on the error of the d-axis current to adjust the output of the PLL. Furthermore, the q-axis current error is used to calculate an adjustment to VSC output voltage amplitude directly. The proposed error based controller is tested with different scenarios including increasing and decreasing power ramps, three phase fault, and different grid strengths. The simulation results show that using the proposed error based controller the converter is capable of transferring full rated power and to ride-through the fault current with SCR=1 at the connection point to the grid. The results have also shown that the VSC provides stable operation under different conditions (e.g. full power, and fault) with various grid strengths without the need for changing the controller parameters and structure. The simulations also confirm that in a system with multiple VSCs the proposed controller is capable of stabilising the system in a very weak grid and allowing the system to transfer the full power.

The second proposed method to improve the stability of a VSC connected to a weak grid is based on the virtual impedance emulation in the VSC control system. The proposed virtual impedance based stabilising controller also enables the VSC to transfer the full power in the very weak grid condition. This virtual impedance stabilising control works as a supplementary outer control in the d- and q-axis whose inputs to the controller are the d- and q-axis PCC voltage, and where the outputs are added to the d- and q-axis current references. The virtual impedance control consists of a high-pass filter, lead-lag filter, and a gain. This controller stabilises the system by providing extra damping to the system. This proposed controller is also tested with different scenarios including power ramp up/down, three phase fault, and different grid strengths. The simulation results confirm that the VSC controlled by the proposed virtual impedance based stabiliser is capable of transferring 1 p.u. power and of fault ride-through with the very weak connection. The simulation results also show that when the grid strength changes, the converter is operates normally with no changes in the proposed control parameters and structure.

This virtual impedance control method can also be implemented as an external stabiliser which consists of a relatively small converter and an energy store connected to the DC link of the converter. The external converter only needs to provide small transient power for stabilisation and the size of energy store can also be relatively small. Such an external stabiliser may be desirable in different situations, for example if a wind farm is expanding and where the turbines are not made by a single manufacturer, or if two large wind farms are integrated into a very weak point of the grid, and it is therefore the grid owner's responsibility to ensure the stability of the grid. In the context of the wind farms, this means that the controller of the wind turbine grid interfaced converter is kept unchanged whereas an external device is utilised to provide extra damping to the whole system.

## 6.2. Author's Contributions

The main contributions of this thesis are as follows:

- In this thesis, a MIMO frequency domain model of a single VSC is developed that includes the complete control and physical systems. Based on the developed model of single VSC, a frequency domain model of parallel VSCs is developed considering the d-axis of the synchronous reference frame aligned with the grid voltage. Thus, all the VSCs have the same reference frame, and any number of parallel VSCs can easily be added to the MIMO frequency domain model, making the stability study simpler and more straightforward.
- A novel control method for weak grid connected VSC is proposed which uses the current errors to calculate compensation terms for the PLL angle and the voltage amplitude. This control method is added to the classic vector control of VSC. The method enables the VSC to operate and transfer the rated power during normal and transient conditions without the requirement of any control mode switch. The proposed control method is able to maintain system stability if the strength of the connected AC system changes during operation without the need for changing the controller gains. Compared to other methods in the literature, this approach is simple to implement and, as

the current control loop is always in place, the VSC can control the current during transients.

- A control method based on active damping of the voltage oscillations using virtual impedance is proposed in this thesis for improving system stability of weak grid connected VSCs. The virtual impedance based voltage stabiliser control works as an extra outer control loop for the vector current control for both d- and q-axis. This control method is also simple to implement and retains the current loop structure. Based on this principle, an external device is proposed that can be utilised and connected to a weak point of the grid to allow a large amount of VSC interfaced power generation (e.g. wind power) to be connected to the grid without inducing stability issues.

## 6.3. Suggestions for Future Research

Based on the studies conducted in this thesis, the potential areas for future research are proposed as follows:

- Optimisation of the design and allocation of the virtual impedance based external stabiliser to reduce the external VSC and the energy storage size can be considered as an area for further study. This can be achieved by optimising the controller gains, system structure, etc.
- In a large wind farm, the amount of the inter-array cables for connecting wind turbines is large. In this study, these cables are mostly not considered. Investigation on the impacts of these inter-array cables on the system modelling and proposed control methods is suggested as a further research field.
- Consideration of different outer control loop structures, and analysis of their impacts on the overall system performance is suggested for further investigation.
- Conduct experimental verification of the proposed control methods.

# References


[1] IEA, *Next-Generation Wind and Solar Power from Cost to Value* IEA, 2016.

[2] WindEurope, "Wind in Power-2016 European Statistics," Wind Europe Business Intelligence2017.

[3] WindEurope, "The European Offshore Wind Industry-Key Trends and Statistics 2016," WindEurope2017.

[4] T. Burton, D. Sharpe, N. Jenkins, and E. Bossanyi, *Wind Energy Handbook*: John Wiley & Sons, Ltd, 2011.

[5] J. F. Manwell, J. G. McGowan, and A. l. Rogers, *Wind Energy Explained Theory, Design and Application*: John Willey and Sons, Ltd, 2002.

[6] K. Givaki, M. Parker, and P. Jamieson, "Estimation of the Power Electronic Converter Lifetime in Fully Rated Converter Wind Turbine for Oshore and Offshore Wind Farms," in *7th IET International Conference on Power Electronics, Machines and Drives (PEMD 2014)*, Manchester, 2014.

[7] O. Anaya-Lara, D. Campos-Gaona, E. Moreno-Goytia, and G. Adam, *Offshore Wind Energy Generation Control, Protection, and Integraion to Electrical Systems*: John Wiley & Sons, Ltd, 2014.

[8] L. Holdsworth, X. G. Wu, J. B. Ekanayake, and N. Jenkins, "Comparison of Fixed Speed and Doubly-Fed Induction Wind Turbines During Power System Disturbances," *IEE Proceedings - Generation, Transmission and Distribution,* vol. 150, pp. 343-352, 2003.

[9] S. K. Chaudhary, R. Teodorescu, and P. Rodriguez, "Wind Farm Grid Integration Using VSC Based HVDC Transmission - An Overview," in *IEEE Energy 2030 Conference*, Atlanta, 2008.

[10] T. Ackermann, "Transmission Systems for Offshore Wind Farms," in *Wind Power in Power Systems*, ed West Sussex: John Willey and Sons, Ltd, 2005, pp. 479-503.

[11] Y. Iwatta, S. Tanaka, K. Sakamoto, H. Konishi, and H. Kawazoe, "Simulation Study of a Hybrid HVDC System Composed of a Self-Commutated Converter and a Line-Commutated Converter," in *Sixth International Conference on AC and DC Power Transmission*, 1996.

[12] N. Flourentzou, V. G. Agelidis, and G. D. Demetriades, "VSC-Based HVDC Power Transmission Systems: An Overview," *IEEE Trans. Power Electron.*, vol. 24, pp. 592-602, 2009.

[13] L. Xu and V. Agelidis, "VSC Transmission System Using Flying Capacitor Multilevel Converters and Hybrid PWM Control," *IEEE Trans. Power Del.*, vol. 22, pp. 693 - 702,, 2007.

[14] M. P. Bahrman, J. G. Johansson, and B. A. Nilsson, "Voltage Source Converter Transmission Technologies: the Right Fit for the Application," in *IEEE Power Engineering Society General Meeting*, 2003.

[15] B. R. Andersen, L. Xu, P. J. Horton, and P. Cartwright, "Topologies for VSC transmission," *Power Engineering Journal* vol. 16, pp. 142 - 150, 2002.

[16] D. Jovcic, L. A. Lamont, and L. Xu, "VSC Transmission Model for Analytical Studies," in *IEEE Power Engineering Society General Meeting*, 2003, pp. 1-1742 Vol. 3.

[17] G. Strbac, A. Shakoor, M. Black, D. Pudjianto, and T. Bopp, "Impact of Wind Generation on the Operation and Development of the UK Electricity Systems," *Electric Power Systems Research,* vol. 77, pp. 1214-1227, 2007/07/01/ 2007.

[18] I. A. Gowaid, A. El-Zawawi, and M. El-Gammal, "Improved Inertia and Frequency Support from Grid-Connected DFIG Wind Farms," in *IEEE/PES Power Systems Conference and Exposition (PSCE)*, Phoenix, 2011.

[19] L. Badesa, S. Fathima, M. T. Musavi, and P. Villeneuve, "Impact of Wind Generation on Dynamic Voltage Stability and Influence of the Point of Interconnection," in *2016 IEEE Green Technologies Conference (GreenTech)*, 2016, pp. 84-89.
[20] S. Heier, "The Transfer of Electrical Energy to the Supply Grid," in *Grid Integration of Wind Energy*, ed: John Wiley & Sons, Ltd, 2014, pp. 210-354.
[21] E. W. E. Association, "The European Offshore Wind Industry -Key Trends and Statistics 2015," 2016.
[22] G. Quinonez-Varela, G. W. Ault, O. Anaya-Lara, and J. R. McDonald, "Electrical Collector System Options for Large Offshore Wind Farms," in *IET Renewable Power Generation*, 2007.
[23] K. Givaki, D. Chen, and O. Anaya-Lara, "Stability studies of different AC collection network topologies in wind farms," presented at the International Conference on Renewable Power Generation, London, 2016.
[24] Y. Zhou, D. E. Macpherson, W. Blewitt, and D. Jovcic, "Comparison of DC-DC Converter Topologies for Offshore Wind-Farm Application," in *6th IET International Conference on Power Electronics, Machines and Drives (PEMD 2012)* 2012, pp. 1-6.
[25] S. Dutta and T. J. Overbye, "A Clustering Based Wind Farm Collector System Cable Layout Design," in *IEEE Power and Energy Conference at Illinois*, 2011, pp. 1-6.
[26] B. Xiaoyan, L. Guangyue, and K. C. Wong, "Impact of Wind Farm Cluster with DFIG on Power System Transient Stability," in *IEEE PES Innovative Smart Grid Technologies*, 2012, pp. 1-3.
[27] D. Elliott, C. E. Jones, and S. Finney, "A Comparison of Technologies for the Clustering of Multiple Wind Turbines," in *European Wind Energy Association Annual Conference*, Vienna, 2013.
[28] H. J. Bahirat, B. A. Mork, and H. K. Hoidalen, "Comparison of Wind Farm Topologies for Offshore Applications," in *IEEE Power and Energy Society General Meeting*, San Diego, 2012.
[29] K. Musasa, M. N. Gitau, and R. C. Bansal, "Comparative Analyses of DC Collection Grid Based Power Converter Topologies for Offshore Wind Farm," in *International Conference on Renewable Power Generation (RPG 2015)*, 2015, pp. 1-6.
[30] D. W. Elliott, S. J. Finney, and C. Booth, "Single Converter Interface for a Cluster of Offshore Wind Turbines," in *IET Conference on Renewable Power Generation* 2011, pp. 1-6.
[31] G. Quinonez-Varela, G. W. Ault, O. Anaya-Lara, and J. R. McDonald, "Electrical Collector System Options for Large Offshore Wind Farms," *IET Renewable Power Generation*, vol. 1, pp. 107-114, 2007.
[32] "IEEE Guide for Planning DC Links Terminating at AC Locations Having Low Short-Circuit Capacities," *IEEE Std 1204-1997*, pp. 1-216, 1997.
[33] CIGRE, "Connection of Wind Farms to Weak AC Networks," Paris, 2016.
[34] L. V. L. Abreu and M. Shahidehpour, "Wind Energy and Power System Inertia," in *IEEE Power Engineering Society General Meeting*, Montreal, 2006.
[35] X. Zhu, Y. Wang, L. Xu, X. Zhang, and H. Li, "Virtual Inertia Control of DFIG-based Wind Turbines for Dynamic Grid Frequency Support " in *IET Conference on Renewable Power Generation*, Edinburgh, 2011.
[36] P. Wall, F. González-Longatt, and V. Terzija, "Demonstration of an Inertia Constant Estimation Method through Simulation," in *45th International Universities Power Engineering Conference (UPEC)* Cardiff, 2010.
[37] W. Freitas, Z. Huang, and W. Xu, "A practical method for assessing the effectiveness of vector surge relays for distributed generation applications," *IEEE Trans. Power Del.*, vol. 20, pp. 57-63, 2005.
[38] E. Twining and D. G. Holmes, "Grid Current Regulation of a Three-phase Voltage Source Inverter with an LCL Input Filter," *IEEE Trans. Power Electron.*, vol. 18, pp. 888 - 895, 2003.

[39] B. Mokrytzki, "Pulse Width Modulated Inverters for AC Motor Drives," *IEEE Trans. Industry and General Appl.*, vol. IGA-3, pp. 493-503, 1967.
[40] Z. Yu, A. Mohammed, and I. Panahi, "A review of three PWM techniques," in *1997 American Control Conference* 1997, pp. 257-261 vol.1.
[41] H. W. v. d. Broeck, H. C. Skudelny, and G. V. Stanke, "Analysis and Realization of a Pulsewidth Modulator Based on Voltage Space Vectors," *IEEE Trans. Ind. Appl.*, vol. 24, pp. 142-150, 1988.
[42] M. Malinowski, M. Jasinski, and M. P. Kazmierkowski, "Simple direct power control of three-phase PWM rectifier using space-vector modulation (DPC-SVM)," *IEEE Trans. Ind. Electron.*, vol. 51, pp. 447-454, 2004.
[43] D. Zhi, L. Xu, and B. W. Williams, "Improved Direct Power Control of Grid-Connected DC/AC Converters," *IEEE Trans. Power Electron.*, vol. 24, pp. 1280-1292, 2009.
[44] L. Xu, D. Zhi, and L. Yao, "Direct Power Control of Grid Connected Voltage Source Converters," in *IEEE Power Engineering Society General Meeting*, Tampa, 2007.
[45] J. L. Duarte, A. V. Zwam, C. Wijnands, and A. Vandenput, "Reference frames fit for controlling PWM rectifiers," *IEEE Trans. Ind. Electron.*, vol. 46, pp. 628-630, 1999.
[46] Y. Cho and K. B. Lee, "Virtual-Flux-Based Predictive Direct Power Control of Three-Phase PWM Rectifiers With Fast Dynamic Response," *IEEE Trans. Power Electron.*, vol. 31, pp. 3348-3359, 2016.
[47] M. Malinowski, M. P. Kazmierkowski, S. Hansen, F. Blaabjerg, and G. D. Marques, "Virtual-Flux-Based Direct Power Control of Three-phase PWM Rectifiers," *IEEE Trans. Ind. Appl.*, vol. 37, pp. 1019-1027, 2001.
[48] T. Noguchi, H. Tomiki, S. Kondo, and I. Takahashi, "Direct Power Control of PWM Converter Without Power-Source Voltage Sensors," *IEEE Trans. Ind. Appl.*, vol. 34, pp. 473-479, 1998.
[49] T. Ohnishi, "Three phase PWM converter/inverter by means of instantaneous active and reactive power control," in *International Conference on Industrial Electronics, Control and Instrumentation*, 1991, pp. 819-824 vol.1.
[50] G. Escobar, A. M. Stankovic, J. M. Carrasco, E. Galvan, and R. Ortega, "Analysis and Design of Direct Power Control (DPC) for a Three Phase Synchronous Rectifier via Output Regulation Subspaces," *IEEE Trans. Power Electron.*, vol. 18, pp. 823-830, 2003.
[51] S. A. Larrinaga, M. A. R. Vidal, E. Oyarbide, and J. R. T. Apraiz, "Predictive Control Strategy for DC/AC Converters Based on Direct Power Control," *IEEE Trans. Ind. Electron.*, vol. 54, pp. 1261-1271, 2007.
[52] S. Vazquez, J. A. Sanchez, J. M. Carrasco, J. I. Leon, and E. Galvan, "A Model-Based Direct Power Control for Three-Phase Power Converters," *IEEE Trans. Ind. Electron.*, vol. 55, pp. 1647-1657, 2008.
[53] D. Zhi and L. Xu, "Direct Power Control of DFIG With Constant Switching Frequency and Improved Transient Performance," *IEEE Trans. Energy Convers.*, vol. 22, pp. 110-118, 2007.
[54] P. Antoniewicz, M. P. Kazmierkowski, P. Cortes, J. Rodriguez, and A. Sikorski, "Predictive Direct Power Control Algorithm for Three Phase AC/DC Converter," in *The International Conference on "Computer as a Tool"-EUROCON 2007* 2007, pp. 1530-1534.
[55] B. Singh and N. K. S. Naidu, "Direct Power Control of Single VSC-Based DFIG Without Rotor Position Sensor," *IEEE Trans. Ind. Appl.*, vol. 50, pp. 4152-4163, 2014.
[56] M. P. Kazmierkowski and L. Malesani, "Current Control Techniques for Three-Phase Voltage-Source PWM Converters: a Survey," *IEEE Trans. Ind. Electron.*, vol. 45, pp. 691-703, 1998.

[57] F. Blaabjerg, R. Teodorescu, and M. Liserre, "Overview of Control and Grid Synchronization for Distributed Power Generation Systems " *IEEE Trans. Ind. Electron.* , vol. 53, pp. 1398-1409, 2006.

[58] H. Cha, T.-K. Vu, and J.-E. Kim, "Design and Control of Proportional-Resonant Controller Based Photovoltaic Power Conditioning System " in *IEEE Energy Conversion Congress and Exposition* San Jose, 2009.

[59] R. Teodorescu, F. Blaabjerg, M. Liserre, and P. C. Loh, "Proportional-resonant controllers and filters for grid-connected voltage-source converters," *IEE Proceedings - Electric Power Applications*, vol. 153, pp. 750-762, 2006.

[60] J. Svensson, "Synchronisation methods for grid-connected voltage source converter," *IEE Proceedings Generation, Transmission and Distribution, ,* vol. 148, pp. 229 - 235, 2001.

[61] M. Karimi-Ghartemani, M. Mojiri, A. Safaee, J, x00C, Walseth, *et al.*, "A New Phase-Locked Loop System for Three-Phase Applications," *IEEE Trans. Power Electron.*, vol. 28, pp. 1208-1218, 2013.

[62] F. D. Freijedo, A. G. Yepes, x00D, x00F, pez, A. Vidal, *et al.*, "Three-Phase PLLs With Fast Postfault Retracking and Steady-State Rejection of Voltage Unbalance and Harmonics by Means of Lead Compensation," *IEEE Trans. Power Electron.*, vol. 26, pp. 85-97, 2011.

[63] D. Jovcic, "Phase locked loop system for FACTS," *IEEE Trans. Power Syst.*, vol. 18, pp. 1116-1124, 2003.

[64] V. Minambres, M. I. Milanes, B. Vinagre, and E. Romero, "Comparison of Controllers for a Three-Phase Phase Locked Loop System Under Distorted Conditions," in *2009 Compatibility and Power Electronics*, 2009, pp. 79-85.

[65] V. Kaura and V. Blasko, "Operation of a phase locked loop system under distorted utility conditions," *IEEE Trans. Ind. Appl.*, vol. 33, pp. 58 - 63, 1997.

[66] B. Meersman, J. De Kooning, T. Vandoorn, L. Degroote, B. Renders, and L. Vandevelde, "Overview of PLL methods for Distributed Generation Units," in *45th International Universities Power Engineering Conference (UPEC)*, Cardiff, 2010.

[67] H.-S. Song and K. Nam, "Instantaneous Phase-angle Estimation Algorithm under Unbalanced Voltage-sag Conditions," *IEE Proceedings Generation, Transmission and Distribution*, vol. 147, pp. 409 - 415, 2000.

[68] X. Yuan, W. Merk, H. Stemmler, and J. Allmeling, "Stationary-frame generalized integrators for current control of active power filters with zero steady-state error for current harmonics of concern under unbalanced and distorted operating conditions," *IEEE Trans. Ind. Appl.*, vol. 38, pp. 523 - 532, 2002.

[69] M. Karimi-Ghartemani and M. R. Iravani, "A Nonlinear Adaptive Filter for Online Signal Analysis in Power Systems: Applications," *IEEE Trans. Power Del.*, vol. 17, pp. 617 - 622, 2002.

[70] M. Karimi-Ghartemani and M. R. Iravani, "A Method for Synchronization of Power Electronic Converters in Polluted and Variable-frequency Environments," *IEEE Trans. Power Syst.*, vol. 19, pp. 1263 - 1270, 2004.

[71] P. Rodriguez, R. Teodorescu, I. Candela, A. V. Timbus, M. Liserre, and F. Blaabjerg, "New Positive-sequence Voltage Detector for Grid Synchronization of Power Converters under Faulty Grid Conditions," in *37th IEEE Power Electronics Specialists Conference*, 2006.

[72] M. Karimi-Ghartemani, "A Novel Three-phase Magnitude-Phase-Locked Loop System," *IEEE Trans. Circuits Syst. I, Reg. Papers*, vol. 53, pp. 1792 - 1802, 2006.

[73] S. Pavljasevic and F. Dawson, "Synchronization to Disturbed Utility-Network Signals Using a Multirate Phase-Locked Loop," *IEEE Trans. Ind. Electron.*, vol. 53, pp. 1410 - 1417, 2006.

[74] A. Egea-Alvarez, S. Fekriasl, F. Hassan, and O. Gomis-Bellmunt, "Advanced Vector Control for Voltage Source Converters Connected to Weak Grids," *IEEE Trans. Power Syst.*, vol. 30, pp. 3072-3081, 2015.

[75] L. Zhang, L. Harnefors, and H. P. Nee, "Power-Synchronization Control of Grid-Connected Voltage-Source Converters," *IEEE Trans. Power Syst.*, vol. 25, pp. 809-820, 2010.

[76] L. Harnefors, M. Bongiorno, and S. Lundberg, "Input-Admittance Calculation and Shaping for Controlled Voltage-Source Converters," *IEEE Trans. Ind. Electron.*, vol. 54, pp. 3323-3334, 2007.

[77] D. Dong, B. Wen, D. Boroyevich, P. Mattavelli, and Y. Xue, "Analysis of Phase-Locked Loop Low-Frequency Stability in Three-Phase Grid-Connected Power Converters Considering Impedance Interactions," *IEEE Trans. Ind. Electron.*, vol. 62, pp. 310-321, 2015.

[78] J. Z. Zhou, D. Hui, F. Shengtao, Z. Yi, and A. M. Gole, "Impact of Short-Circuit Ratio and Phase-Locked-Loop Parameters on the Small-Signal Behavior of a VSC-HVDC Converter," *IEEE Trans. Power Del.*, vol. 29, pp. 2287-2296, 2014.

[79] B. H. Kim and S. K. Sul, "Stability Oriented Design of Frequency Drift Anti-islanding and Phase-Locked Loop Under Weak Grid," *IEEE Journal of Emerging and Selected Topics in Power Electronics*, vol. PP, pp. 1-1, 2016.

[80] B. Wen, D. Boroyevich, R. Burgos, P. Mattavelli, and Z. Shen, "Analysis of D-Q Small-Signal Impedance of Grid-Tied Inverters," *IEEE Trans. Power Electron.*, vol. 31, pp. 675-687, 2016.

[81] W. Du, X. Chen, and H. F. Wang, "PLL-induced Modal Resonance of Grid-Connected PMSGs with the Power System Electromechanical Oscillation Modes," *IEEE Trans. Sustain. Energy*, vol. PP, pp. 1-1, 2017.

[82] S. Grunau and F. W. Fuchs, "Effect of Wind-Energy Power Injection into Weak Grids," in *EWEA Annual Event*, Copenhagen, 2012.

[83] J. A. Suul, S. D. Arco, P. Rodr, xed, guez, and M. Molinas, "Impedance-Compensated Grid Synchronisation for Extending the Stability Range of Weak Grids with Voltage Source Converters," *IET Generation, Transmission & Distribution*, vol. 10, pp. 1315-1326, 2016.

[84] A. Egea-Alvarez, C. Barker, F. Hassan, and O. Gomis-Bellmunt, "Capability Curves of a VSC-HVDC Connected to a Weak AC Grid Considering Stability and Power Limits," in *11th IET International Conference on AC and DC Power Transmission*, 2015, pp. 1-5.

[85] J. P. Barton and D. G. Infield, "Energy Storage and Its Use with Intermittent Renewable Energy," *IEEE Trans. Energy Convers.*, vol. 19, pp. 441-448, 2004.

[86] J. Z. Zhou and A. M. Gole, "VSC Transmission Limitations Imposed by AC System Strength and AC Impedance Characteristics," in *10th IET International Conference on AC and DC Power Transmission* 2012, pp. 1-6.

[87] M. F. M. Arani and Y. A. R. I. Mohamed, "Analysis and Performance Enhancement of Vector-Controlled VSC in HVDC Links Connected to Very Weak Grids," *IEEE Trans. Power Syst.*, vol. 32, pp. 684-693, 2017.

[88] J. Driesen and K. Visscher, "Virtual Synchronous Generators," in *IEEE Power and Energy Society General Meeting - Conversion and Delivery of Electrical Energy in the 21st Century*, 2008, pp. 1-3.

[89] H. P. Beck and R. Hesse, "Virtual Synchronous Machine," in *9th International Conference on Electrical Power Quality and Utilisation (EPQU 2007)* 2007, pp. 1-6.

[90] M. Ashabani and Y. A.-R. I. Mohamed, "Integrating VSCs to Weak Grids by Nonlinear Power Damping Controller With Self-Synchronization Capability," *IEEE Trans. Power Syst.*, vol. 29, pp. 805-814, 2014.

[91] Q. C. Zhong and Weiss, "Synchronverters: Inverters that mimic synchronous generators," *IEEE Trans. Ind. Electron.*, vol. 58, pp. 1259-1267, 2011.

[92] L. Zhang, L. Harnefors, and H. P. Nee, "Interconnection of Two Very Weak AC Systems by VSC-HVDC Links Using Power-Synchronization Control," *IEEE Trans. Power Syst.*, vol. 26, pp. 344-355, 2011.

[93] Q. C. Zhong, P. L. Nguyen, Z. Ma, and W. Sheng, "Self-Synchronized Synchronverters: Inverters Without a Dedicated Synchronization Unit," *IEEE Trans. Power Electron.*, vol. 29, pp. 617-630, 2014.

[94] K. Visscher and S. W. H. D. Haan, "Virtual synchronous machines (VSGs) for frequency stabilisation in future grids with a significant share of decentralized generation," in *CIRED Seminar SmartGrids for Distribution*, 2008, pp. 1-4.

[95] C. H. Zhang, Q. C. Zhong, J. S. Meng, X. Chen, Q. Huang, S. h. Chen, *et al.*, "An Improved Synchronverter Model and Its Dynamic Behaviour Comparison with Synchronous Generator," in *2nd IET Renewable Power Generation Conference (RPG 2013)*, 2013, pp. 1-4.

[96] S. D'Arco, J. A. Suul, and O. B. Fosso, "A Virtual Synchronous Machine Implementation for Distributed Control of Power Converters in Smart Grids," *Electric Power Systems Research*, vol. 122, pp. 180-197, 5// 2015.

[97] O. Mo, S. D. Arco, and J. A. Suul, "Evaluation of Virtual Synchronous Machines with Dynamic or Quasi-stationary Machine Models," *IEEE Trans. Ind. Electron.*, vol. PP, pp. 1-1, 2016.

[98] Y. Chen, R. Hesse, D. Turschner, and H. P. Beck, "Dynamic Properties of the Virtual Synchronous Machine (VSIMA)," in *International Conference on Renewable Energies and Power Quality*, Las Palmas, Spain, 2011.

[99] M. Albu, M. Calin, D. Federenciuc, and J. Diaz, "The Measurement Layer of the Virtual Synchronous Generator Operation in the Field Test," in *IEEE International Workshop on Applied Measurements for Power Systems (AMPS)*, 2011, pp. 85-89.

[100] Y. Chen, R. Hesse, D. Turschner, and H. P. Beck, "Comparison of Methods for Implementing Virtual Synchronous Machine on Inverters " in *International Conference on Renewable Energies and Power Quality (ICREPQ'12)* Santiago de Compostela 2012.

[101] Y. Hirase, K. Abe, K. Sugimoto, and Y. Shindo, "A Grid-Connected Inverter with Virtual Synchronous Generator Model of Algebraic Type," *Electrical Engineering in Japan*, vol. 184, pp. 10-21, 2013.

[102] H. Bevrani, T. Ise, and Y. Miura, "Virtual Synchronous Generators: A Survey and New Perspectives," *International Journal of Electrical Power & Energy Systems*, vol. 54, pp. 244-254, 1// 2014.

[103] T. V. Van, K. Visscher, J. Diaz, V. Karapanos, A. Woyte, M. Albu, *et al.*, "Virtual Synchronous Generator: An Element of Future Grids," in *IEEE PES Innovative Smart Grid Technologies Conference Europe (ISGT Europe)*, 2010, pp. 1-7.

[104] M. P. N. v. Wesenbeeck, S. W. H. d. Haan, P. Varela, and K. Visscher, "Grid Tied Converter with Virtual Kinetic Storage," in *IEEE Bucharest PowerTech*, 2009, pp. 1-7.

[105] V. Karapanos, S. d. Haan, and K. Zwetsloot, "Real time simulation of a power system with VSG hardware in the loop," in *IECON 2011*, 2011, pp. 3748-3754.

[106] T. Shintai, Y. Miura, and T. Ise, "Reactive power control for load sharing with virtual synchronous generator control," in *7th International Power Electronics and Motion Control Conference*, 2012, pp. 846-853.

[107] K. Sakimoto, Y. Miura, and T. Ise, "Stabilization of a power system with a distributed generator by a Virtual Synchronous Generator function," in *8th International Conference on Power Electronics - ECCE Asia*, 2011, pp. 1498-1505.

[108] K. i. Sakimoto, K. Sugimoto, and Y. Shindo, "Low Voltage Ride Through Capability of a Grid Connected Inverter Based on the Virtual Synchronous Generator," in *IEEE 10th International Conference on Power Electronics and Drive Systems (PEDS)*, 2013, pp. 1066-1071.

[109] Y. Chen, R. Hesse, D. Turschner, and H. P. Beck, "Investigation of the Virtual Synchronous Machine in the Island Mode," in *3rd IEEE PES Innovative Smart Grid Technologies Europe (ISGT Europe)*, 2012, pp. 1-6.

[110] Y. Chen, R. Hesse, D. Turschner, and H. P. Beck, "Improving the Grid Power Quality Using Virtual Synchronous Machines," in *International Conference on Power Engineering, Energy and Electrical Drives*, 2011, pp. 1-6.

[111] S. D. Arco, J. A. Suul, and O. B. Fosso, "Control System Tuning and Stability Analysis of Virtual Synchronous Machines," in *IEEE Energy Conversion Congress and Exposition*, 2013, pp. 2664-2671.

[112] N. P. W. Strachan and D. Jovcic, "Stability of a Variable-Speed Permanent Magnet Wind Generator With Weak AC Grids," *IEEE Trans. Power Del.*, vol. 25, pp. 2779-2788, 2010.

[113] H. Azani, A. Massoud, L. Benbrahim, B. W. Williams, and D. Holiday, "An LCL Filter-based Grid-interfaced Three-phase Voltage Source Inverter: Performance Evaluation and Stability Anaylsis," in *7th IET International Conference on Power Electronics, Machines and Drives (PEMD 2014)*, 2014, pp. 1-6.

[114] F. Tang, X. Jin, X. Zhou, and Y. Tong, "Stability analysis on parallel of LCL-filter-based grid-connected converters in MW-level direct-drive wind generation using complex vector," in *International Conference onElectrical Machines and Systems* 2011, pp. 1-6.

[115] D. Jovcic, N. Pahalawaththa, and M. Zavahir, "Analytical Modelling of HVDC-HVAC Systems," *IEEE Trans. Power Del.*, vol. 14, pp. 506-511, 1999.

[116] C. Osauskas and A. Wood, "Small-signal dynamic modeling of HVDC systems," *IEEE Trans. Power Del.*, vol. 18, pp. 220-225, 2003.

[117] M. Durrant, H. Werner, and K. Abbott, "Model of a VSC HVDC Terminal Attached to a Weak AC System," in *Proceedings of 2003 IEEE Conference on Control Applications*, 2003, pp. 178-182 vol.1.

[118] C. Debruyne, S. Derammelaere, J. Desmet, and L. Vandevelde, "Using General Synchronous Machine Theory to Integrate PLL Controller Dynamics into a Static Power Electronic Converter Model," in *IEEE Industry Applications Society Annual Meeting (IAS)*, Las Vegas, 2012.

[119] L. Xu, L. Yao, and C. Sasse, "Grid Integration of Large DFIG-Based Wind Farms Using VSC Transmission," *IEEE Trans. Power Syst.*, vol. 22, pp. 976-984, 2007.

[120] D. Chen and L. Xu, "Autonomous DC Voltage Control of a DC Microgrid With Multiple Slack Terminals," *IEEE Trans. Power Syst.*, vol. 27, pp. 1897-1905, 2012.

[121] A. Yazdani and R. Iravani, *Voltage-Sourced Converters in Power Systems Modeling, Control and Applications*. Hoboken: John Wiley & Sons, 2010.

[122] L. Xu and L. Fan, "System identification based VSC-HVDC DC voltage controller design," in *North American Power Symposium (NAPS)*, Champaign, 2012.

[123] G. P. Adam, K. H. Ahmed, S. J. Finney, K. Bell, and B. W. Williams, "New Breed of Network Fault-Tolerant Voltage-Source-Converter HVDC Transmission System," *IEEE Trans. Power Syst.*, vol. 28, pp. 335 - 346, 2013.

[124] K. Givaki and L. Xu, "Stability analysis of large wind farms connected to weak AC networks incorporating PLL dynamics," in *International Conference on Renewable Power Generation* 2015, pp. 1-6.

[125] D. Jovcic, "Control of High Voltage DC and Flexible AC Transmission Systems, PhD Thesis," The University of Auckland, Auckland1999.

[126] S. L. Lorenzen, A. B. Nielsen, and L. Bede, "Control of a Grid Connected Converter During Weak Grid Conditions," in *IEEE 7th International Symposium on Power Electronics for Distributed Generation Systems (PEDG)*, 2016, pp. 1-6.

[127] P. Channegowda and V. John, "Filter Optimization for Grid Interactive Voltage Source Inverters," *IEEE Trans. Ind. Electron.*, vol. 57, pp. 4106-4114, 2010.

# Appendices

## Appendix 1. Simulation Models

In this section the main simulation models developed in Matlab / Simulink are presented.

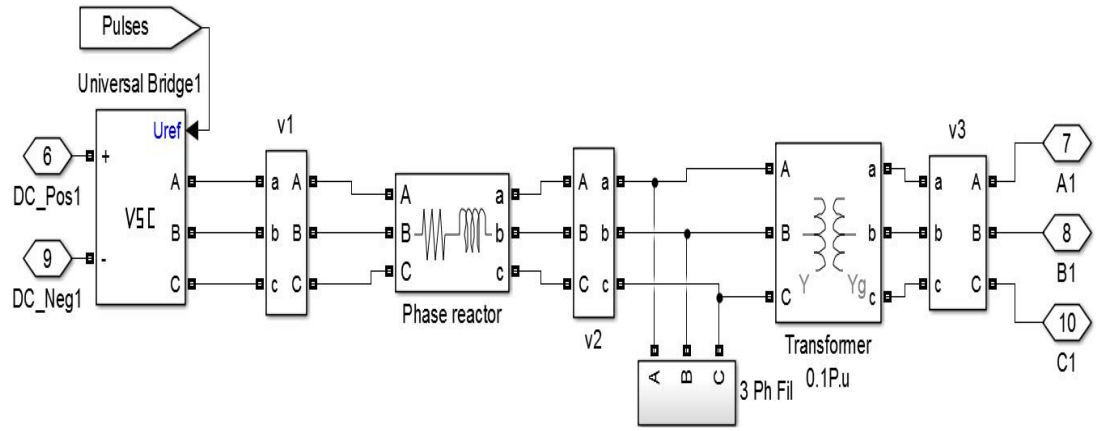


Fig. A1. 1. Converter schematic model in Simulink

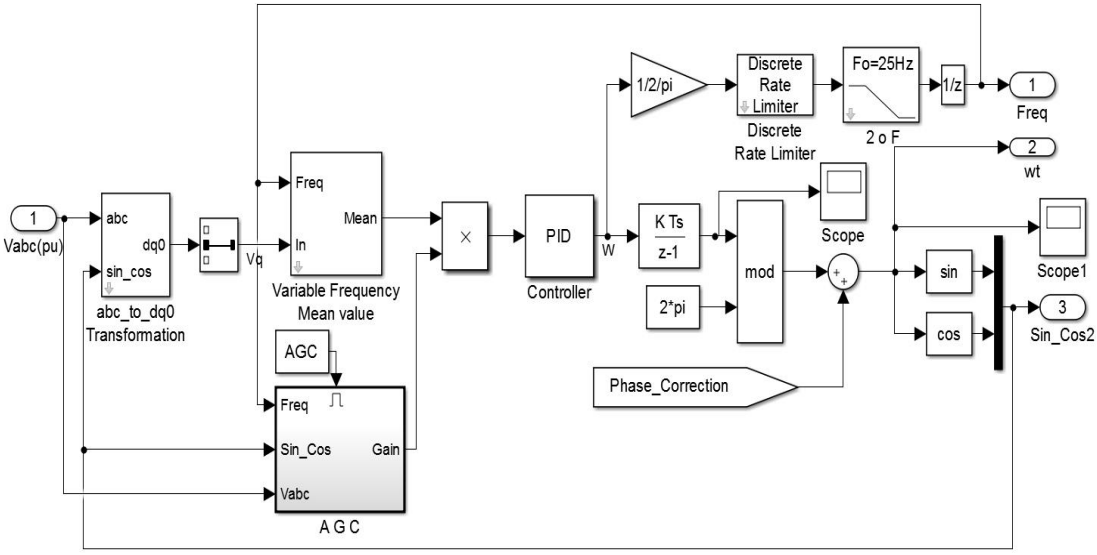


Fig. A1. 2. The Simulink implementation of the proposed d-axis current error controller added to the PLL output angle

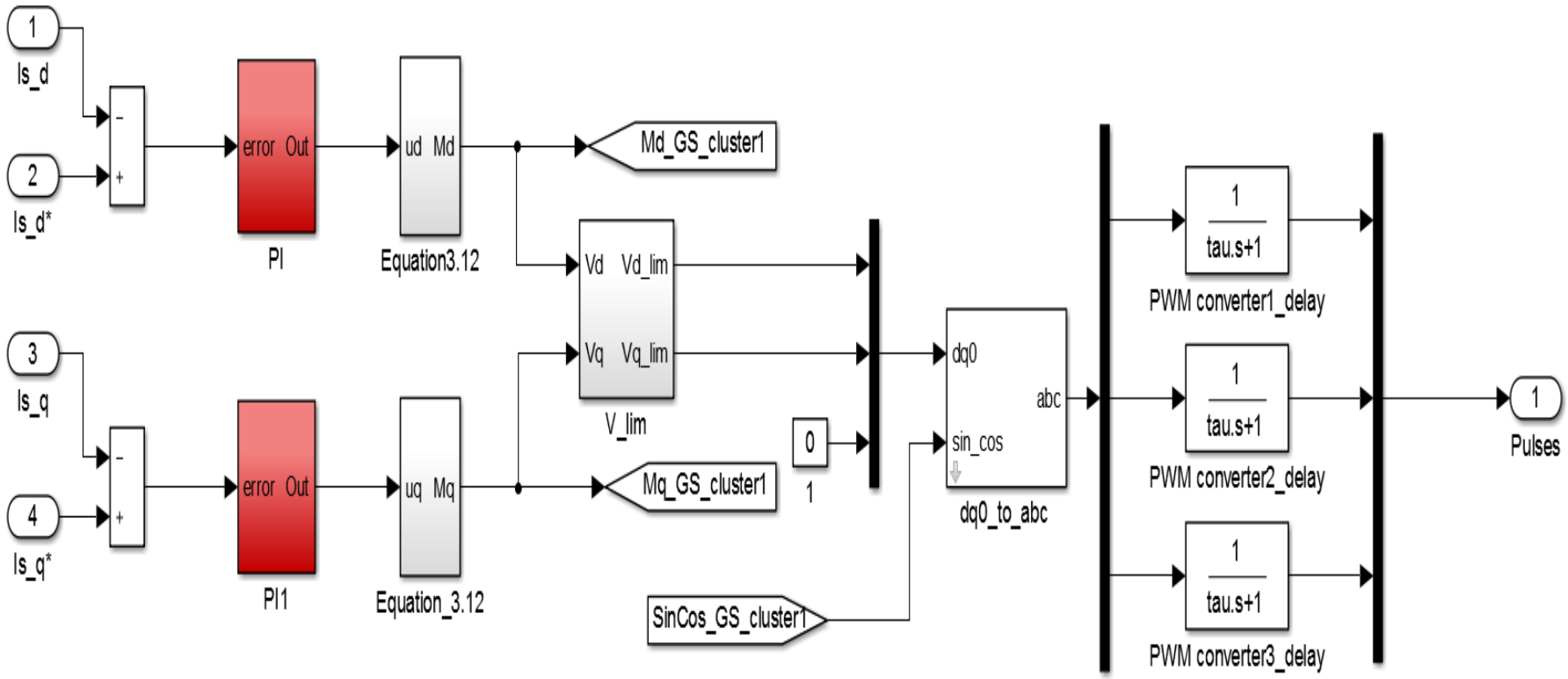


Fig. A1. 3. The vector current control model implementation in Simulink

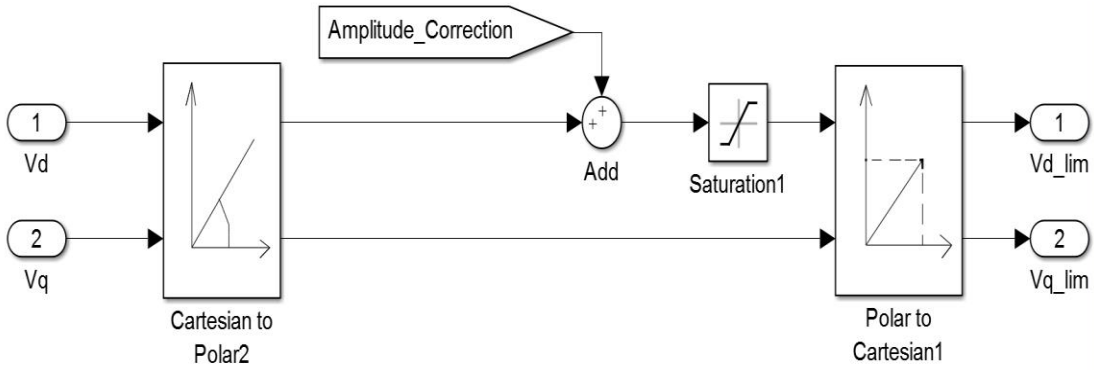


Fig. A1. 4. The Simulink implementation of the proposed q-axis current error into the system

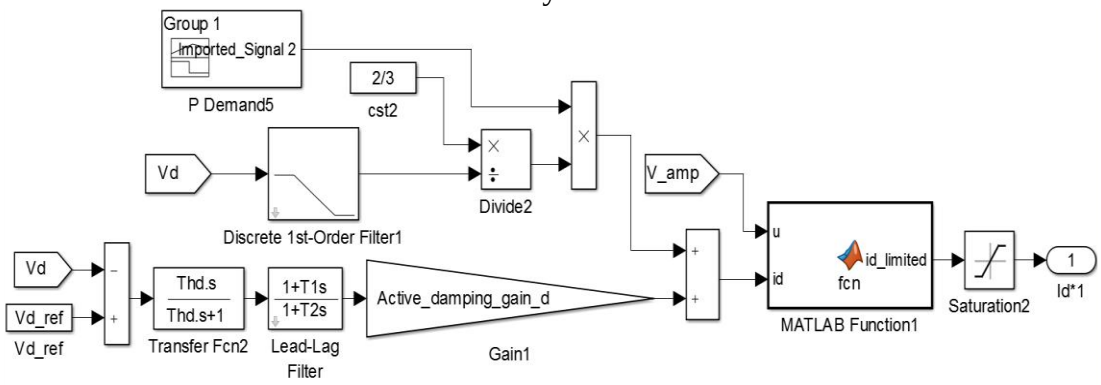


Fig. A1. 5. The Simulink implementation of the proposed d-axis virtual impedance controller

# Appendix 2. List of Publications

The list of publications based on this thesis are as follows:

- K. Givaki, L. Xu, "*Stability analysis of large wind farms connected to weak AC networks incorporating PLL dynamics,"* IET Renewable Power Generation (RPG 2015).

  **Abstract:**

  Voltage source converter interfaced wind turbines connected to weak grids can induce system instability. A state-space model is used in this paper to study the stability of large wind farms. Dynamics of the phase locked loop is integrated to the state-space model. The advantage of this model is that it allows study the stability of systems with parallel wind turbines. Studies on the dynamic responses of the system show the importance of including phase locked loop as its existence can induce system instability especially under weak network conditions. This model can be used to study the stability of converter interfaced wind farms and helps to design the converter controller to ensure wind farm system stability when connected to weak grids.

- K. Givaki, D. Chen, L. Xu, *"Current Error Based Compensations for VSC Current Control in Weak Grid for Wind Farm Applications",* IEEE Trans. Sustainable Energy (second round revision).

  **Abstract:**

  A novel current control strategy is proposed for voltage source converters connected to weak grid using conventional current vector control with additional current error based voltage angle and magnitude compensations. For connecting to very weak AC network, conventional vector control is proved to be unstable, whereas the proposed current error based compensations can significantly improve system stability. In this way, the proposed control can still benefit from the presence of current closed-loop control without the need for control switching during large AC voltage variations. Comprehensive frequency domain model is established to analyse stability performance. Comprehensive time

domain simulations are further carried out to validate its effectiveness and robustness by demonstrating its current control performance during a three phase fault, multiple-converter situation and various grid strength conditions.

- D. Chen, K. Givaki, L. Xu, *"Active Damping Control of Wind Farm Connected to Very Weak Electrical Grids",* IEEE Trans. Power Delivery (Preparation in Progress).

  **Abstract:**

  A stabilising control technique is proposed for Voltage Source Converter (VSC) generation from very weak grid in this paper. The proposed method is based on virtual impedance method and can be used along with reactive power compensations to enhance the overall voltage stability with no need for control mode switching during transients. The proposed method can further benefit from its flexibility of implementation for practical concerns. It can be either embedded in VSC generations or implemented by low-cost external aggregated stabilizers. A complete frequency domain model is established to prove the effectiveness of the stabilizing control with root locus. The effectiveness of proposed method is further validated by comprehensive time domain simulations concerning power (current) ramp, transient and external stabilizer tests.

- K. Givaki, D. Chen, L. Xu, H. Xu, *"A Current-error Based Control for VSC Integration to Weak Grid",* PES General Meeting, (Submitted).

  **Abstract:**

  A An enhanced current control strategy is proposed for voltage source converters for the integration to weak grids. The control derives from the current-error based vector control. By implementing simple close-loop compensations of both angle and magnitude inputs to the pulse width modulation, the damping of vector control in the weak grid can be significantly improved hence able to deliver full rated power to very weak grid. Due to the presence of the current loop, the fault-ride-through capability can be maintained with no need for mode switching. A comprehensive frequency domain model is employed to analyse the stability. Time domain simulations are further carried out to validate its effectiveness and robustness of integrating to the weak grid with fault-ride-through capability.

Papers published during my PhD that are not covered in this thesis:

- K. Givaki, M. Parker, P. Jamieson, *"Estimation of the power electronic converter lifetime in fully rated converter wind turbine for onshore and offshore wind farms",* Power Electronics, Machines and Drives (PEMD 2014)

**Abstract:**

A comparison has been made of the converter lifetime for a 3MW fully rated converter horizontal axis wind turbine located onshore and offshore. Simulated torque and speed of the turbine shaft were used to calculate voltage and current time series, that was used to calculate the junction temperatures of the diode and IGBT in the generator-side converter by a thermal-electrical model. A rain-flow counting algorithm was applied to the junction temperature in combination with an empirical model of the lifetime estimation, to calculate the lifetime of the power electronic modules in the turbine. The number of parallel modules for each location to achieve 20 years life time has also been found. Simulations show the lifetime consumption rate of the diode and IGBT is decreased exponentially by increasing number of parallel modules, lowering the average temperature. The offshore wind turbine has a higher lifetime consumption rate, requiring a slightly higher converter rating to achieve a 20-year lifetime, but this difference is small, and both turbines will use the same number of modules.

- K. Givaki, D. Chen, O. Anaya-Lara, *"Stability studies of different AC collection network topologies in wind farms",* IET Renewable Power Generation (RPG 2016).

**Abstract:**

In this paper, the stability studies for different wind farm collection network topologies have been performed. As the wind farm becomes larger, the inter-array network becomes larger.so that the impedance of the overall system will be increased. This means that the inter-array configuration can impact the stability of system. The dynamic studies results presented in this paper show that the star collection network topology has the ability to be connected to weaker grid followed by radial, double sided and single side ring collection network topology.